REPORT DOCUMENTATION PAGE

AFRL-SR-AR-TR-04-

$\mathcal{O}24\mathcal{S}$

1. AGENCY USE ONLY (Leave blank)	2. REPORT DATE	3. REPOI

01 Jun 2001 - 31 Jan 2004   FINAL

4. TITLE AND SUBTITLE
(THEME 2) SCALED-UP NONEQUILIBRIUM AIR PLASMAS

5. FUNDING NUMBERS
61102F
2308/TA

6. AUTHOR(S)
DR KRUGER

7. PERFORMING ORGANIZATION NAME(S) AND ADDRESS(ES)
STANFORD JUNIOR UNIVERSITY
496 LOMITA MALL
DURAND BLDG 137
STANFORD CA 94305-4030

8. PERFORMING ORGANIZATION REPORT NUMBER

9. SPONSORING/MONITORING AGENCY NAME(S) AND ADDRESS(ES)
AFOSR/NE
4015 WILSON BLVD
SUITE 713
ARLINGTON VA 22203

10. SPONSORING/MONITORING AGENCY REPORT NUMBER

FA9550-01-1-0389

11. SUPPLEMENTARY NOTES

12a. DISTRIBUTION AVAILABILITY STATEMENT
DISTRIBUTION STATEMENT A: Unlimited

12b. DISTRIBUTION CODE

13. ABSTRACT (Maximum 200 words)

Experimental investigations of flow/plasma interactions in a DC discharge placed in a transverse preheated air flow confirm the role of the gas heating effect. The volume of plasma produced by the discharge is found to decrease when the air flow increases. This counterintuitive result is analyzed through measurements of the reduced field strength E/N profile in the discharge. When the flow velocity increases, the gas traversing the discharge region has less time to undergo vibrational-translational energy transfer and therefore it does not heat up as much. Lower temperature results in higher gas density N, thereby decreasing the E/N further downstream the flow. Since the rate coefficients of electron-impact processes are controlled by the E/N, the discharge volume tends to be larger in the slower flows.

20040423 015

14. SUBJECT TERMS
flow/plasma and E/N profile

15. NUMBER OF PAGES

16. PRICE CODE

17. SECURITY CLASSIFICATION OF REPORT	18. SECURITY CLASSIFICATION OF THIS PAGE	19. SECURITY CLASSIFICATION OF ABSTRACT	20. LIMITATION OF ABSTRACT
Unclassified	Unclassified	Unclassified	UL

SCALED-UP NONEQUILIBRIUM AIR PLASMAS

Submitted by
Professor Charles H. Kruger (Principal Investigator)
Professor Christophe O. Laux (Associate Investigator)
Dr. Zdenko Machala
Professor Graham V. Candler

January 2004

Mechanical Engineering Department
Stanford University
Stanford, California 94305

THERMOSCIENCES DIVISION

SCALED-UP NONEQUILIBRIUM AIR PLASMAS

Final Technical Report for the Period:
June 1, 2001 – January 31, 2004

Submitted to

Dr. Robert J. Barker

Air Force Office of Scientific Research

Grant No. F49620-01-1-0389

Submitted by

Professor Charles H. Kruger (Principal Investigator)

Professor Christophe O. Laux (Associate Investigator)

Dr. Zdenko Machala

Professor Graham V. Candler

January 2004

Contents

1. Abstract

The objective of the current program was to investigate the volume scalability of nonequilibrium plasmas produced by electrical discharges in atmospheric pressure air. Both DC and repetitively pulsed plasma discharges have been successfully demonstrated in a MURI program on Air Plasma Ramparts, but the dimensions of these plasmas are typically limited to a few centimeters in length and a few millimeters in diameter.

In this report, we first review the experiments with single DC and pulsed discharges in ambient and preheated air and nitrogen and discuss the mechanism of gas heating that influences the discharge temperature and the power budget. We then examine the physical mechanisms that limit the size of individual discharges. To this end, we use cavity ring-down (CRDS) and optical emission spectroscopy (OES) to measure the concentration profiles of the dominant ion, N_2^+, and of various excited electronic states of N_2 and N_2^+, in order to define and determine the diameter of a nitrogen discharge. The electron concentration profiles were obtained from the CRDS-measured N_2^+ X (v=0) profiles by using our collisional-radiative model. A comparison of the spatial electron density profiles with the emission profiles yields reasonable agreement. This result supports the use of optical emission spectroscopy to measure the size of the atmospheric pressure nitrogen (and air) plasmas. We then present results of numerical models simulating two-dimensional DC discharges in air and nitrogen. Good agreement is obtained with our experimental observations.

Experimental investigations of flow/plasma interactions in a DC discharge placed in a transverse preheated air flow confirm the role of the gas heating effect. The volume of plasma produced by the discharge is found to decrease when the air flow increases. This counterintuitive result is analyzed through measurements of the reduced field strength E/N profile in the discharge. When the flow velocity increases, the gas traversing the discharge region has less time to undergo vibrational-translational energy transfer and therefore it does not heat up as much. Lower temperature results in higher gas density N, thereby decreasing the E/N further downstream the flow. Since the rate coefficients of electron-impact processes are controlled by the E/N, the discharge volume tends to be larger in the slower flows.

We then further investigate methods to increase the plasma volume by means of dual and multiple DC or pulsed discharges operated in parallel. Dual DC discharges in ambient air and nitrogen and multi-pin pulsed discharges are demonstrated with plasma volumes of cubic-centimeter size. We also examined dual parallel and transverse discharges in preheated air flows. These setups enable us to scale-up plasma volumes and to verify the effect of the gas flow velocity on the gas heating in the discharge.

Finally, we introduce a novel approach to produce highly ionized atmospheric pressure air and nitrogen plasmas in DC glow discharges. We employ thermionic cathodes ($LaCrO_3$, LaB_6 and Mo) and place the discharges in tubes with swirl gas flow injection. As a result, an increase

higher current densities and lower electric fields. The swirl flow confines the discharge, increasing its current and electron densities, and enhancing its stability. The discharge can be extended to as long as 10 cm between the electrodes. In addition, the electric field is lower with the thermionic cathodes than with the metal cathodes, resulting in a low power budget. A new falling region in our air discharge E-j and E/N-j characteristics was revealed, similar to nitrogen discharge characteristics. Computational analysis of the discharges in the swirl flow helps to understand the stabilizing effect of the swirl flow. DC discharges with thermionic cathodes combined with the swirl flow represent a promising way for producing scaled-up highly ionized plasmas in atmospheric air or nitrogen.

2. Technical Discussion

2.1. Introduction

This final technical report describes the results of our research program on "Scaled-up Nonequilibrium Air Plasmas." This program was supported by a grant from the Air Force Office of Scientific Research (Grant No. F49620-01-1-0389) and was conducted in the group of Prof. Kruger at Stanford University and Prof. Candler at the University of Minnesota.

Large-volume air plasmas at atmospheric pressure present considerable interest for a wide range of Air Force applications in plasma aerodynamics and flow control. Desirable conditions are electron densities of the order of 10^{13} cm^{-3} and gas temperatures less than 2000 K. Considerable advances have been achieved in a recent MURI program on Air Plasma Ramparts [1]. In particular, we have demonstrated that it is possible to produce over 10^{12} electrons/cm^3 in atmospheric pressure air with DC and repetitively pulsed discharges. Furthermore, we have experimentally demonstrated that it takes only 12 W/cm^3 of power to produce 10^{12} electrons/cm^3 with a repetitively pulsed discharge in air. This power level is about 250 times lower than for a DC discharge producing the same electron density.

The present program seeks to expand on the results of the MURI program. Specifically, we are interested in scaling up the MURI discharges to produce larger volumes of plasma. Our research effort has concentrated in the following directions:

- Understand the physical mechanisms that limit the size of an individual discharge

- Demonstrate the operation of several discharges to create larger plasma volumes

- Investigate flow/discharge interactions (parallel or transverse discharge)

- Test the use of thermionic cathodes and swirl gas flow injection to enhance the electron density and scale up plasma volumes

Section 2.2 provides an overview of our previous experiments with single DC discharges in atmospheric pressure air and nitrogen. Sections 2.3 to 2.5 present experimental and numerical investigations of the diameter of an individual DC discharge. Section 2.6 describes experimental investigation of flow/discharge interactions in a DC discharge placed perpendicular to a preheated air flow. Sections 2.7 to 2.9 reports the attempts to scale up plasma volumes by using dual and multiple DC and pulsed discharges, both in ambient and preheated flows, and in parallel, as well as transverse configurations. Finally, section 2.10 is focused on our most recent results of experiments with DC discharges with thermionic cathodes in the swirl flow and section 2.11 describes the computational analysis of DC discharges in tubes with the swirl flow.

2.2. Review of Experiments with Single DC and Pulsed Discharges

Single DC and pulsed glow discharges in air and nitrogen at atmospheric pressure have been extensively studied at Stanford University over the past few years, both experimentally and theoretically. [1-19] The objective of these studies was to provide a clear understanding of the mechanisms of ionization and recombination in atmospheric pressure air and nitrogen plasmas.

Spatially and temporally resolved diagnostics, including quantitative Optical Emission Spectroscopy (OES) and Cavity Ring-Down Spectroscopy (CRDS), as well as electrical techniques, have been developed to measure the electron number density and the gas temperature in these discharges. [4, 8, 9, 14, 15, 20, 21]

2.2.1. Experimental

Atmospheric glow DC discharges are obtained by applying a few hundred volts to a few kilovolts between ballasted electrodes. A 15 kW DC power supply, Del High Voltage Model RHVS, capable of delivering up to 10 kV and 1.5 A, is employed, together with a ballast resistor of 3-50 kΩ in series with the discharge, as shown in Figure 1. The appropriate value of the ballast resistor is chosen according to the operating current in order to stabilize the discharge.

The DC discharges are typically applied between two platinum pins parallel to the axis of the gas flow. The pins are welded onto cooled stainless steel tubes in order to prevent their melting at the elevated temperature operation. Although the platinum pins are not required to operate the discharge, they help stabilize the discharge spatially.

Optical Diagnostics

Temperature and indirect electron number density measurements were made by means of spatially resolved optical emission spectroscopy. Spectra of the 2nd and 1st positive systems of N$_2$ (C$^3\Pi_u$-B$^3\Pi_g$ and B$^3\Pi_g$-A$^3\Sigma_u^+$), in some cases also 1st negative system of N$_2^+$ (B$^2\Sigma_u^+$- X$^2\Sigma_g^+$), NO γ system (A$^2\Sigma^+$-X$^2\Pi_r$), and OH system (A$^2\Sigma^+$-X$^2\Pi_{3/2}$), were used to determine the rotational and vibrational temperatures T_r and T_v, respectively, using the SPECAIR radiation code. [22-23] In atmospheric pressure plasmas, the T_r is close to the gas temperature, owing to fast collisional relaxation.

Spatially resolved optical emission spectroscopy of the discharge enables us to characterize its important properties. A schematic of the optical set-up used at Stanford is shown in Figure 1. Two spectroscopic devices were used, each of them with appropriate optics.

The first system uses an Ocean Optics S2000 dual spectrometer, fitted with two grating/CCD combinations. The two 1200 and 600 grooves/mm gratings provide coverage of the two spectral ranges: 200-500 nm, and 400-1050 nm, with respective wavelength resolutions of 0.41 and 0.88 nm. We use two independent optical trains separated by a small angle and focused to the same point in the discharge, one for UV, and the other for VIS-NIR spectral region. In

each train, light emitted from the discharge collected with two fused silica lenses is focused into a fiber optic connected to the respective spectrometer channel. The optical trains are mounted on a translation stage, which enables horizontal and vertical lateral scanning in both spectral regions simultaneously.
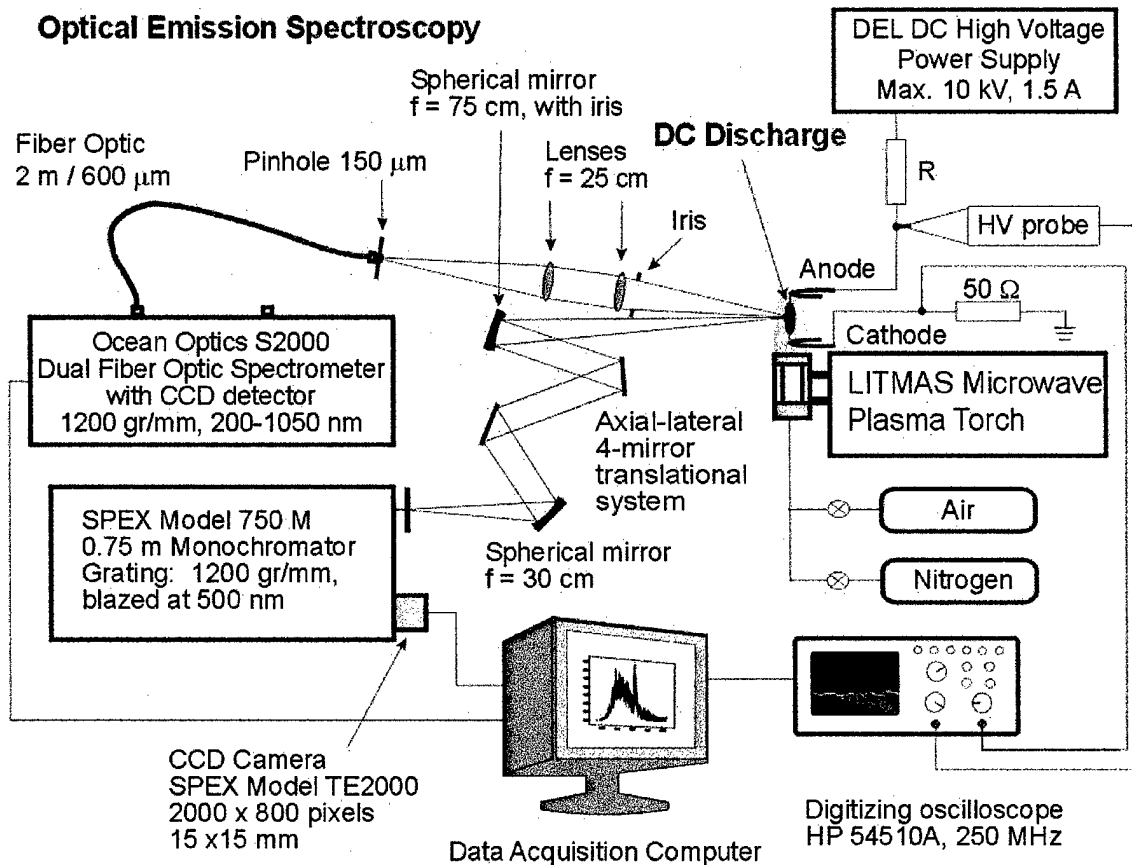
Figure 1. Overall view of the experimental setup for DC discharges and optical emission spectroscopy.

While the S2000 spectrometer described above provides quick but poorly resolved spectral scanning in the whole region between 200-1050 nm, we used an additional spectroscopic system providing better spectral resolution. It contains a 75-cm monochromator SPEX 750M (200-800 nm grating) fitted with a 2000 x 800 pixel CCD camera SPEX TE2000 (15 x 15 μm pixel dimension). Both monochromator, and the CCD camera were controlled by a PC (National Instruments Labview programs). The light emitted from the discharge is collected with a spherical mirror, translated using the 4-mirror translational system, and then focused by another spherical mirror onto the entrance slit of the monochromator. The best wavelength resolution of this system is 0.04 nm; we typically use 0.12 nm resolution, which is satisfactory to resolve the rotational structure of molecular spectra. This system also enables 2-dimensional scanning.

8

Furthermore, it allows taking wavelength-specific CCD camera images of the discharges that are useful for measuring the discharge diameter.

Absolute intensity calibrations for both used spectroscopic systems were obtained by means of two radiance standards traceable to NIST calibrations. Both systems in their typical settings provide a spatial resolution of 250 μm.

Besides emission spectroscopy we also used the digital camera Nikon Coolpix 990 for photo-documentation of discharges.

Microwave Plasma Torch

Experiments with DC and pulsed discharges were conducted in ambient and preheated air and nitrogen at atmospheric pressure. In the past we preheated air to about 2000 K with the 50 kW RF plasma torch (TAFA model 66). Experimental details may be found in Refs. [1-4, 8-11, 13] Now we preheat air with a microwave plasma torch (Litmas Red) powered by a 5 kW magnetron (Richardson Electronics switching power generator Model SM1050). The torch has a maximum power output of 3 kW, considerably lower than the previously used RF torch. The temperature and velocity of the outgoing plasma can be set by varying the power output and gas flow rate, as well as by using water-cooled test sections and nozzles. The torch is able to generate air plasmas in the temperature range 750-4700 K at flow velocities from 20 to 200 m/s, corresponding to gas flow rates from 8 to 110 slpm (standard liters per minute). The microwave torch head and a close-up view of the air plasma plume at typical experimental conditions (T~2000 K, v~160 m/s) are shown in Figure 2.
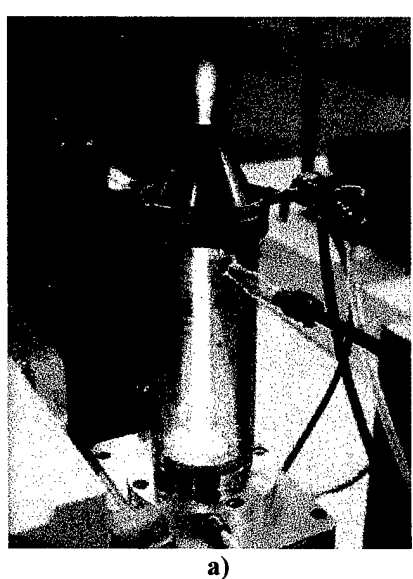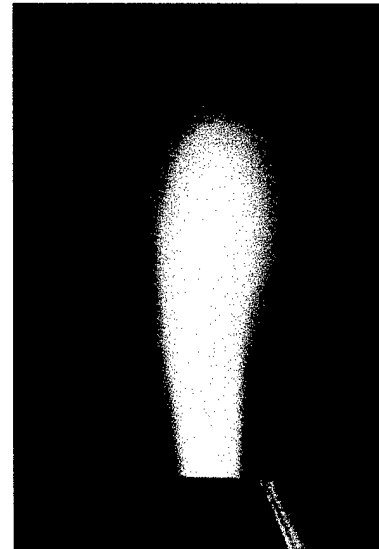
a)   b)

Figure 2. a) Microwave plasma torch head, test-section, and accelerating nozzle (exit diameter 1 cm). b) air plasma plume at the exit of the 1 cm diameter nozzle.

9

2.2.2. DC Discharges in Ambient Air

Atmospheric glow DC discharges are obtained by applying a few hundred volts to a few kilovolts between ballasted electrodes. A 15 kW DC power supply, Del High Voltage Model RHVS, capable of delivering up to 10 kV and 1.5 A, is employed, together with a ballast resistor of 3-50 kΩ (typically 18 kΩ) in series with the discharge, as shown in Figure 1.

Figure 3a shows a picture of a typical DC glow discharge in ambient air at atmospheric pressure. A DC glow discharge in nitrogen at the same conditions is also shown for comparison (Figure 3b). The gas (either air or nitrogen) is injected at about 0.5 m/s between two electrodes separated by 1.2 cm. The air discharge voltage and current are 1.5 kV and 100 mA, respectively. The stratification into dark and bright layers typical of low pressure glow discharges is also observed at atmospheric pressure, especially at currents below 20 mA. Note for instance the Faraday dark space near the cathode (lower electrode) in the nitrogen discharge (Figure 3b) Nevertheless, the cathode layers are concentrated in the immediate vicinity of the cathode, thus suggesting that the positive column occupies most of the interelectrode space. This observation was confirmed by electrical measurements. The electric field strength is found to be uniform and equal to approximately 935 V/cm in the interelectrode space, except within the 1 mm region close to the cathode. The voltage drop across the cathode region is about 280 V, a value typical of the cathode fall in air glow discharges with Pt electrodes. [24]

The diameter of the discharge in air measured by emission spectroscopy of the N_2 $C^3\Pi_u$-$B^3\Pi_g$ (0,0) at 337 nm is approximately 1.7 mm for the current of 100 mA. The same discharge diameter was measured for the nitrogen discharge of the same conditions. Since the C state of N_2 is produced by electron-impact excitation, this diameter is representative of the region with high electron number density. An experimental validation of this spectroscopic method of the discharge diameter measurement will be provided in Section 2.3. In Figure 3, the discharge in air appears to be wider than the discharge in nitrogen. This effect is due to the presence of a halo around the discharge produced by NO_2 emission in the surrounding air environment heated by the discharge. The measured gas temperature in the discharge channel at these conditions is about 2500 K, and the estimated electron temperature is around 9500 K. This thermal nonequilibrium provides further indication that the discharge is a glow and not an arc.

The DC glow discharges in ambient air flows can be operated in the current range from 2 to 500 mA or even higher. The corresponding gas temperatures, measured by optical emission spectroscopy at the centerline of the discharge column, start at 1500 K, up to 4000 K, depending strongly on the gas velocity. The current-voltage characteristic of the discharges in ambient air is descending. The gap length can be varied from few mm to few cm, depending on the flow velocity of the gas and the discharge current. Plasma volumes of ~0.5 cm^3 can be produced in this manner.

The conductivity, hence the electron number density, can be obtained using Ohm's law and the measured electric field strength and current density (determined from the measured

10

discharge current and discharge diameter). We estimated the electron number density n_e to be approximately 10^{12} cm^{-3}. This value agrees well with the n_e measured by Cavity Ring-Down Spectroscopy of N_2^+, the dominant ion in nitrogen glow discharges. [15]

a) air   **b) N$_2$**
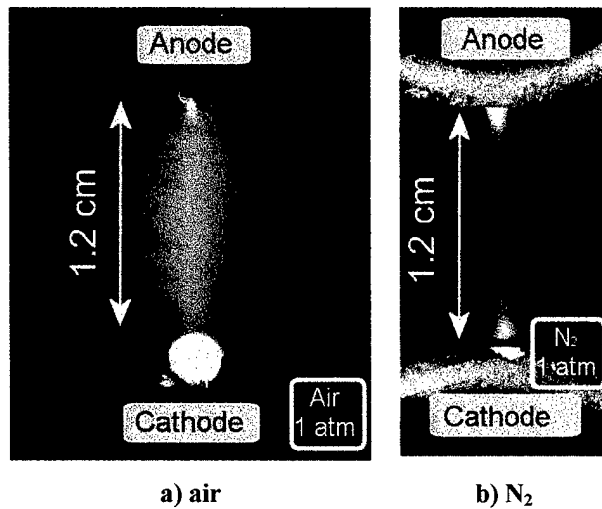
Figure 3. DC glow discharge in a) air and b) nitrogen flow (v = 0.5 m/s) at room temperature and atmospheric pressure. I = 100 mA, U = 1.5 kV in air, 1.4 kV in N$_2$.

2.2.3. DC Discharges in Fast Flow of Preheated Air

DC discharge experiments were also conducted with fast flowing preheated air at ~2000 K. The main reason for going to fast gas flows (20-400 m/s) is that discharges in slow flows result in significant gas heating, especially at high currents where electron number densities of 10^{12} cm^{-3} or higher are achieved. The mechanism of gas heating can be explained as follows.

In the DC discharges, a large fraction of the electron energy is lost via excitation of the vibrational modes of air molecules, mainly N$_2$. These vibrational modes subsequently relax through collisions with the dominant species, i.e. O, N$_2$, and O$_2$. This collisional quenching transfers the energy from vibration into the translational modes of molecules, which results in Joule heating of the gas. This process is called vibrational-translational energy transfer (VT transfer). In slow air flows, the residence time of the gas in the discharge is long enough to enable the VT transfer. As a result, the gas is heated.

In fast air flows, on the other hand, the vibrational modes of N$_2$ have shorter time to relax, hence cannot heat the gas as much over the short residence time between the two electrodes. Thus the temperature in the discharge is almost determined by the inlet gas flow. Yet, it is very difficult to maintain stable DC discharges in fast flows of ambient air. This is because electron attachment is fast, whereas ionization is slow since the reduced field strength E/N (where E is the field strength and N is the gas density) is lower due to the lower gas temperature, hence higher N.

11

For these reasons, we used a fast flow of preheated air at ~2000 K. At this temperature, electron attachment does not play an important role. Moreover, the density is about seven times lower than at room temperature and the reduced field strength E/N is sufficient to maintain the discharge. When the residence time of the flow in the discharge column is shorter than the characteristic time for VT relaxation, the temperature remains close to 2000 K.

(a)   **(b)**
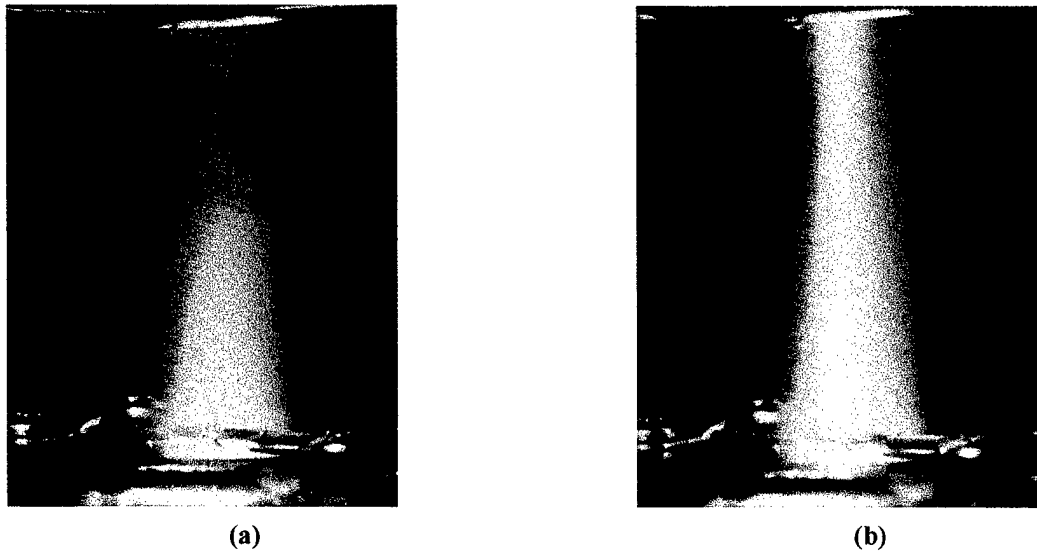
Figure 4. Air plasma at 2300 K: a)without discharge. b) with discharge (1.4 kV/cm, 200 mA). Interelectrode gap 3.5 cm.

Figure 4 shows photographs of an air plasma plume preheated to ~2000 K by means of the RF torch (Figure 4a) and of the same plume with a DC discharge applied (Figure 4b). In these experiments, the interelectrode distance is about 3.5 cm, and the discharge diameter measured by the emission of the N_2 C-B transition is 3.2 mm. The discharge diameter is larger in preheated air than in ambient air. This effect is most likely due to the presence of larger dissipative thermal gradients in the ambient air discharge than in the preheated air plume. In addition, electron attachment may become important at the low temperature discharge boundaries in ambient air experiments.

2.2.4. Repetitively Pulsed Discharge in Preheated Air

As the power required to sustain elevated electron densities (~10^{12} cm^{-3}) with DC discharges is large, a power reduction strategy based on pulsed electron heating was explored. [8, 11-13] This strategy is illustrated in Figure 5. Short (10 ns) high voltage pulses (10 kV) are applied to increase the electron number density. After each pulse, the n_e decreases according to electron recombination processes. When the n_e reaches the minimum desired value, the next

12

pulse is applied. The average electron density obtained with this method depends on the pulse duration, pulse voltage, and the interval between pulses.

A repetitive pulser capable of generating 10 ns pulses, with peak voltages of 3-12 kV and pulse repetition frequencies up to 100 kHz from Moose-Hill/FID Technologies was used. The electric circuit and the pulser were described elsewhere. [8,11,13] The discharge is applied in atmospheric pressure air preheated to about 2000 K. The power deposited into the plasma by the discharge was determined from the pulse current (measured with a Rogowski coil), the voltage between the electrodes minus the cathode potential fall, and the measured discharge diameter.
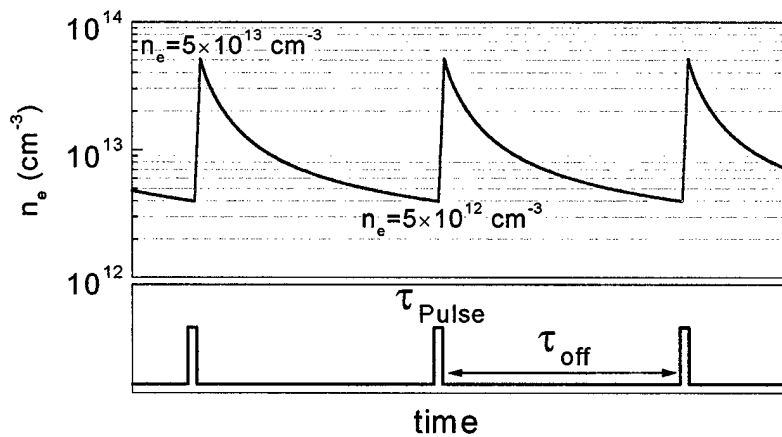
Figure 5. Repetitively pulsed strategy
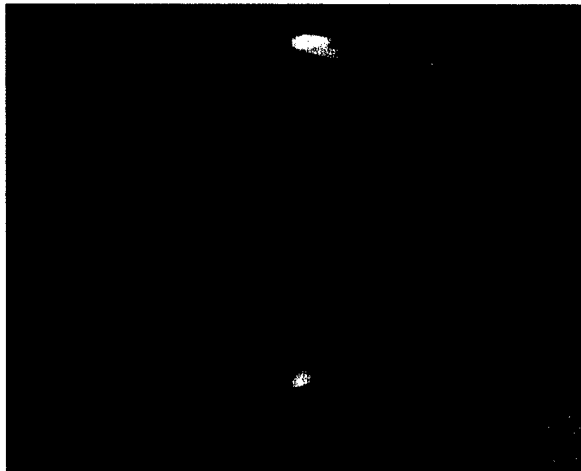
Figure 6. Photograph of 10 ns, 100 kHz repetitively pulsed discharge in preheated air at 2000 K and 1 atm. Interelectrode distance 1.2 cm. Discharge diameter 3.2 mm.

Figure 6 shows a picture of the repetitively pulsed discharge in preheated air at ~2000 K. Here the interelectrode distance is 1.2 cm, and the discharge diameter is about 3.2 mm, which is comparable to the diameter of the DC discharge in preheated air. The measured electron number density varies from 7×10^{11} to 1.7×10^{12} cm^{-3}, with an average value of about 10^{12} cm^{-3}. The power

deposited into the discharge is measured to be 12 W/cm^3, consistent with the theoretical value of 9 W/cm^3 for an optimized pulsed discharge producing 10^{12} electrons/cm^3. [8,13] It is lower, by a factor of 250, than the power of 3 kW/cm^3 required to sustain 10^{12} electrons/cm^3 with a DC discharge. More details about the pulsed discharge experiments and modeling can be found in the final report of the MURI program and elsewhere. [8, 11-13]

2.3. Characterization of the Diameter of a DC Discharge in Ambient Nitrogen

Experimental investigations of gas discharges involve the determination of various parameters including the electric field strength and the current density. The electric field strength can be measured from the electric potential difference between adjacent locations in the plasma. The current density j is usually obtained by dividing the total current by the cross-section area of the discharge. The discharge diameter, however, is often a vague concept. In our MURI work, we have defined the diameter as the full width at half maximum (FWHM) of the emission profile of an excited molecular state such as the C state of N$_2$. Here, we investigated whether excited state emission profiles can provide a reasonable estimate of the electron density profile, and thus of the discharge diameter. We now provide an experimental justification of this assumption.

We apply two spatially resolved diagnostic techniques, Optical Emission Spectroscopy (OES) and Cavity Ring-Down Spectroscopy (CRDS), coupled with a collisional-radiative (C-R) model for nonequilibrium nitrogen plasmas, to characterize the nitrogen discharge column. OES is used to measure the spatial emission profiles of excited N$_2$ and N$_2^+$ states, and the gas temperature profiles. CRDS provides the spatial absorption profiles of the N$_2^+$ ground vibronic state concentrations. A C-R model is employed to infer the total concentrations of N$_2^+$ and N$^+$ from the N$_2^+$ X (v=0) concentration profiles found by CRDS. At respective discharge currents of 97 and 187 mA we measure centerline electron number densities (sum of N$_2^+$ and N$^+$ concentrations) of 1.6±0.3 x10^{12} and 5.0±0.7 x10^{12} cm^{-3}. A comparison of the spatial electron number density profiles with the emission profiles yields reasonable agreement. We review the previous experimental results, and describe modifications implemented in the modeling part. Our results confirm that the plasma emission profiles are coincident with the electron density profiles and thus can be used to determine the discharge diameter.

2.3.1 Experimental

The experiments presented in this section were performed with an atmospheric pressure nitrogen DC discharge. A photograph of the discharge is shown in Figure 7. Nitrogen is injected through a flow straightener and passes through the discharge region with a velocity of about 20 cm/s. The discharge is generated between a pair of platinum pins that are vertically mounted on

14

water-cooled stainless-steel tubes. The discharge is maintained by a DC current supply (I_{max} = 250 mA) in a ballasted circuit (R_b = 9.35 kΩ). The pins are brought together to ignite the discharge, and are then separated to 8.5 mm using a translation stage. The positive column plasma occupies most of the discharge space, therefore all the spectroscopic diagnostics described in the following sections apply to the discharge column. The discharge is contained within a plexiglass cylinder (diameter 30 cm) that isolates it from ambient room air disturbances. Small holes allow weak ventilation by a fan through the top to avoid accumulation of undesirable by-products of the discharge, and enable passage of the laser beam through the discharge. A second translation stage is used to displace the entire discharge cylinder relative to the optical axis in order to obtain spatial profiles.
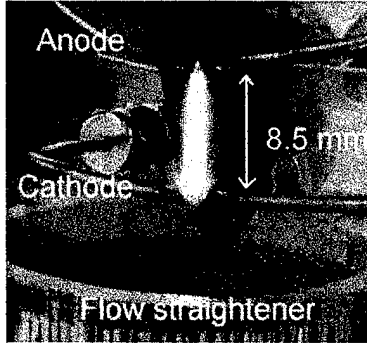
Figure 7. **Photograph of the atmospheric pressure nitrogen DC discharge. Electrode separation: 8.5 mm, discharge current: 187 mA, nitrogen gas flow velocity: 0.2 m/s.**

2.3.2. Cavity Ring-Down Spectroscopy (CRDS) measurements

We measured the N_2^+ ion concentration by probing the (0,0) band of its first negative system (B $^2\Sigma_u^+$ – X $^2\Sigma_g^+$) in the vicinity of 391 nm. The optical layout is shown in Figure 8. An OPO system (doubled idler) is used as the light source (repetition rate = 10 Hz, pulse width ~7 ns, pulse energy ~3 mJ, linewidth ~0.14 cm^{-1}). The output from the OPO passes through a Glan-Taylor polarizer to attenuate the energy, and several beam shaping optics to approximately mode-match the beam into the cavity. We use a linear cavity of 75-cm length with 50-cm radius-of-curvature (ROC) mirrors. The selection of cavity geometry is discussed in Ref. [15]. Typically, about 100 µJ per pulse is incident on the back face of the entrance ring-down mirror. The ring-down signal is collected behind the output mirror with a fast photomultiplier tube (Hammamatsu-R1104), which we filter against the pump laser and other luminosity with two narrow-band interference filters (CVI-F10-390-4-1). The PMT signals are passed to a digitizing oscilloscope (HP 54510A, 250 MHz analog bandwidth, 8-bit vertical resolution) and are read to computer with custom data acquisition software. In a typical ring-down spectrum, 16 or 32 decay curves are averaged at each wavelength, and the resulting waveform is fitted with an exponential to yield the ring-down time τ. The portion of the ring-down signal used in the fit is that in between 90% and 10% of the peak (initial) signal amplitude. The detuned ring-down time

τ_0 is determined with the laser tuned off the absorption features. Spectral scans use a step-size of 0.001 nm. The spatial resolution of our measurements is determined by the spatial step-size, and is approximately 0.2 mm.
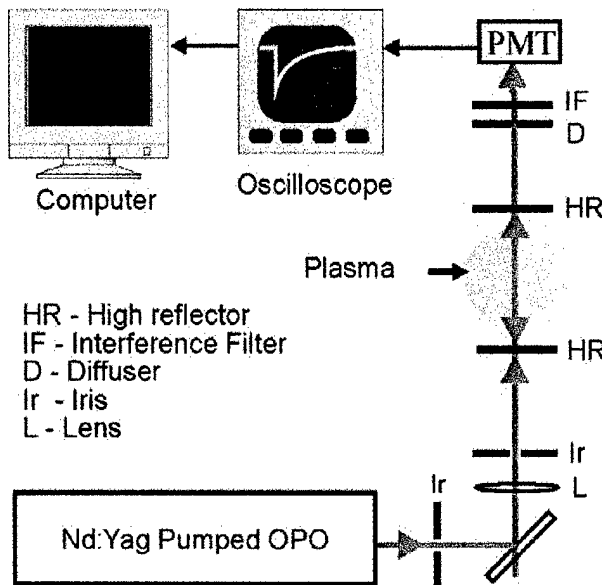
Figure 8 Schematic diagram of CRDS set-up. The ring-down cavity has a length of 0.75 m, and uses 0.5-m radius of curvature mirrors. An OPO is used as the light source, and a photomultiplier tube (PMT) detects the light exiting the cavity.

N_2^+ ring-down spectra are recorded as a function of discharge current and position. Figure 9 shows measured and simulated absorption spectra in the vicinity of the (0,0) bandhead of the first negative system. Rotationally resolved lines from the P and R branches are visible. The lines are identified using tabulated line locations [25-26], and are labeled with the angular momentum quantum number N" of the lower state. The displayed spectrum is recorded along the discharge centerline, at a current of 187 mA, and averages 16 shots at each wavelength.

We obtain spatial profiles of the $[N_2^+ X (v=0)]$, square brackets designating concentration, by displacing the discharge perpendicularly to the optical axis. CRDS is a path-integrated technique and the discharge has axial symmetry. We verify the symmetry of the discharge by performing measurements with the plasma rotated by 90 degrees, and find that the cases have <2% deviation. We use an Abel inversion to recover the radial $N_2^+X (v=0)$ concentration profile. The concentration measurements are based on the (frequency integrated) area of the lines P(9)-P(17) in the (0,0) bandhead vicinity. We use tabulated line strengths from Refs. [25-26]. Figure 10 shows $[N_2^+X (v=0)]$ profiles determined for different values of current ($I = 97$ and 187 mA). We find peak (centerline) $[N_2^+ X (v=0)]$ of 5.34×10^{11} and 1.11×10^{12} cm^{-3} for $I = 97$ and 187 mA, respectively. The shape of the concentration profile remains approximately uniform at the different conditions, though we observe that the radial half-maximum values increase slightly

with current. We find radial half-maximums of 0.82, and 1.05 mm for $I = 97$ and 187 mA, respectively. The error bars on $[N_2^+ X (v=0)]$ represent one standard deviation (1σ). These uncertainties account for the laser beam waist, and the beam walk caused by index-of-refraction gradients in the cavity.
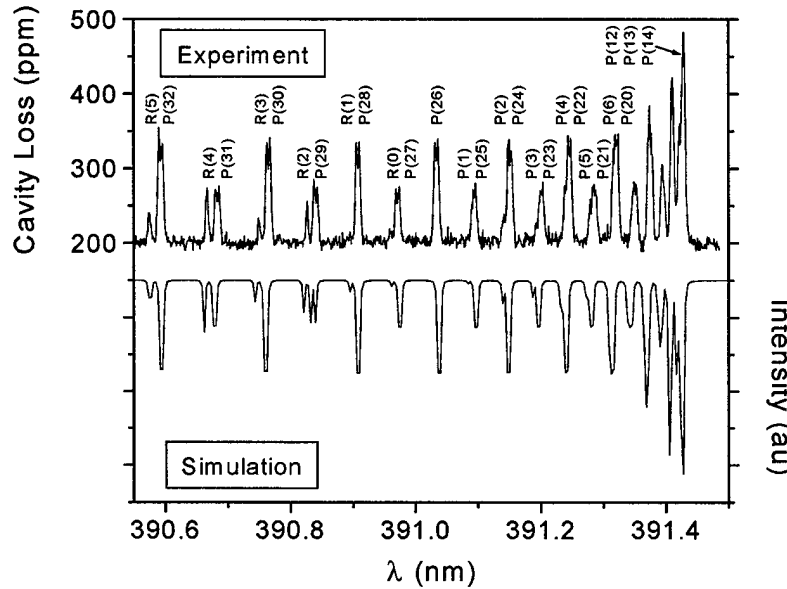
Figure 9 Measured and simulated N_2^+ absorption spectra near the (0,0) bandhead of the N_2 1st negative system. Lines from the P and R branches are identified.
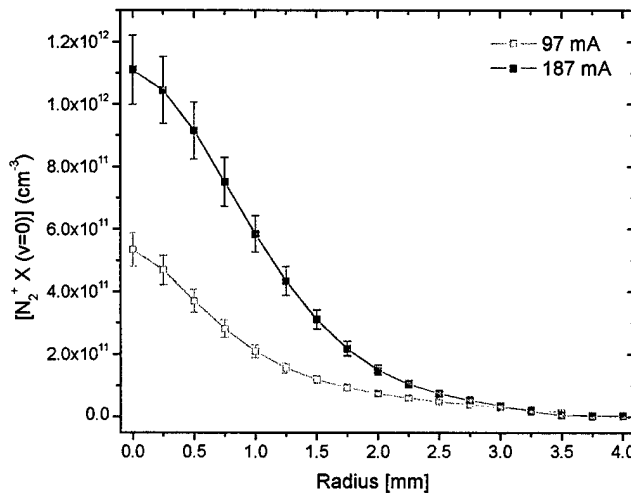
Figure 10 Abel-inverted radial concentration profiles of N_2^+ X (v=0) concentration measured by CRDS in an atmospheric pressure nitrogen DC glow discharge.

17

2.3.3. Optical Emission Spectroscopy (OES) Measurements

The simultaneous optical emission measurements were performed by the system shown in Figure 1 and described in Section 2.2.1. Figure 11 shows the line-of-sight emission spectrum recorded in the ultraviolet region for a discharge current of 187 mA. The most prominent features are the N_2 C-B (second positive system), and the N_2^+ B-X (first negative system). Figure 12 shows the spectrum recorded in the visible and near-infrared regions at the same current. The dominant emission system is the N_2 B-A (first positive system). Note that the ultraviolet bands of N_2^+ B-X appear as a second order interference.
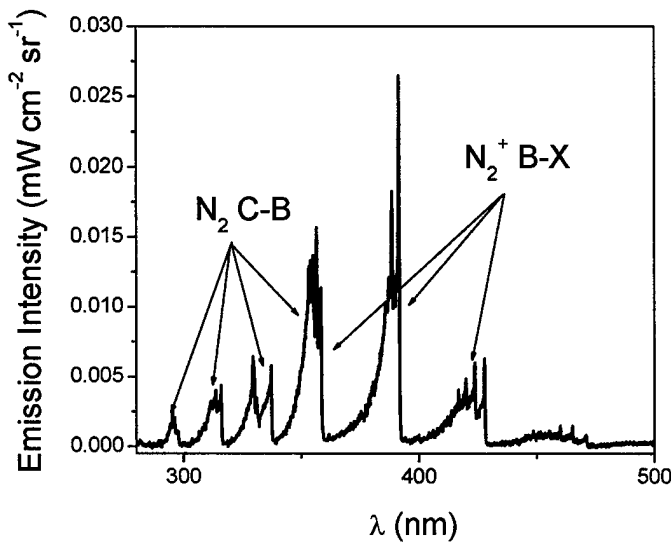
Figure 11. UV emission spectrum from the center of the nitrogen discharge. I = 187 mA.
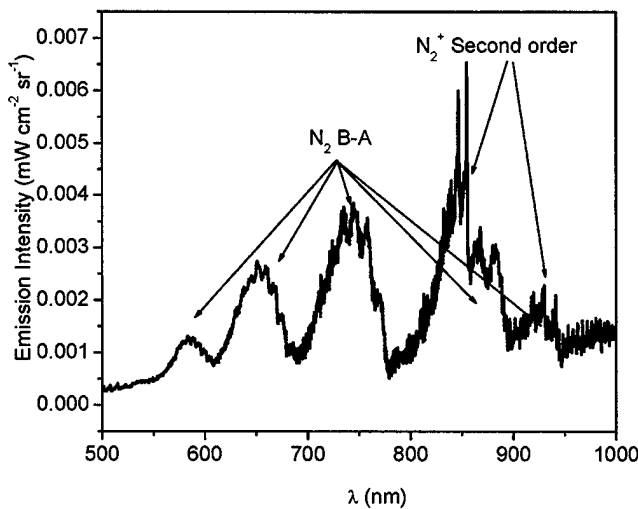
Figure 12. VIS/NIR emission spectrum from the center of the nitrogen discharge (I = 187 mA), showing bands of the N_2 B-A system.

18

2.3.2 N_2^+ and N_2 Emission Intensity Profiles measured by OES

Emission spectra of the 2nd and 1st positive systems of N_2 ($C^3\Pi_u$-$B^3\Pi_g$ and $B^3\Pi_g$-$A^3\Sigma_u^+$), and 1st negative system of N_2^+ ($B^2\Sigma_u^+$- $X^2\Sigma_g^+$) were collected from the discharge as a function of discharge current and position. We obtain spatial profiles of emission intensity by displacing the discharge perpendicularly to the optical axis. The spectra are placed on an absolute intensity scale after calibration with the radiance standards. Like CRDS, OES is a path-integrated technique and the discharge has an axial symmetry. Therefore, we use an Abel inversion to recover the radial intensity profiles. The absolute emission intensity of a particular molecular band is directly proportional to the population of the corresponding excited vibronic state, e.g. the intensity of the N_2^+ B-X (0,0) band is proportional to the concentration of N_2^+ B (v=0).

Figure 13 and Figure 14 compare normalized Abel-inverted emission intensity profiles of N_2^+ B, N_2 C, and N_2 B states with the normalized N_2^+ X (v=0) concentration profile measured by CRDS for currents of 97 and 187 mA. The three excited state profiles are practically identical. We find radial HWHM (half-width at half-maximum) of 0.63, 0.59, 0.59, and 0.59, 0.64, 0.67 mm, for N_2^+ B (v=0), N_2 C (v=0), and N_2 B, respectively, and respective currents 97 and 187 mA. On the other hand, the ground state N_2^+ X (v=0) profiles measured by the CRDS are broader, with HWHM = 0.82 and 1.05 mm for I = 97 and 187 mA, respectively. This result indicates that the spatial distribution of the ground and excited states are not the same.
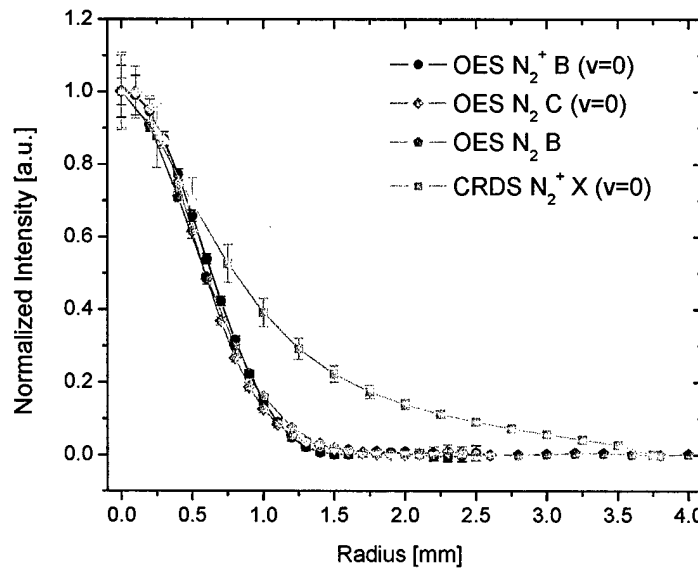
Figure 13. Normalized Abel-inverted emission and CRDS absorption radial profiles in the nitrogen DC glow discharge, I = 97 mA.

19
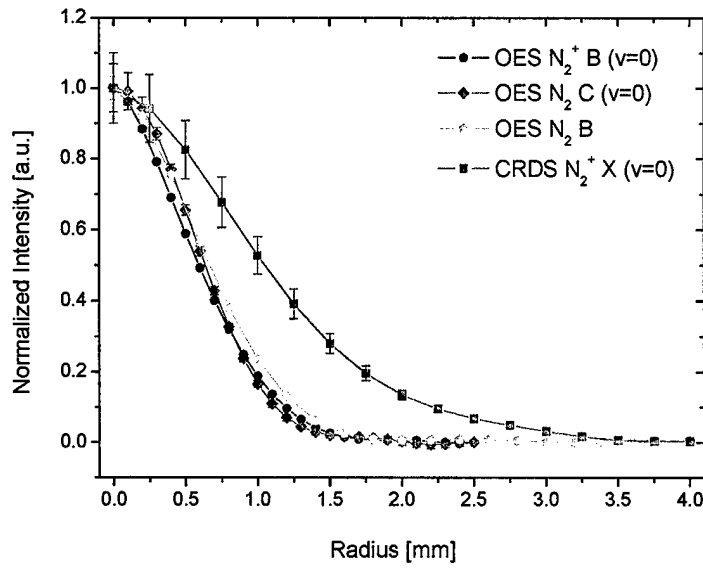
Figure 14. Normalized Abel-inverted emission and CRDS absorption radial profiles in the nitrogen DC glow discharge, I = 187 mA.

2.3.3 Gas temperature profiles measured by OES
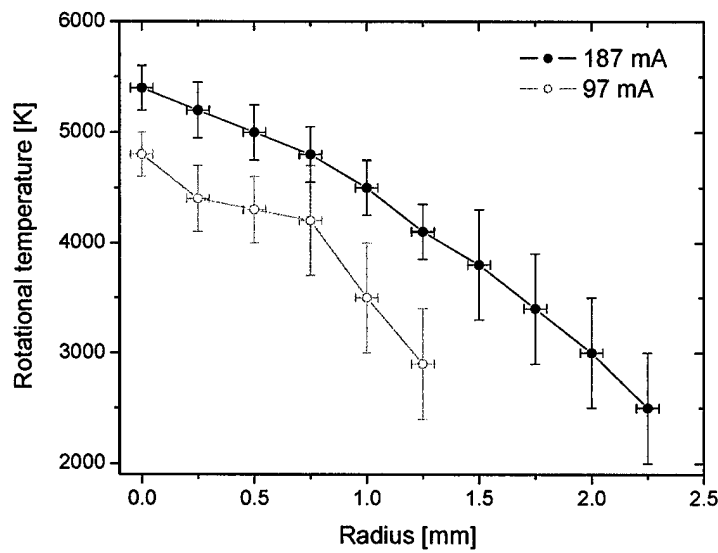
Figure 15. Rotational temperature radial profiles in the nitrogen DC glow discharge.

The spatially resolved N_2 (C-B) and N_2^+ (B-X) emission spectra are used to determine the rotational temperature profile in the discharge, using the SPECAIR radiation code [22-23] The

measured profiles are shown in Figure 15. In atmospheric pressure plasmas, rotational temperature is equal to the gas temperature owing to fast collisional relaxation. The error bars of the measured $T_r = T_g$ values rise with increasing radial position due to the decreasing emission intensity of N_2 and N_2^+ bands (and increase in noise). As a check of the OES temperatures, the rotational temperature profile at 187 mA was also measured by CRDS using a Boltzmann analysis of individually resolved rotational lines of the ground vibronic state of N_2^+. The CRDS temperature profile is slightly higher by about 200-400 K, but this does not appreciably change the results.

2.3.4 N_2^+ and N^+ concentration profiles calculated by C-R model

Spatial profiles of [N_2^+ X (v=0)] measured by CRDS were used to infer the total concentration of N_2^+ and N^+ by means of the collisional-radiative (C-R) model for nonequilibrium nitrogen plasma. [5] Since N_2^+ and N^+ are the dominant ions in the pure nitrogen plasma, the electron number density n_e is given by:

$$n_e = [N_2^+] + [N^+].$$

The basic input parameters of the C-R model are the gas and electron temperatures, T_g and T_e. We first run the model with the gas temperature measured by OES for each current and radial position in the discharge and with an estimated T_e value (we typically start with 10000 K). We compare the predicted [N_2^+ X (v=0)] with the experimental value measured by CRDS. We then refine the T_e setting in the model iteratively to obtain the best match between the calculated and the experimental [N_2^+ X (v=0)] value. The resulting T_e ranges between 8000 and 10100 K except at the centerline of the high current discharge ($I = 187$ mA, $r = 0$ mm) where the plasma gets close to thermal equilibrium ($T_e \approx T_g \approx 5400$ K). Over most of the plasma extent, however, the electron temperature is elevated relative to the gas temperature, which indicates that the plasma is out of thermal equilibrium, and therefore the discharge is of the glow type.

A similar procedure was used previously [15] to infer n_e from the CRDS-measured value of [N_2^+ X (v=0)]. However, two improvements are implemented here:

We use the gas temperature profile measured by OES (Figure 15) to determine [N_2^+] and [N^+], whereas in Ref. [15] an average constant temperature (3600 K and 4700 K for $I = 97$ and 187 mA, respectively) was employed.

The radiation escape factor in the C-R model is taken equal to unity for all transitions, i.e. plasma is considered optically thin, whereas in Ref. [15] the plasma was erroneously considered optically thick. This modification leads to an increase of the predicted ratios of [N_2^+ X (v=0)]/[N_2^+].
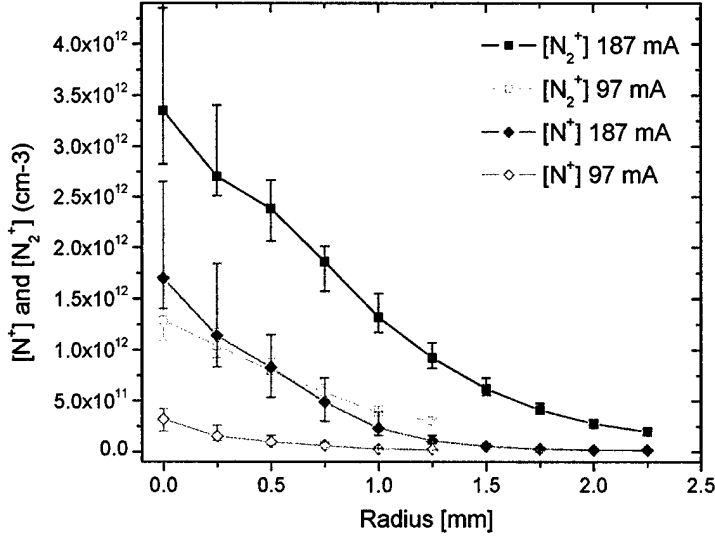
Figure 16. Predicted radial profiles of N_2^+ and N^+ concentrations in the nitrogen DC glow discharge.

The calculated $[N_2^+]$ and $[N^+]$ profiles for both currents are shown in Figure 16. The upper and lower limits of calculated $[N_2^+]$ and $[N^+]$ values represented by the asymmetric error bars are extreme cases accounting for the uncertainty of the OES-measured T_g (between 200 and 500 K, depending on the radial position), and the CRDS-measured $[N_2^+ X (v=0)]$ (about 10%). Although N_2^+ is the dominant ion, the concentration of N^+ ions becomes quite important in the high temperature region close to the plasma center, especially at $I = 187$ mA. The N^+ ions thus sharpen the radial profiles of total ion concentration, i.e. n_e profiles. The centerline n_e values are now equal to $1.6 \pm 0.3 \times 10^{12}$ and $5.0 \pm 0.7 \times 10^{12}$ cm^{-3} for $I = 97$ and 187 mA, respectively. The results reported in Ref. [15], without the improved modeling described above, yielded comparable values of $1.6 \pm 0.2 \times 10^{12}$ and $4.2 \pm 0.4 \times 10^{12}$ cm^{-3} for $I = 97$ and 187 mA; however, the revised values are preferable for the reasons discussed.

2.3.5 Comparison of n_e profiles with optical emission profiles

Figure 17 and Figure 18 show the normalized calculated n_e radial profile (i.e. $[N_2^+]+[N^+]$ profile) and the normalized emission intensity profile of N_2 C for $I = 97$ and 187 mA, respectively. We have selected the N_2 C profile as being representative of all the excited state profiles since they are all very similar as can be seen from Figure 13 and Figure 14. The asymmetric error bars in Figure 17 and Figure 18 correspond to the extreme limits of calculated $[N_2^+]$ and $[N^+]$ accounting for aforementioned uncertainties of T_g and $[N_2^+ X (v=0)]$.

It is informative to compare the normalized n_e and N_2^+ B intensity profiles. Although the two profiles are different at large radii, they are in reasonable agreement near the discharge

22

center. In particular, the radial HWHM of the emission profile is very close to the HWHM of the n_e profile: for $I = 97$ mA, the radius (HWHM) of the emission profiles equal to 0.63 ± 0.02 mm and the radius of the n_e profile is 0.61 ± 0.13 mm. Similarly, for $I = 187$ mA, we find a radius of 0.59 ± 0.02 mm for the N_2^+ B profile, and of 0.61 ± 0.15 mm for the n_e profile. The emission profile is found to be very similar to the electron density profile and therefore provides a reliable measurement of the plasma radius. These results support the use of emission spectroscopy as a tool for measuring the plasma extent.
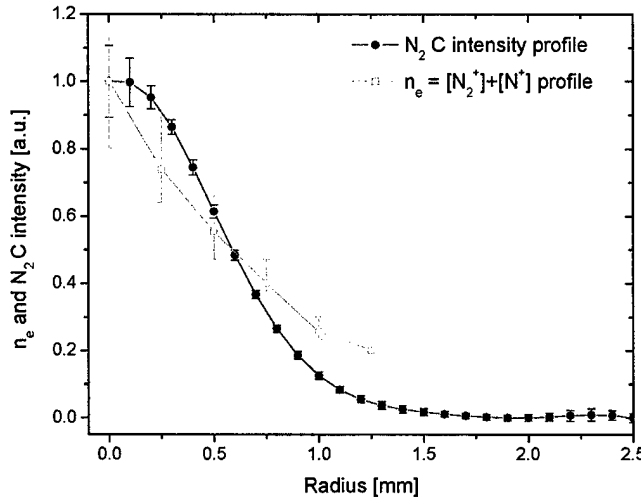
Figure 17. Normalized electron number density profile (inferred from CRDS) vs. normalized Abel-inverted N_2 C emission intensity profile , I = 97 mA.
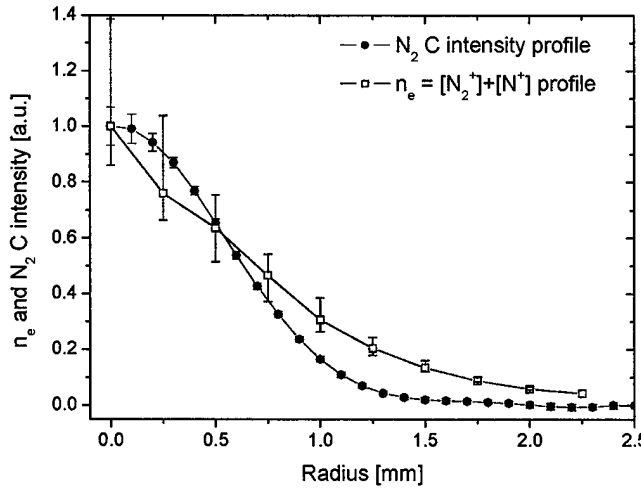
Figure 18. Normalized electron number density profile (inferred from CRDS) vs. normalized Abel-inverted N_2 C emission intensity profile , I = 187 mA.

23

2.4. Numerical Simulation of the Radial Current Density Profiles in a DC Discharge in Preheated Air

In the experiments presented in Section 2.2, we have shown that the discharges produced in preheated air at ~2000 K were diffuse, and approximately 3.5 cm in length and 3.2 mm in diameter. To understand the effects controlling the diameter of the discharge, we have developed a simple model of a discharge generated between a pin anode and a pin cathode. The model is described in Sections 2.4.1 and 2.4.2, and the modeling results are presented in Section 2.4.3.

2.4.1. Equations

The discharge size is controlled by several factors including the non-resistive behavior embedded in the electrical j-E discharge characteristics (see Figure 19), the flow field properties, and ambipolar diffusion. In this Section, we examine the effects of the non-resistive discharge characteristics on the discharge diameter.
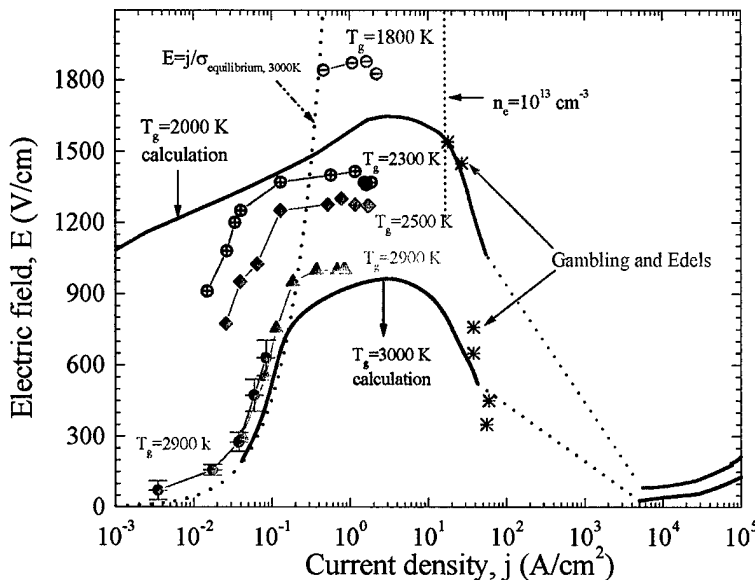
Figure 19. Measured (symbols) and predicted (solid lines) electrical discharge characteristics in atmospheric pressure air plasmas generated by DC electric discharges. [9-10]

Using Faraday's law for a plasma with no magnetic field:

$$\nabla \times \vec{E} = 0,$$

we obtain the following relation:

$$\vec{E} = -\nabla \phi, \tag{1}$$

where E is the electric field and ϕ is the electric potential.

The steady-state current continuity equation reads:

$$\nabla \cdot \vec{j} = 0 \tag{2}$$

24

We use Ohm's law to relate the current density j and the electric field E:

$$j = \sigma E,$$ (3)

where σ is the electrical conductivity.

Combining equations (1)-(3), we obtain:

$$\nabla \cdot (\sigma \nabla \phi) = 0,$$

or equivalently:

$$\nabla \ln(\sigma) \cdot \nabla \phi + \Delta \phi = 0.$$ (4)

From the non-resistive behavior of the j-E characteristics, we have

$$j = \sigma(j) E,$$ (5)

with

$$\sigma(j) = A \cdot j^{1-a},$$

where the constants a and A can be determined by fitting the experimental discharge characteristics of Figure 19.

Thus

$$j = (AE)^{1/a}$$
$$= j_0 \left(E/E_0 \right)^{1/a}$$
$$= \sigma_0 E^{1/a} E_0^{(a-1)/a}$$

Since $j = \sigma E$, we have:

$$\sigma = \sigma_0 \left(\frac{E_0}{E} \right)^{\left(\frac{a-1}{a} \right)}$$

We then obtain:

$$\nabla \ln(\sigma) = \left(\frac{1-a}{a} \right) \nabla \ln(E) = \left(\frac{a-1}{a} \right) \nabla \ln(\nabla \phi),$$

and we rewrite Equation (4) as:

$$\Delta \phi = -\nabla \ln(\sigma) \cdot \nabla \phi = \left(\frac{1-a}{a} \right) \nabla \ln(\nabla \phi) . \nabla \phi .$$ (6)

The nonlinear partial differential equation (6) is of the form:

$$\frac{\partial \rho}{\partial t} + \nabla \cdot (\rho \vec{u} \Psi) = \nabla . (\Gamma \cdot \nabla \Psi) + S_\Psi,$$ (7)

where the terms on the left side of the equation are the unsteady and convection terms respectively, and the terms on the right side are the diffusion and source terms respectively. ρ is the density and $\vec{u}$ the velocity vector. This equation can be solved using the SIMPLEC algorithm.

Thus equation (6) can be solved with the SIMPLEC algorithm by setting:

$$\begin{cases} \rho = 0 \\ \Gamma = 1 \\ S_\Psi = \left[(a-1)/a \right] \nabla \ln(\nabla \phi) . \nabla \phi \end{cases}$$

25

2.4.2 Boundary conditions and computational grid

We consider two metal pin electrodes of radius r_0 separated by a distance L. The computational domain uses a non-uniform grid with smaller mesh size near the electrodes, as shown in Figure 20.

Radial position (r)

Axial position (x)
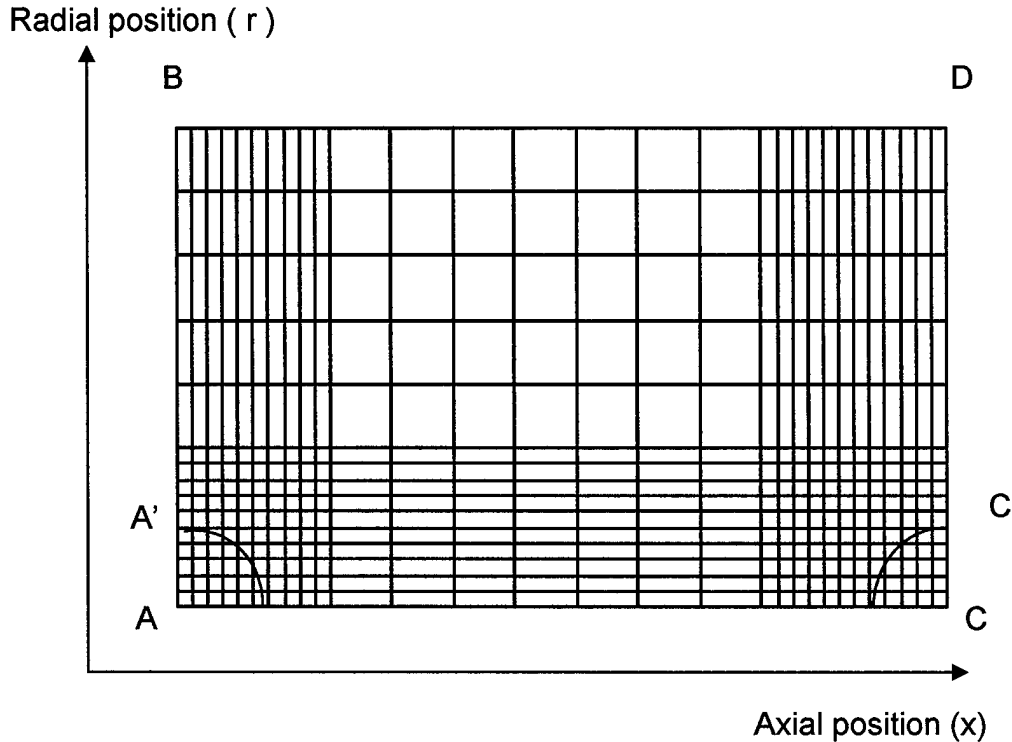
Figure 20. Schematic of the two-block grid used to model the two pin stationary DC discharge.

We assume that the anode (A) is at potential V_0 and the cathode (C) is at ground potential. We also assume that the system is 2D axi-symmetric. The boundary conditions outside the pins are:

$$\frac{\partial \phi}{\partial x} = 0, \text{ along the A'B and C'D boundaries,}$$

$$\frac{\partial \phi}{\partial r} = 0, \text{ along the AC and BD boundaries.}$$

2.4.3 Results and discussion

The potential distribution in the domain shown in Figure 20 was obtained by solving equation (6). From this solution, we determine the $j_X(r)$, the radial distribution of the current density, at various axial distances x. Figure 21 shows the normalized radial distributions of $j_X(r)$ in the plane located half way between the pins, for different values of the a parameter. As can be seen from Figure 21, the Half Width at Half Maximum (HWHM) of the radial current density profile decreases with decreasing values of a. Note that $a=1$ corresponds to the situation

26

where the pins are immersed in a purely resistive environment. In that case, σ is constant and independent of the discharge current density j.
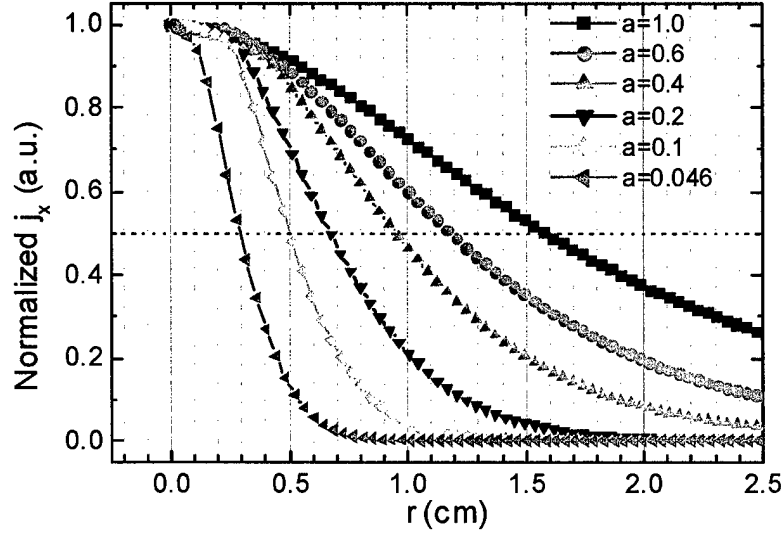
Figure 21. Normalized radial distributions of $j_x(r)$ in the plane located half way between the pins for different values of the a parameter.
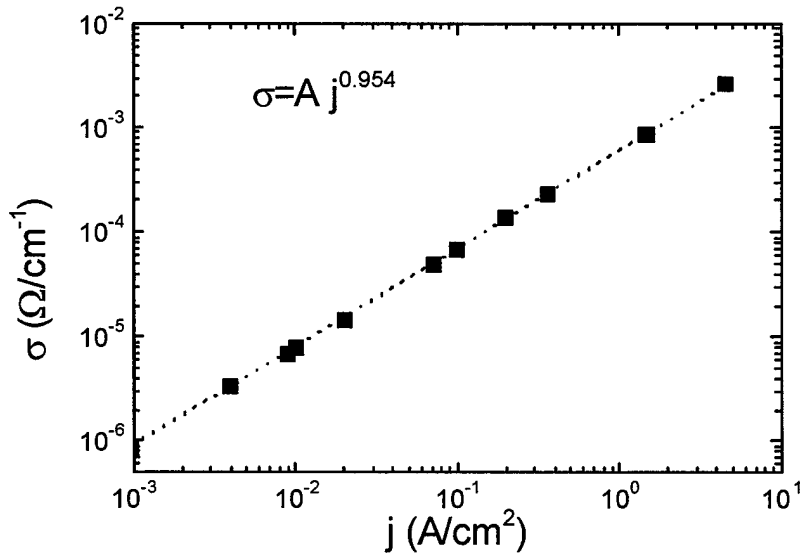
Figure 22. Fit of experimental j-E characteristics.

To compare the modeled and measured discharge sizes, we determine the a parameter from the experimental discharge characteristics. Figure 22 shows a fit of the experimental data of Figure 19. As can be seen in Figure 22, the best fit is obtained for a=0.046. From Figure 21 it can be seen that for a=0.046 the HWHM of $j_X(r)$ is predicted to be 2.8 mm. This value is in

agreement (within a factor two) with the experimental discharge radius which is measured to be 1.6 mm.

Simulations with different pin sizes were made to investigate the effect of the pin dimensions on the size of the discharge. The results show that the discharge diameter is independent of the pin diameter, as long as the distance between the two pins is much larger than their diameter. This result is in agreement with our experimental observations.

2.4.4. Conclusion

We conclude that the discharge size can be reasonably well predicted with the model presented in this section. The modeling results are within a factor of two of the measurements. To improve the model, flow field effects should be added to the model. This can be achieved by including the flow field variations in Equation (6).

2.5. Computational Analysis of Diffuse Discharges in Atmospheric Air

In this section, we present a more detailed computational analysis of the DC discharge experiments in preheated air. We focus on the radial spreading mechanism and carry out computational experiments with a three-temperature, finite-rate computational fluid dynamics code. We find that axisymmetric simulations of the jet are unstable, with the jet shear layer rolling up into vortical structures. The jet non-uniformities pinch the discharge which causes a breakdown into what appears to be an arc. This is contrary to the experimental observations, and therefore we postulate that turbulent mixing may increase the stability of the jet through enhanced mixing. We use an approximate formulation that produces a steady jet flow, resulting in stable diffuse discharges with reasonable experimental agreement. We then vary the flow parameters and find that laminar diffusive processes are too weak to produce much change in the discharge radius. The experiments described here were conducted in atmospheric air preheated to ~2000 K by the RF plasma torch. Experimental details may be found in Ref. [6]

2.5.1. Numerical Simulations

The DC discharge is modeled phenomenologically with a superimposed gas flow field. The flow field is described by the Navier-Stokes equations that have been extended to include the effects of nonequilibrium thermochemistry. Separate mass conservation equations for the each of the 11 chemical species are solved. Details of the chemistry modeling can be found in Ref. [4]. The energy of the flow is modeled by solving total energy, vibrational energy, and electron energy conservation equations. In general, the change of energy = divergence of energy flow + energy source terms.

28

$$\frac{\partial E}{\partial t} = -\nabla \cdot \left((E + p)\vec{u} + \vec{q} + \vec{u} \cdot \tilde{\tau} \right) + \frac{j^2}{\sigma}$$

$$\frac{\partial E_v}{\partial t} = -\nabla \cdot \left(E_v \vec{u} + \vec{q}_v \right) + Q_{T-v} + Q_{v-e} + \sum_s w_s e_{vs}$$

$$\frac{\partial E_e}{\partial t} = -\nabla \cdot \left(E_e \vec{u} + \vec{q}_e \right) + \frac{j^2}{\sigma} - Q_{h-e} - Q_{v-e} + w_e e_e$$

The heat flow vectors $\vec{q}$, $\vec{q}_v$, and $\vec{q}_e$, contain heat conduction and heat carried by mass diffusion. The semi-empirical formula of Blottner *et al.* [27] and curve fits provided by Gupta *et al.* [28] are used to obtain the energy transport properties. Unfortunately, for flows with bulk phenomena such as turbulent mixing, a general multi-component approach for transport properties is not available. This limitation will be discussed later in the report.

The energy transfer terms Q_{T-v}, Q_{h-e}, and Q_{v-e}, the translation-vibration energy transfer rate, the heavy-particle-electron energy transfer rate, and the vibration-electron energy transfer rate, respectively, are taken from Refs.[4, 6, 29]. The diffusional mass fluxes carry energy and are calculated per species using the explicit expression derived by Ramshaw [30] in his self-consistent effective binary diffusion approximation. The driving forces in this formulation are the species concentration gradients and the body forces acting on the charged species due to the ambipolar electric field. Ambipolar diffusion is included because concentration gradients of charged particles exist in regions of no current flow and their diffusion is curbed by the presence of neighboring charged particles. The first expansion of the binary diffusion coefficient, utilizing the weighted averages of the pair cross sections, is used.

The discharge is modeled as axisymmetric, with no Lorentz force and coincident axial electric current. The electric field influences the total energy and the electron energy conservation equations through a Joule heating source term. The current is controlled experimentally, and is thus a prescribed parameter, which is conserved at each axial location. A flux of electrons is introduced at the cathode location. It is calculated from the total current in the discharge and the effective area of the cathode. Sheath details are not resolved, and the current is considered to be entirely carried by the electrons. Between the electrodes the charged particles are acted upon by the electric field. The flux of electrons passing through a unit area per unit time is

$$\Gamma_e = \rho_e \vec{\bar{u}}_e$$

where $\vec{\bar{u}}_e$ is the mean drift velocity and is related to the kinetic energy acquired by the electrons under the influence of the electric field. The mean drift velocity of the electrons depends on the electric field and the electron mobility, μ_e

$$\vec{\bar{u}}_e = \mu_e \vec{E}$$

The electron mobility is related to the collision frequency v_e, between electrons and heavy particles.

$$\mu_e = \frac{e}{m_e v_e}$$

For the experimental conditions, the ions have negligible concentrations and the collision frequency is approximated by

$$v_e = n v_{the} Q_{en}$$

where n is the number density and v_{the} is the thermal velocity of the electrons,

$$v_{the} = \sqrt{\frac{8kT_e}{\pi m_e}}$$

and the average cross-section Q_{en} is the average momentum transfer cross section taken to be 10^{-15} cm^2. The current density j, is determined according to the equation:

$$j \approx j_e = -e n_e \vec{\bar{u}}$$

where the mean drift velocity is obtained from the known total current, I, using

$$I = \int_A j\, dA \cong -e \vec{\bar{u}}_e(x) \int_A n_e\, dA$$

The integral is taken in the radial direction, and we assume that the mean drift velocity is only a function of the axial distance, x. This is essentially the classical channel model discussed in Ref. [24]. Finally, the electrical conductivity is defined using the calculated particle mobility and electron number density

$$\sigma = \mu_e e n_e$$

2.5.2. Numerical Method

Under the conditions of the DC discharge experiments, the energy relaxation processes are very fast relative to the fluid motion time scales and the chemical kinetic processes. We use a simple implicit method, in which only relatively fast terms (the internal energy relaxation and the Joule heating) are linearized. The conservation equations are written

$$\frac{\partial U}{\partial t} + \frac{\partial F}{\partial x} + \frac{1}{r}\frac{\partial rG}{\partial r} = W$$

where U is the vector of conserved variables, F and G are the flux vectors, and W is the source vector.

The inflow profile is based on the measured temperature distribution at the exit of the mixing section, where the flow is assumed to be in LTE. The static pressure and temperature are held fixed, and a characteristic relation is used to update the inflow velocity. In the converging portion of the nozzle, the wall temperature is held fixed at 300 K. The outflow from the nozzle is passed to the inflow of the reservoir. All additional boundaries of this region use characteristic

inflow / outflow conditions to hold the static pressure fixed at atmospheric pressure. These boundary conditions closely represent the experimental conditions and allow the discharge to develop in a physically consistent manner.

2.5.3. Results

Let us first consider the flow of the torch jet into the atmosphere without electrical energy addition. Figure 23 plots contours of velocity magnitude and density, overlaid with instantaneous streamlines. Clearly the jet is unstable, with the shear layer rolling up into vortices. This results in an unsteady flow field, with the vortical structures propagating downstream at approximately the shear layer mean convective speed. Simulations have been carried out to many characteristic times, and these structures persist in the calculations.

Previous results [6, 31] did not demonstrate this unsteadiness, but those calculations used a reservoir temperature of 800 K, rather than the 300 K used here. The new results have a three times larger reservoir density and have significantly lower viscosity in the shear layer. These differences greatly enhance the jet instability.

The flow field described by the Navier-Stokes equations assumes that the flow from the nozzle to the open atmosphere is laminar. The flow at the end of the nozzle section has a Reynolds number of about 10^4, suggesting that the flow in the nozzle is likely transitional or turbulent. The cold gas mixing upstream of the nozzle also enhances the turbulent motion in the nozzle. If this is the case, then the flow in the open jet must be transitional or turbulent as well.

With the background flow described above, we now include electrical energy addition. For computational reasons, we establish the discharge by propagating the electron flux from the cathode downstream to the anode before "igniting" the discharge. This provides an initial channel of electrons to carry the current. These electrons absorb the electrical energy, are boosted to high temperature, and rapidly produce more electrons until a balance between the energy addition and losses is established.

Once the discharge is ignited, it is difficult to obtain a steady state solution for the discharge. Figure 24 plots contours of vibrational temperature and electron number density 6.4 μs after the energy addition is started. Note the non-uniformity in the discharge, with substantial variations in n_e along the axis. In particular, the elevated region of n_e corresponds to the narrowing of the jet by the vortical structures. The discharge is not robust, and as the endless cycle of vortical motion occurs in the shear layer, the discharge is pinched and transforms into an arc.

The obvious question is: Why does arcing happen in the computations, but not in the experiments?

31
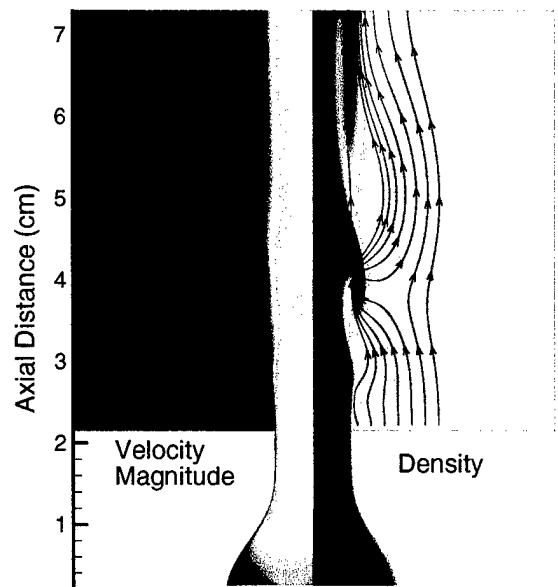
Figure 23. Contours of velocity magnitude and density at the experimental conditions without the discharge.
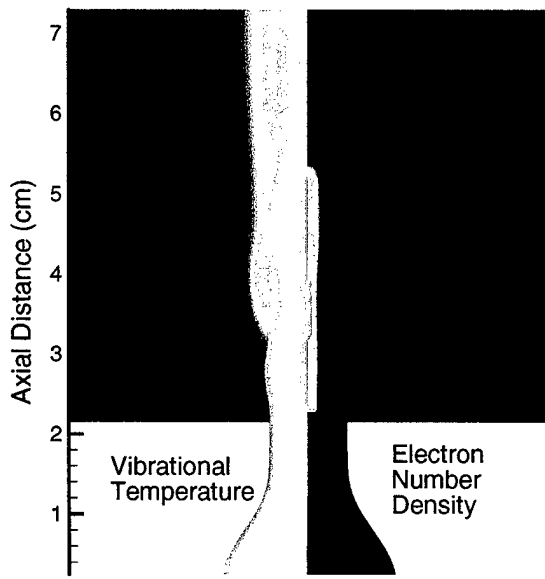
Figure 24. Contours of vibrational temperature and electron number density, 6.4 μs after discharge initiation.

One important mechanism to stabilize the discharge is radial heat conduction. If the flow is transitional or turbulent, the heat flux must have a component due to turbulent motion. There

is no adequate model for predicting turbulence in gas discharges or plasmas. Huang [32] introduced a two-fluid turbulence model for thermal plasma sprays that qualitatively reproduces the large-scale transport. He showed that pockets of heated gas move away from the shear layer, convectively transporting large amounts of heat. This mechanism would also inhibit the formation of large-scale vortical structures.

Unfortunately, without additional information about the properties of the experimental jet, it is very difficult to make *predictive* simulations for turbulent flows. We could include a turbulence model, but this would involve a tedious and unrewarding game of parameter adjustment (tuning) to get reasonable results. We have therefore resorted to an approximate approach to better understand the role of mixing in the discharge stability.

2.5.4. Approximate Discharge Model

The jet shown in Figure 23 and Figure 24 grows primarily by mixing across the shear layer. This mixing is slow, with the jet size remaining (at least visually) constant for the 3.5 cm length of the discharge. We can exploit this slow growth rate of the jet, and develop a simple and cost-effective jet/discharge model.

If we assume that the growth of the jet is simply due to diffusive processes (viscous dissipation, thermal conduction, and mass diffusion), then the flow gradients that drive these processes are negligible in the axial (x) direction. Then the above conservation equation becomes

$$\frac{\partial U}{\partial t} = W - \frac{1}{r}\frac{\partial rG}{\partial r},$$

and the two-dimensional steady-state equation is converted to a one-dimensional time-dependent problem that is *much* easier to solve. Within the limitations of our assumptions, this approach is useful to study the discharge growth mechanisms.

To implement this model, we start at the cathode plane where a known flux of electrons is imposed on the inflow velocity and temperature profile. We then integrate the above equation in time. Since the axial velocity u, varies only with r, we can construct the entire flow field by simply using $x = ut$.

Figure 25 plots contours of temperature and electron number density in the flow field computed with the approximate method at the experimental conditions. Note that because we have neglected streamwise gradients, there is no mechanism to promote an instability in the jet. However, if the calculation is run without the diffusive terms included, the discharge immediately collapses to an arc. The jet grows only very slowly because the thermal diffusivity is extremely low in the cold quiescent gas.

Figure 26 and Figure 27 show the centerline and radial variation of the discharge properties for this case. A close examination of the plot shows that the electron temperature

33

increases to very high values near the cathode (at $x = 0$) where the electrical energy is added to a small number of electrons. The high T_e causes the rapid production of electrons, which then lowers the electron temperature, and a balance between the electron density and temperature is reached. This figure shows that the heavy particle and vibrational temperatures do not increase significantly, but the coupling between these modes and the electrons is responsible for limiting the electron temperature. The electron temperature is approximately 10,000 K, which is somewhat lower than the 12,000 K found in the experiments. The vibrational and translational temperatures closely match the measured values. The predicted electron number density for most of the discharge is about 4×10^{11} cm^{-3}, which is considerably below the value of 2×10^{12} cm^{-3} measured in the experiments. The reason for this difference is unknown at the present time. Clearly, the electron number density depends on the details of the ionization and energy transfer rates.
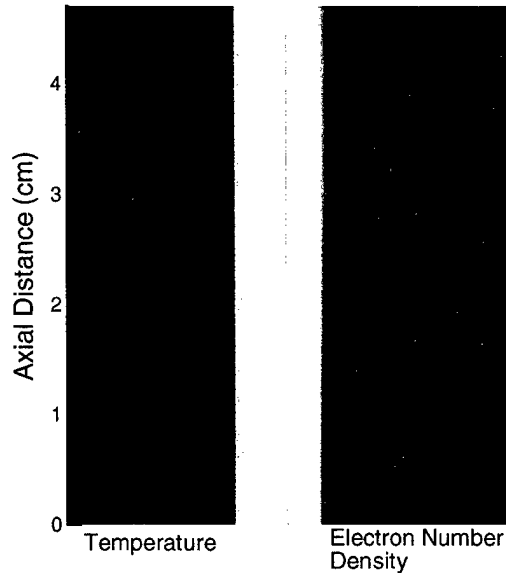
Figure 25. Contours of temperature and electron number density computed using the approximate method at experimental conditions.
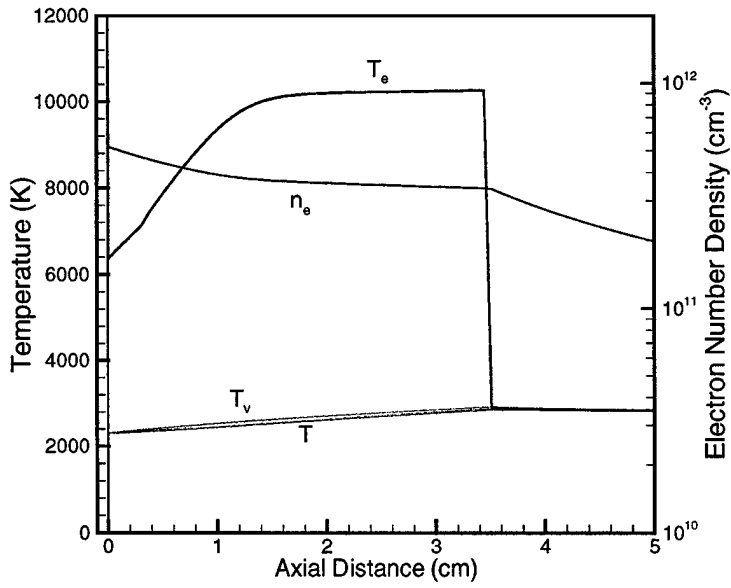
Figure 26. Centerline temperatures and electron number density computed using the approximate method at experimental conditions.
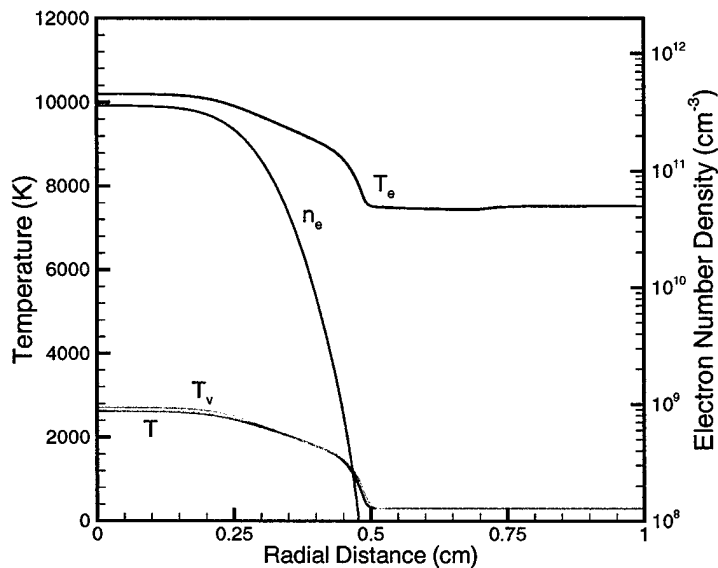
Figure 27. Cross-section of the computed discharge 2 cm from the cathode at experimental conditions.
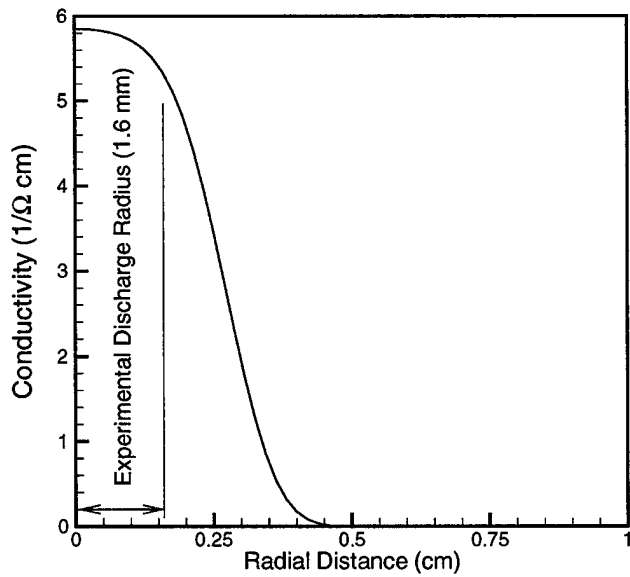
Figure 28. Electrical conductivity 2 cm from the cathode at experimental conditions.
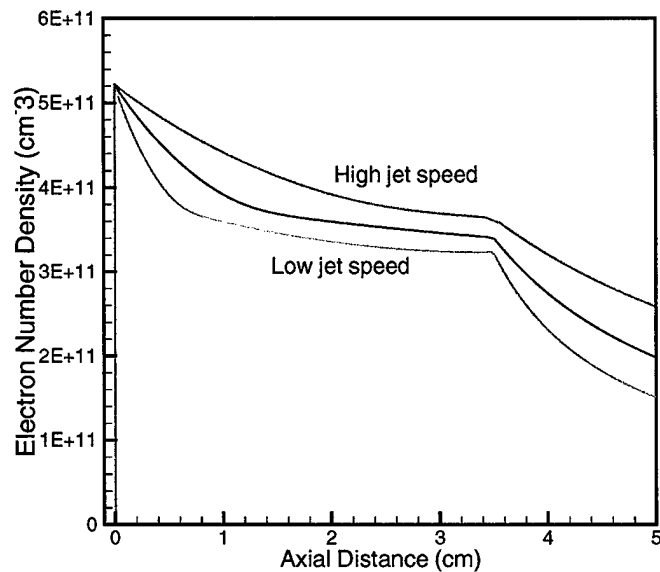
Figure 29. Variation of centerline electron number density with jet speed.
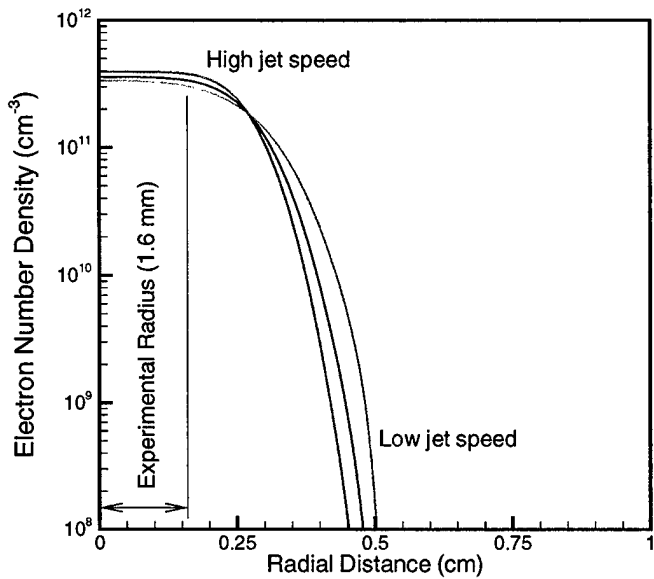
Figure 30. Radial variation of electron number density with jet speed 2 cm from the cathode.
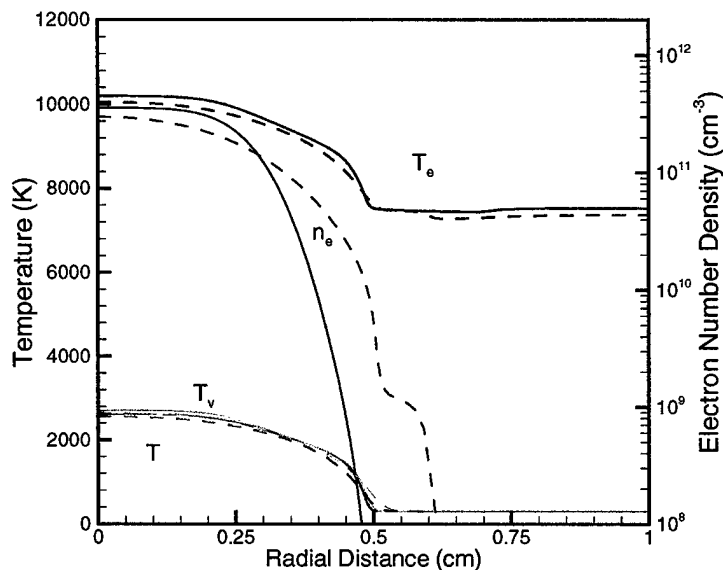
Figure 31. Radial variation of discharge properties. Solid lines: nominal transport properties; dashed lines: transport properties increased by a factor of 10.

The discharge diameter was measured to be approximately 3.2 mm. Figure 28 plots the electrical conductivity at a location 2 cm from the cathode. Although the edge of the discharge is not precisely defined, this plot shows that the computations produce a conducting channel of approximately the same dimension.

37

Figure 29 and Figure 30 summarize how the centerline and radial electron number density depend on the jet speed. Here, we have increased and decreased the jet speed by a factor of two from the measured 440 m/s. The higher jet speed reduces the rate of spreading of the jet, and therefore increases the centerline electron number density. However, this increase is minimal and is a result of the very slow mixing at the jet edge. The radial plot is consistent with the centerline results, showing an increased spreading at low jet speed. Again, the effect is small.

Based on the preceding arguments, we expect turbulent mixing to increase the spreading rate of the jet. We therefore performed additional simulations with the transport properties increased by a factor of 10 to mimic increased mixing. Figure 31 compares the radial variation of the temperatures and electron number density. The jet radius increases only minimally. Clearly, this simple approach of increasing the molecular transport properties does not produce substantial increased jet spreading. This is because turbulent mixing is a large-scale convective phenomenon. A more complete characterization of the jet is required to incorporate turbulent mixing into the model.

2.5.5. Conclusion

We have performed a computational analysis of the DC discharge experiments in preheated air. A complete axisymmetric simulation including an 11-species finite-rate air kinetics model and a three-temperature energy formulation was used. The jet simulations using this CFD model produced an unstable jet with large-scale vortical structures. Contrary to the experiments, the non-uniformities pinch the discharge and transition to an arc occurs. We postulate that turbulent mixing in the experiments stabilizes the jet.

To study the discharge spreading, we reformulated the model, freezing the gradients in the axial direction. This prevents formation of large vortical structures, and we obtain a stable diffuse discharge. The size of the computed electrically conducting channel matches the experiments, however the electron number densities are underpredicted. The electron temperature is similar to the experiment, and the vibrational and translational temperatures also agree well.

Using the approximate formulation, we varied the jet speed and transport properties to study how the jet spreads. We find that the very low thermal diffusivity in the cold external gas makes the jet spreading essentially insensitive to these changes. The lack of turbulent mixing in our model is a major limitation.

2.6. Transverse DC Discharges in Preheated Air Flow

In our previous research and the previous sections of this report, the electrical discharges were applied along the axis of the gas flow. We now describe experiments conducted in preheated air with a DC discharge perpendicular to the axis of the flow. Two flow-velocity conditions are investigated. We find that the slower flow "blows out" the discharge farther than the faster flow. To explain this counterintuitive result, we have made measurements of gas temperature and electric field profiles in the discharge, and we propose an explanation of the observed behavior based on the measured reduced field strength E/N in the discharge region.

2.6.1. Counterintuitive discharge behavior

The experiments presented here were conducted for two flow rate conditions, 32 and 110 slpm. The corresponding flow velocities are about 45 and 160 m/s. In both cases, the air flow was preheated to ~2000 K with the microwave plasma torch. The DC discharge is applied between two platinum pins orthogonal to the axis of the flow. The electric circuit is the same as for the single DC discharge experiments presented earlier (Figure 1).

Figure 32 shows photographs of the transverse discharges for the slow (Figure 32a) and fast (Figure 32b) flow conditions. In both cases the inlet gas temperature is approximately 2000 K, the interelectrode spacing 5 mm, the discharge current 100 mA. The voltage difference between the two electrodes is 1.2 and 1.33 kV for the gas flow rates of 32 and 110 slpm, respectively. The discharge volume is visually larger at the low flow rate condition. This observation may be somewhat paradoxical because one would expect the fast flow to blow the discharge farther downstream than the slow flow. Figure 33 shows the measured intensity profiles of N_2 C-B (0,0) emission along the centerline axis of the flow. These profiles confirm that the discharge extends farther downstream at low flow rate. They also show that the peak of N_2 emission is less intense in the slow flow than in the fast flow.

We anticipate that the observed emission profiles correlate with the reduced field strength profiles E/N. This is because the reduced field strength is the main parameter controlling the rate of electron-impact reactions. We obtained E/N from measurements of the electric field and gas temperature (from which we infer the gas density N) along the centerline axis of the flow.
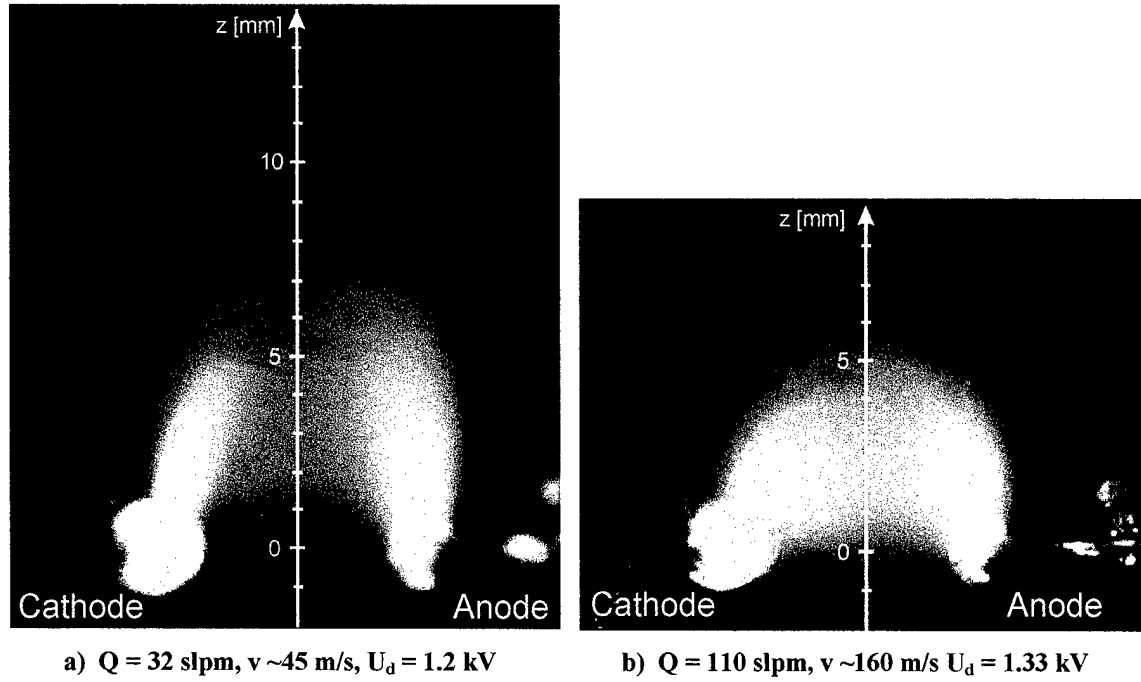
a) Q = 32 slpm, v ~45 m/s, U_d = 1.2 kV   b) Q = 110 slpm, v ~160 m/s U_d = 1.33 kV

Figure 32. Transverse DC discharge in preheated air flow. Flow direction: vertical upward. Interelectrode spacing: 5 mm, gas temperature: ~2000 K, discharge current: 100 mA.
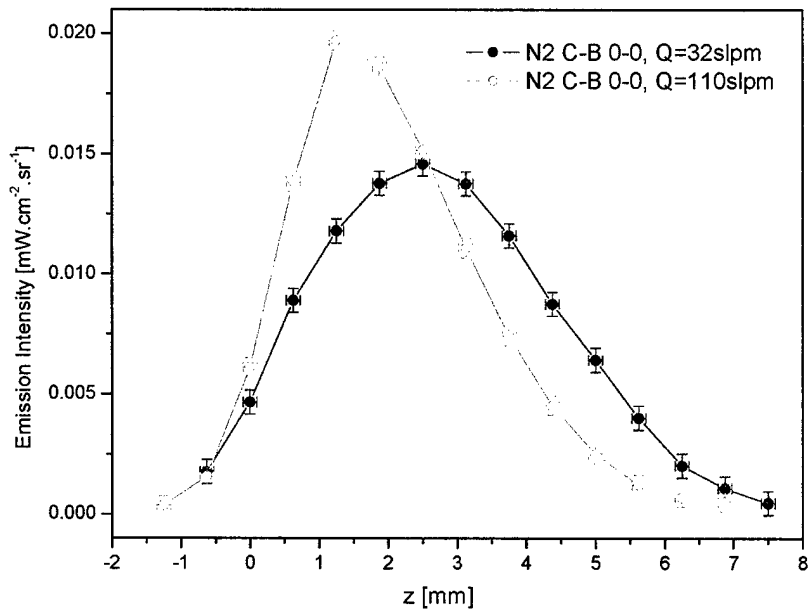
Figure 33. Emission intensity profiles of N_2 C-B (0,0) along vertical transverse discharge axis.

40

2.6.2. Electric field measurement

We measured the electric potential along the centerline z-axis of the flow with a high voltage probe connected to a platinum wire placed inside a ceramic tube (

Figure 34a). To determine the electric field strength from the measured floating potential, we make the following approximations:

- Since the discharge forms an arch, we assume that the current streamlines form arches as well. The length of an arch d is approximated by the length of the straight line between the cathode surface and the probe pin on the vertical axis, i.e. $d^2 = (2.5 \text{ mm})^2 + z^2$.

- We assume that the electric field is constant along a current streamline. This approximation only holds in the positive column and not in the cathode layer but the cathode layer is much thinner than the positive column.

With these approximations, the electric field is calculated as the measured floating potential of the probe minus the cathode potential fall, divided by the length d of the arch extending from the surface of the (grounded) cathode pin to the probe (

Figure 34b). For verification, we measured the E also by using a double-pin probe that measures the floating potential difference at a fixed spacing. Results obtained by this technique agree with the single probe measurements.

The electric field profiles measured for the two flow rate conditions are shown in Figure 35. Their shapes are similar, although in the low flow rate case the maximum E is shifted a little farther downstream and the E magnitude is about 30% smaller. This difference can be partly explained by noting that the voltage across the gap is smaller in the low flow rate case (1.2 kV vs. 1.33 kV). This reason is however insufficient to completely explain the differences in the field profiles.

a)   b)
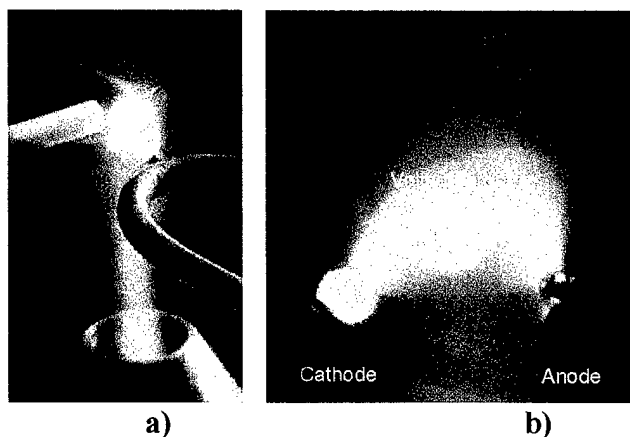
Figure 34 E-measurements along the centerline axis of the flow. a) Overview of the setup: microwave nozzle, preheated air flow, stainless-steel tubes with pin electrodes, discharge, and voltage probe. b) side view: pin electrodes, discharge, voltage probe, current streamline from the cathode to the probe.

41
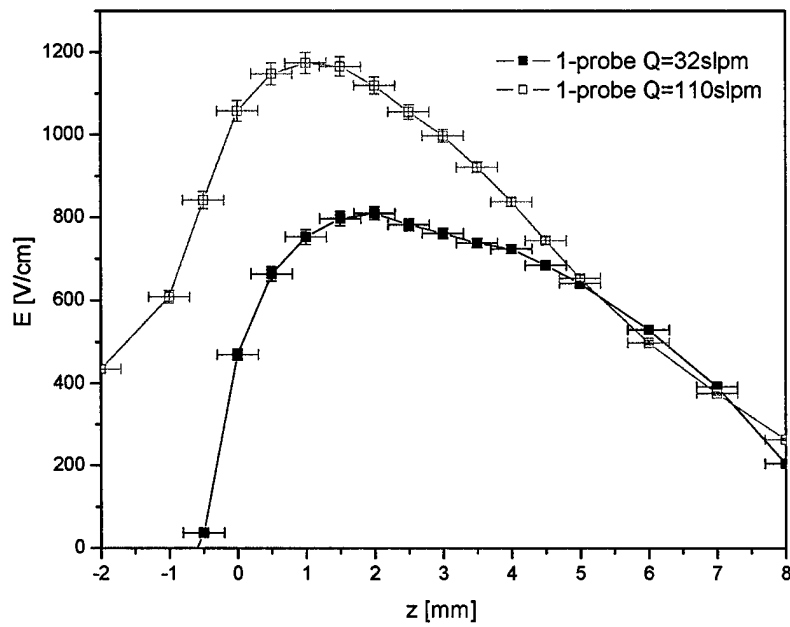
Figure 35. Measured electric field profiles in the transverse air discharges.

2.6.3. Gas density measurement
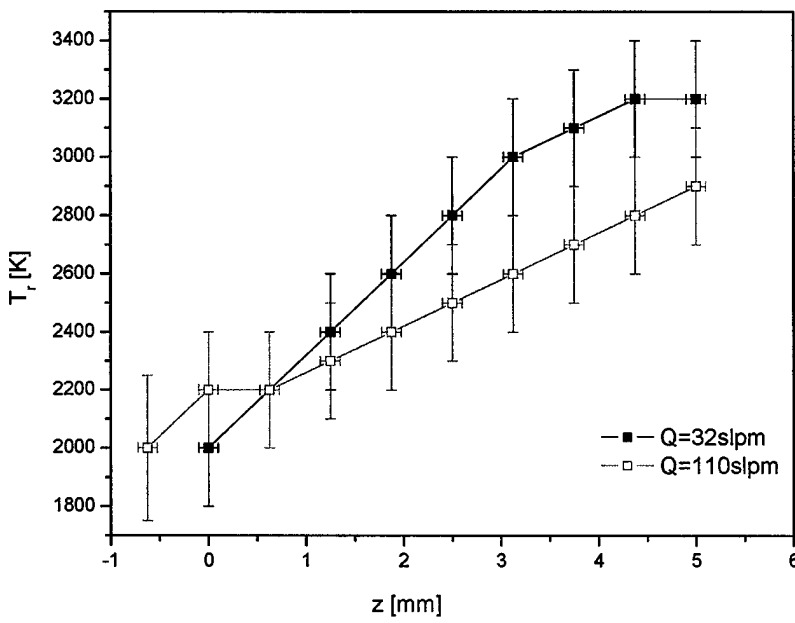
Figure 36. Rotational temperature profiles in the transverse air discharges.

42

We obtain the gas density profile from the gas temperature profile through the state equation $N = p/kT$. The gas temperature is assumed to be equal to the rotational temperature, measured from the shape of the bands of the N_2 C-B emission. The measured profiles, shown in Figure 36, indicate that the gas temperature increases more in the slow flow than in the fast flow, even though the total power dissipated in the discharge is a little higher in the fast flow case (133 W vs 120 W at slow flow). This effect can be again explained in terms of VT transfer (see section 3.2). In both cases, the discharge excites the vibrational modes of N_2 which then relax through collisions. This collisional quenching transfers energy from vibration into the translational modes of molecules, thereby heating the gas. There is more gas heating at low flow rate (i.e. low flow velocity) because the vibrational modes have more time to relax when the residence time is longer. This explains why the temperature increases more in the low flow rate case.

2.6.4. Reduced electric field strength

The reduced field strength E/N profiles deduced from the measured electric field and gas density profiles is shown in Figure 37. In Figure 38, we compare the E/N profiles with the optical emission profiles of the N_2 C-B (0,0) band from Figure 33. The E/N and emission profiles correlate well. It should be mentioned that small changes of E/N cause large changes of emission intensity.
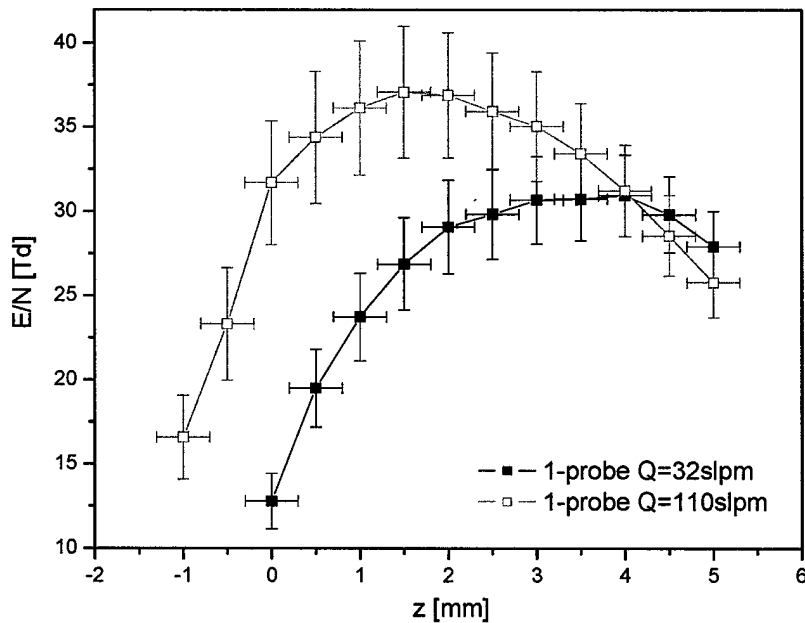
Figure 37. Measured reduced field strength (E/N) profile in the transverse air discharges.

43
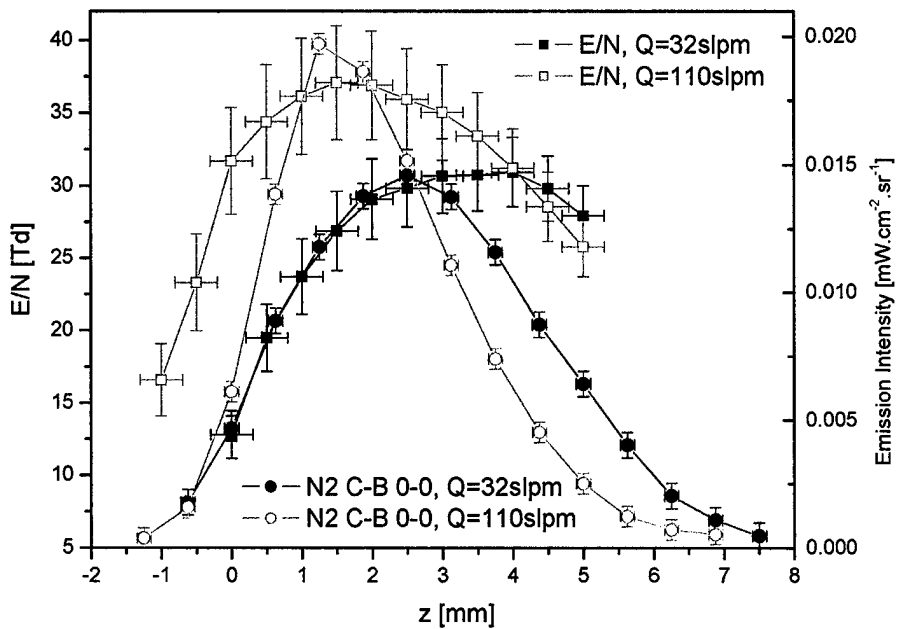
Figure 38. Comparison of E/N profiles and N₂ C-B (0,0) emission profiles in the transverse air discharges.

The results of the approximate measurements of the E/N confirm that the extent of the discharge correlates with the reduced field strength profile. The paradoxical wider extent of the discharge at low flow velocities appears to be mainly caused by a higher temperature downstream. Higher temperature results in lower gas density, thereby increasing the E/N farther downstream.

2.7. Dual DC Discharge Experiments

In this section, we consider the case of two DC discharges operated in parallel as a way to increase the volume of plasma. Section 2.7.1 describes the experimental setup, and Sections 2.7.2 and 2.7.3 present experimental results obtained with the dual discharges in ambient air and nitrogen. Some tests of triple DC discharges were also done.

2.7.1. Experimental Setup

The electrical circuit used to generate dual discharges in ambient (i.e. room temperature) air or nitrogen is shown in Figure 39. The discharges are obtained by applying a high voltage between a set of separately ballasted electrodes. The power supply is a 15 kW DC, Del High Voltage Model RHVS, capable of delivering a maximum voltage and current of 10 kV and 1.5 A. In the studies presented in this section, typical voltages and currents are in the range of 1-2 kV

44

and 100-200 mA. To stabilize the discharges, each cathode and anode is connected to the power supply through a 3 kΩ water-cooled Khantal – Globar ballast resistor.
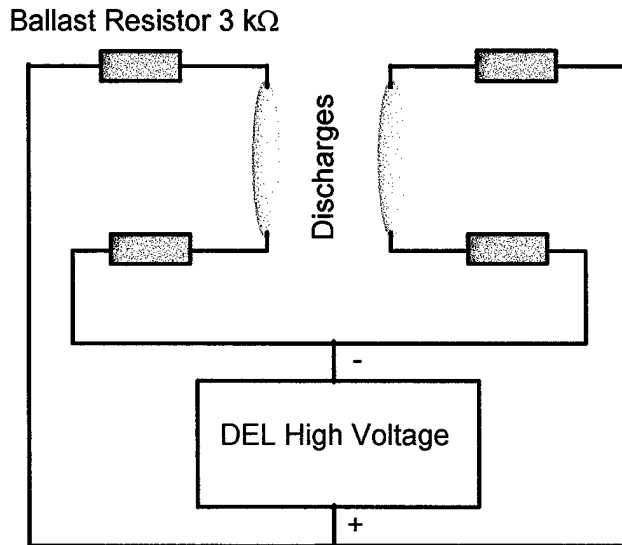
Figure 39. Electrical circuit used for dual-discharge experiments

Stainless steel tubes and platinum ball-pins are used as electrodes. Ambient air or nitrogen is injected with typical flow rates of 40 l/min (corresponding to a gas velocity of ~50 cm/s at room temperature) through a 7 cm diameter flow straightener, used to stabilize the incoming flow. 2D translation stages are used to vary the lateral distance between the two discharges.

2.7.2. Dual discharges in ambient air

The photographs presented in Figure 40 show the dual-discharge in ambient air as a function of the inter-discharge spacing. The ambient air and is injected into the discharge at a flow velocity of about 20 cm/s. The interelectrode distance is kept fixed at 1.2 cm, while the lateral distance l between the two discharges is varied from 1.35 to 0.85 cm. In all cases, the voltage and total current are 1.4 kV and 200 mA (~100 mA per single discharge).

For l = 1.35 cm, the two discharges are clearly separated. When the lateral distance is decreased to 1.15 cm, the space between the two discharges becomes gradually filled with a plasma "cloud". This luminous halo is due to the emission of the surrounding air environment heated by the discharge. Thus, as the lateral distance decreases, the temperature in the region between the two discharges increases due to heat transfer, leading to an increase of the size of the halo.

45

At lateral distances smaller than 1.05 cm, the two discharges merge into a single one, and the plasma volume is almost doubled. As the lateral distance is further decreased, the shape of the plasma remains the same.

Measurements of the emission intensity of the N_2 C-B (0,0) band head were also performed to determine the diameter of the central part of the discharge. For this purpose, an intensified CCD camera (Roper Scientific PI-MAX1024), coupled with a bandpass filter centered around the N_2 C-B (0,0) band head (337 nm) was used. Results are presented in Figure 41. The experimental conditions are the same as those reported on Figure 40. The measured FWHM of N_2 C-B (0,0) band head emission at mid-distance between the electrodes is approximately 1.3 mm when the two discharges are separated ($l \geq 1$ cm), and increases to 2 mm when the lateral distance $l = 0.8$ cm. Cathode layers with Faraday dark space are clearly visible in Figure 41 whereas they were hidden by the halo in Figure 40.

The effect of merging into one discharge column can be explained as follows. When the discharges become sufficiently close from one another, the volume of gas between the two discharges heats up. The gas density decreases, and therefore the reduced field strength E/N increases. The E/N increase may also occur partially due to a higher electric field in the discharge interspace. Since E/N is proportional to the electron temperature, the region between the discharges undergoes more intense ionization processes. Thus, a preferential channel develops in the space between the two discharges, thereby leading to the X-shape.
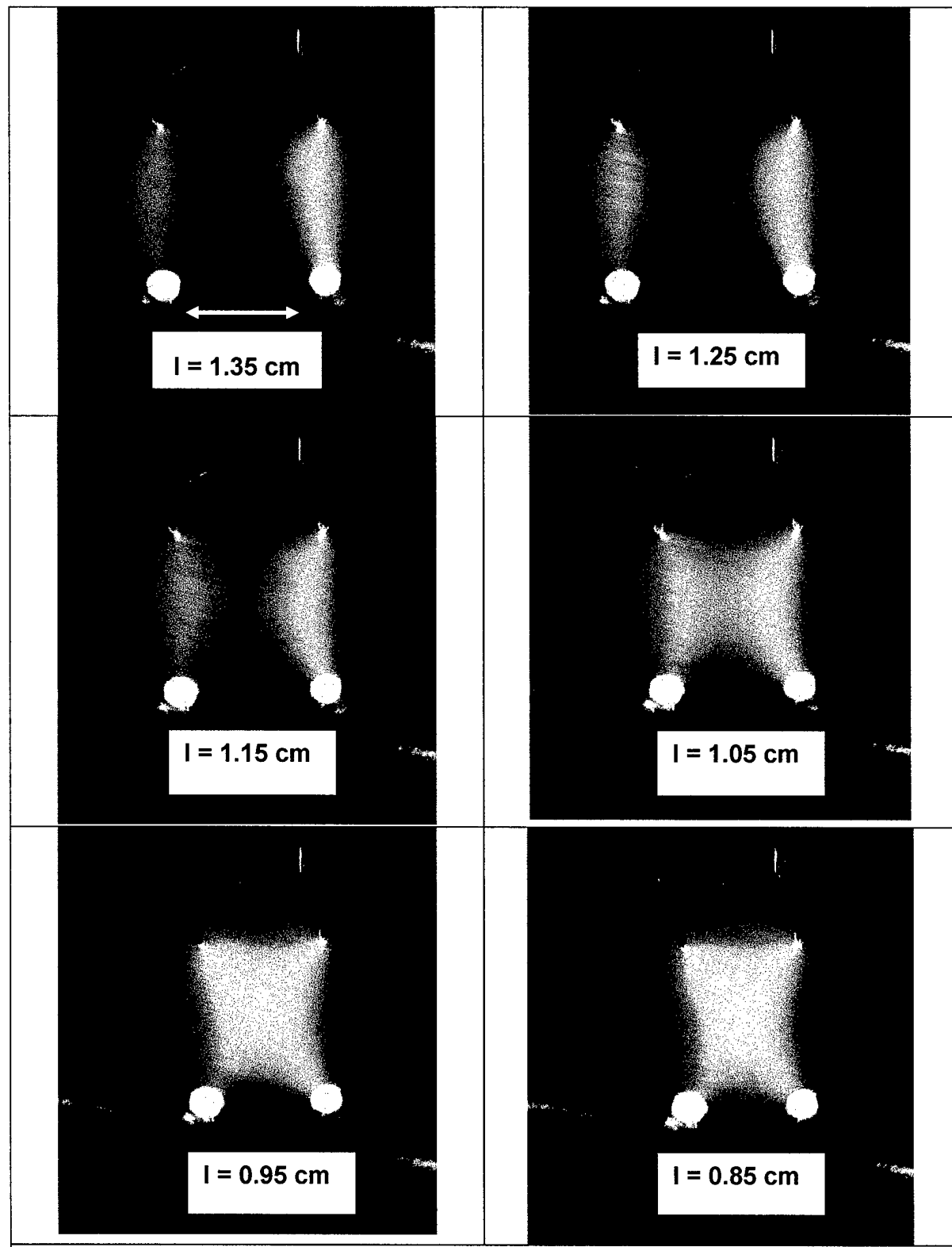
Figure 40. Dual-discharges in ambient air at atmospheric pressure for various separation distances. The gas velocity v ~ 50 cm/s, I = 100 mA per discharge, U = 1.4 kV.

47
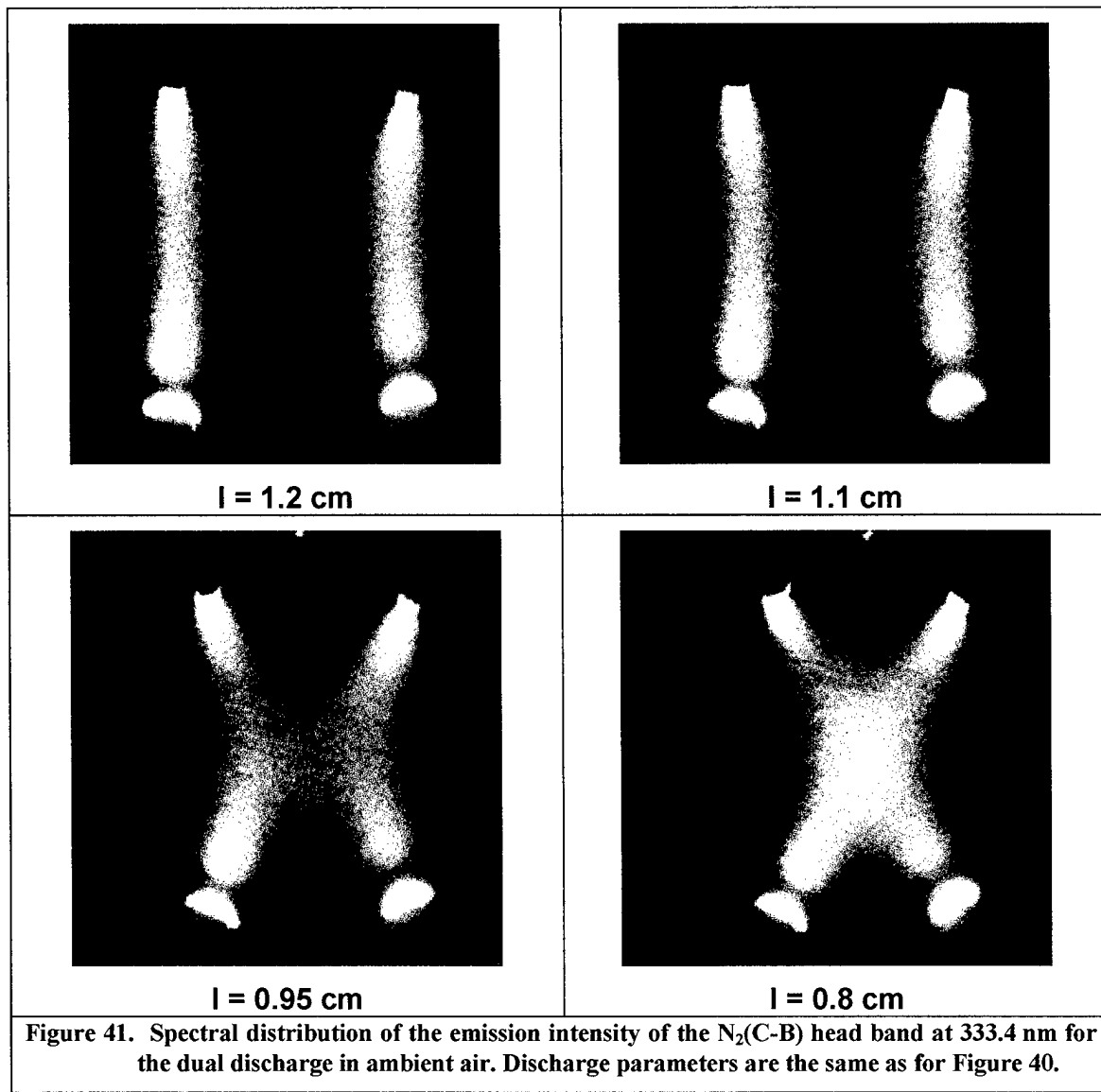
Figure 41. Spectral distribution of the emission intensity of the N_2(C-B) head band at 333.4 nm for the dual discharge in ambient air. Discharge parameters are the same as for Figure 40.

2.7.3. Dual discharges in ambient nitrogen

Dual-discharge experiments were also conducted with an ambient nitrogen at atmospheric pressure. Figure 42 shows the shape of the dual-discharge as a function of the lateral distance. The nitrogen gas velocity was fixed at about 50 cm/s, and the discharge current and voltage to 150 mA and 1.6 kV, respectively. Note the dark space near the cathode (bottom electrode) in the picture. At a lateral distance of 6 mm, the two discharges begin to merge into a single discharge. As the lateral distance is reduced, the space between the two discharges fills up with plasma, and, as in the case of air (Figure 41), an X-shaped dual-discharge is formed.

48
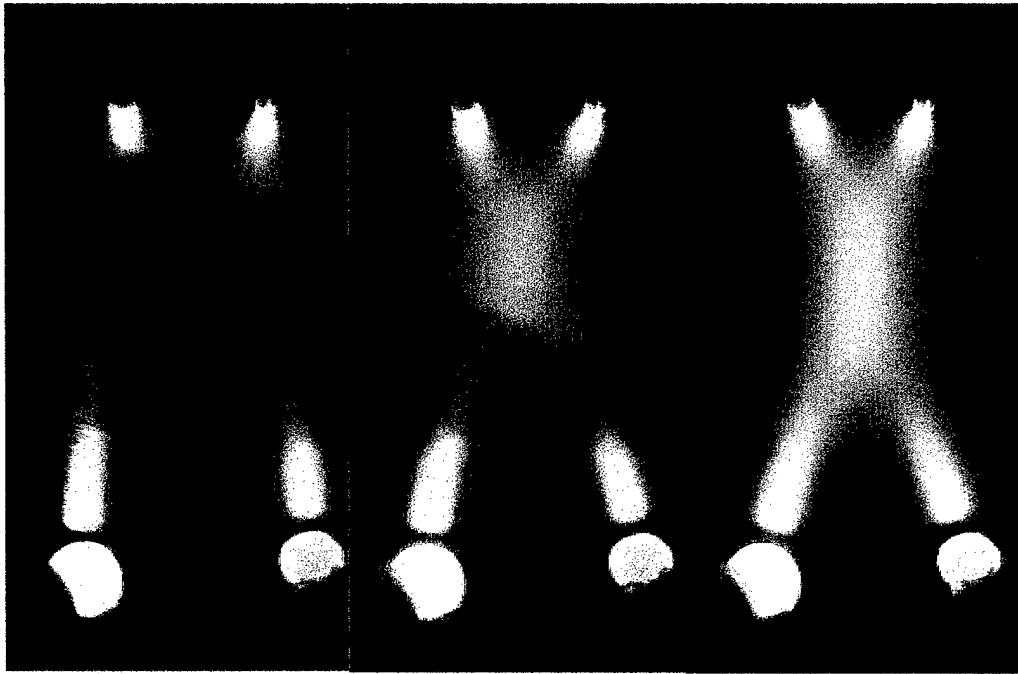
Figure 42. Dual-discharge experiments in ambient temperature nitrogen at atmospheric pressure. The gap is fixed at 1.2 cm and the lateral distance is varied from 0.6 mm to 0.4 mm (left to right). Gas velocity v ~50 cm/s, I = 150 mA, U = 1.6 kV.

This approach shows that the plasma volume can be increased up to ~1 cm^3 by the operation of dual or multiple DC discharges.

2.8. Scaled-up Repetitively Pulsed Discharge in Preheated Air

In the recent MURI program on "Air Plasma Ramparts" [1], we have demonstrated a novel method to efficiently produce electron densities of about 10^{12} cm^{-3} by means of repetitively pulsed discharges with short (10 ns) high voltage (10 kV) pulses. We have also shown that the power requirements are between two and three orders of magnitude lower than for DC discharges producing the same electron density. [8, 13] Additionally, these discharges produce no noticeable electrode erosion, and can be easily operated in parallel for scalability to large volumes.

Parallel operation with six sets of electrodes has been demonstrated in atmospheric pressure air preheated to about 2000 K. The experiment is shown in Figure 43. Preheated air flows at about 10 m/s from bottom to top. The parallel pulsed discharges are easier to implement than dual DC discharges because they do not require individual ballasting on each pin. The discharges do not appear to merge into a single column, unlike the case for the dual DC discharges. One possible reason is that the temperature of the air flow remains uniform. In the

49

pulsed discharges, Joule heating of the gas is very low because the overall discharge power is two to three orders of magnitude lower than in the DC discharges. Thus the gas density is approximately uniform in the entire volume of the multiple discharges, and the reduced field E/N, which controls ionization, is essentially a function of the E. As can be seen from Figure 43, we have achieved a discharge volume of about 0.5 cm^3. Scaling to larger volumes can be achieved by using additional pins.
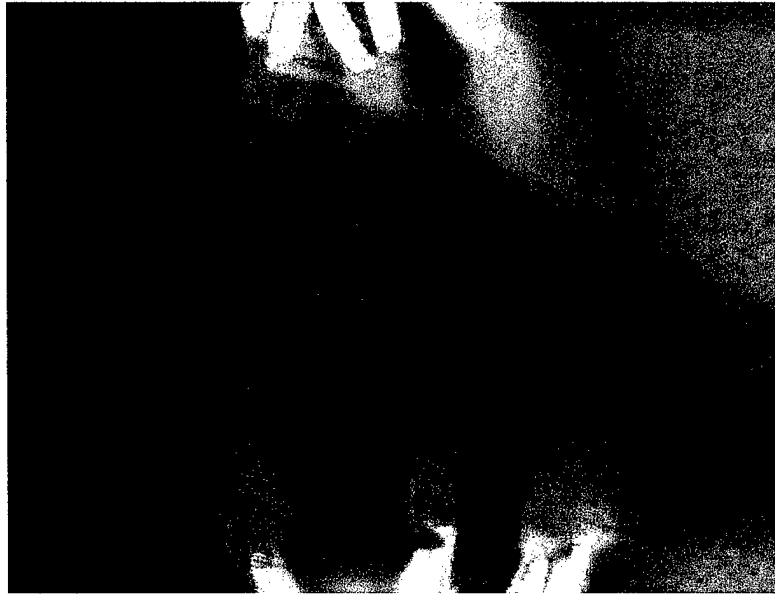
Figure 43. Multi-pin repetitively pulsed discharge in preheated air (~2000 K). Discharge volume ~0.5 cm^3. $n_e \sim 10^{12}$ cm^{-3}.

2.9. Dual-Discharge Experiments in fast preheated air flows

We have conducted experiments to combine two discharges operating in parallel in order to increase the plasma volume, and to investigate scaling effects. Dual discharges in slow ambient air or nitrogen flows have already been reported in Section 2.7. The two parallel discharges merged into a single column as they approached to each other. When the discharges become sufficiently close to each other the volume of gas between the two discharges heats up. The gas density decreases, and therefore the reduced field strength E/N increases. The E/N increase may also occur partially due to a higher electric field in the discharge interspace. Due to the enhanced E/N, the region between the discharges undergoes more intense ionization processes. Thus a preferential channel develops in the space between the two discharges, thereby leading to the X-shape.

50

2.9.1. Dual discharge experiment in parallel preheated air flow

The photographs presented in Figure 44 show a dual DC discharge in a flow of atmospheric pressure air preheated to $T \sim 2000$ K parallel to the discharge axis. The electrode configuration is the same as for dual discharges in ambient air (cathodes at the bottom, anodes at the top). Preheated air is injected into the discharge from the bottom at flow velocities from ~25 to ~160 m/s. The interelectrode distance is 1 cm, and the lateral distance between the two discharges is 0.5 cm. In all cases, the total current is 200 mA, with ~100 mA per single discharge. The voltage across the discharge gap varies from 1.22 kV at 25 m/s to 2.1 kV at 160 m/s.

The two discharges do not interact in the same way as in the slow flow of ambient air. In particular, the two columns have less of a tendency to merge into an X-shape discharge. The merging effect in ambient air occurs, as explained in Section 2.7, due to gas heating in the space between two discharge columns. This effect does not occur in the fast air flows because the residence time of the gas between the electrodes is too short for collisional relaxation of vibrationally excited N_2 molecules.
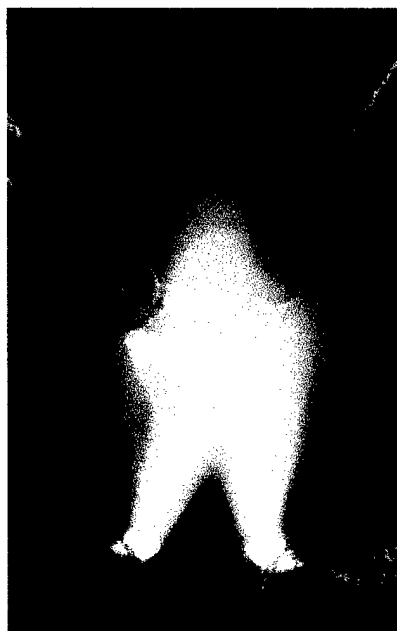
a) Q = 17 slpm, v ≈ 25 m/s, U_d = 1.22 kV   b) Q = 110 slpm, v ≈ 160 m/s, U_d = 2.1 kV

Figure 44. Dual discharge in air flow preheated to ~2000 K. Current 200 mA (total), interelectrode spacing 1 cm, lateral distance between discharges 0.5 cm.

One can notice the formation of a large luminous halo above the anodes on the vertical axis, especially in the 25 m/s flow. This halo is caused by emission from NO_2 in the air heated by the discharge, as already observed in discharges with ambient air. The discharges are less spatially and temporally homogeneous at high flow velocities, as can be seen in the high velocity

51

case (Figure 44b) where plasma filaments appear. However, filamentation occurs at the (cold) edges of the preheated flow, and is less likely to appear in a uniform preheated flow.

This approach shows that the plasma volume can be increased by the operation of dual or multiple DC discharges.

2.9.2. Dual discharge experiment in transverse preheated air flow

The results of experiments with transverse discharges (Section 2.6), together with the experiments with dual and multiple discharges described in above chapters, led us to conduct experiments with dual discharges in transverse flow of air preheated to ~2000 K. The photographs presented in Figure 45 show the discharge configuration (cathodes on the right, anodes on the left). The preheated air is injected into the discharge from the bottom perpendicularly to the discharge axis, at various gas flow rates (17-110 slpm) corresponding to flow velocities from ~25 to ~160 m/s. The interelectrode spacing is 0.5 cm, and the lateral (vertical) distance between the two discharges is 1 cm. In all cases, the total current is 200 mA, with ~100 mA per single discharge.
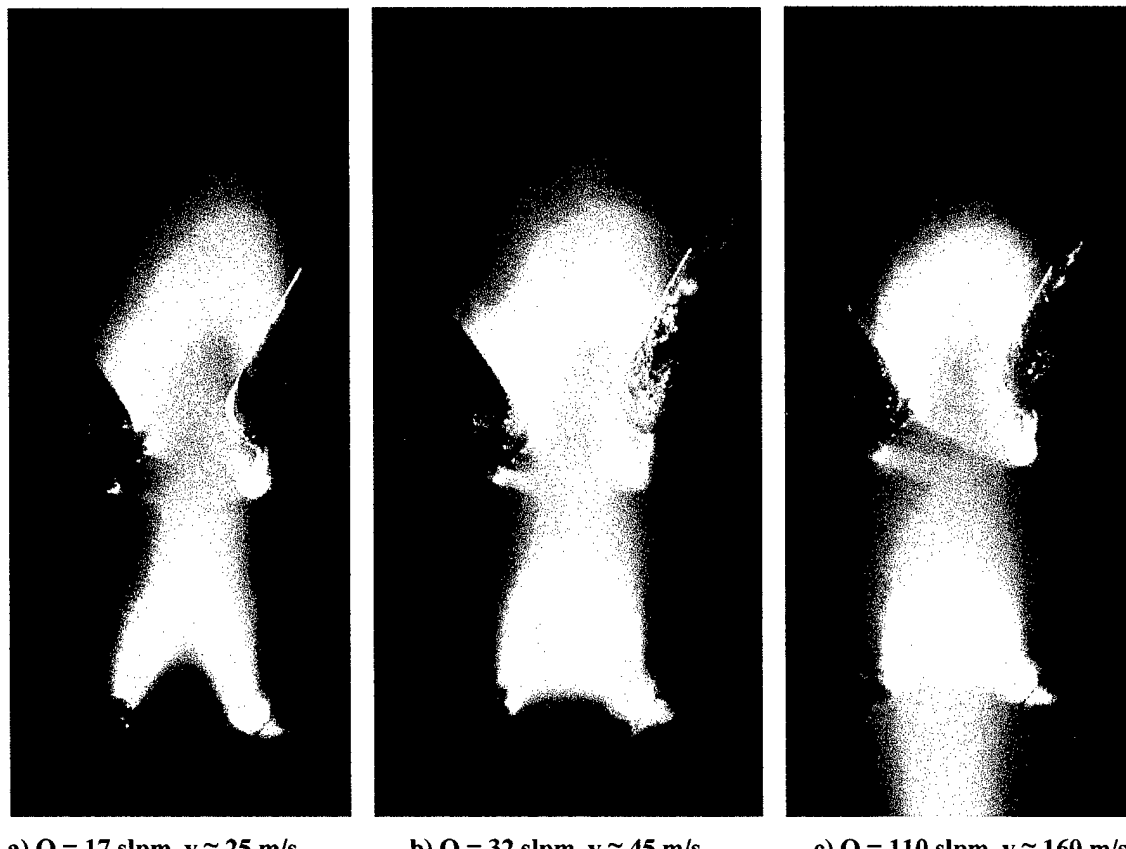
a) Q = 17 slpm, v ≈ 25 m/s   b) Q = 32 slpm, v ≈ 45 m/s   c) Q = 110 slpm, v ≈ 160 m/s

Figure 45. Dual discharge in transverse air flow preheated to ~2000 K. I = 200 mA (total), interelectrode spacing 0.5 cm, vertical distance between discharges 1 cm.

52

As can be seen from Figure 45, the lower discharge is very similar to a single discharge in transverse flow (Figure 32). On the other hand, the upper discharge looks different; the plasma spreads to the volume along the electrodes. The differences between the lower and upper discharges are due to different air flow properties and temperature patterns. The temperature and flow velocity tend to decrease along the vertical axis. On the other hand, the lower discharge dissipates a certain amount of energy into the flow. This effect is stronger at low flow velocities (~25 m/s) where the lower discharge almost reaches the upper discharge. The discharges look more diffuse and spatially homogeneous at low flow velocities, similar to dual discharges in parallel flow (Section 2.9.1).

Dual or multiple DC discharges in either parallel or transverse air flow represent possible ways to obtain larger volumes of atmospheric pressure air plasmas.

2.10. Experiments with thermionic cathodes and swirl flow injection

A *thermionic cathode* is a cathode made of a material that emits electrons by thermionic emission, i.e. electron emission induced by elevated temperature. In previously studied glow discharges with ordinary metal cathodes, the basic mechanisms of electron emission from the cathode are secondary processes such as positive ion impact. When a thermionic cathode is employed, electron emission from the cathode is enhanced by the thermionic effect, as a function of the cathode temperature.

We explored DC discharges at atmospheric pressure with or without thermionic cathodes at various experimental conditions:

- open air vs. in tubes of various diameters (4.7; 8.38; 10.45; 15.5; 22.1 mm)

- various discharge currents: 100-500 mA

- various interelectrode distance: 0.1-10 cm

- laminar vs. swirl flow injection of ambient air or N_2 at various flow rates (21-110 slpm)

- $LaCrO_3$, LaB_6 and Mo vs. stainless steel – Pt cathodes

All these cases were compared with each other. Such comparisons enable us to understand some basic mechanisms and properties of the discharges with thermionic cathodes and the role of the swirl flow fluid dynamics. However, the subject is still open for further investigations.

2.10.1. Discharge setup and cathodes

In experiments with thermionic cathodes, we replace the platinum cathode (in our previous experiments typically the lower stainless steel tube with Pt pin) with a small piece of thermionic material. We have tested lanthanum chromite ($LaCrO_3$), lanthanum hexaboride (LaB_6), and molybdenum (Mo) as thermionic cathode materials because their significant thermionic effect starts at relatively low temperature (~1400-2000 K). The thermionic cathodes are heated by the discharge itself, although we have made some attempts with external ohmic heating.

Mo is a hard metal; $LaCrO_3$ and LaB_6 are fragile, slightly conductive ceramics. All tested materials are difficult to weld, especially $LaCrO_3$ and LaB_6 that are challenging for electrical or mechanical contacts. In addition, we need these special cathodes in the middle of the gas flow but allowing the gas to flow around them approximately uniformly.

The best technical solution for Mo cathode seems to fix a 1-2 mm thin strip of Mo on top of the brass nozzle that provides the gas flow (nozzle exit diameter 1 cm). For $LaCrO_3$ and LaB_6 which cannot be easily made in the form of strip, we use the copper or stainless steel mesh that covers the nozzle exit. A small, usually irregular, piece (~1-2 mm) of $LaCrO_3$ or LaB_6 is fixed in the mesh in about the center of the gas flow. Figure 46 shows this setup without and with the glass tube regulating the gas flow.
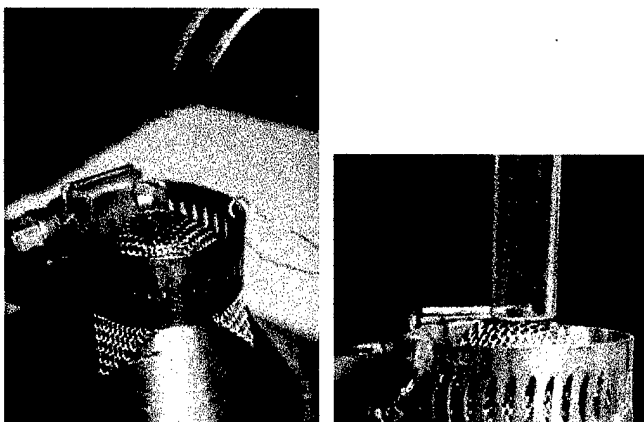
Figure 46. Set-up for experiments with $LaCrO_3$ cathode. A small piece of $LaCrO_3$ ceramic is fixed on the copper mesh covering the top of the gas feeding nozzle. The same set-up with a glass tube on the right.

Ceramic, glass and quartz tubes of various inner diameters (4.7; 8.38; 10.45; 15.5; 22.1 mm) and both swirl and axial gas injection into the discharge were examined to study their effects on the fluid dynamics of the plasma system. The swirling flow was established by tangential injection of the supply gas near the base of the microwave plasma torch in its off mode. In general, the tubes and the swirl flow help to stabilize the discharge spatially. Experiments in open air without the use of tubes were also conducted for comparison. Ceramic

tubes can resist higher plasma temperatures. On the other hand, glass and especially quartz tubes enable valuable direct emission spectroscopy of the discharge inside the tube.

The temperature of the thermionic cathode surface was measured by an infrared pyrometer Minolta Land Cyclops 152. We used the same set-up for the optical emission spectroscopy as for single DC discharges with regular cathodes (described in section 2.2, Figure 1).

2.10.2. Cathode fall reduction

Typically, glow discharges have a characteristic high-field cathode fall region where the voltage drops steeply by several hundreds of volts in a relatively short distance at the vicinity of the cathode. This region is only a few tens of μm in thickness at atmospheric pressure. The cathode fall in glow discharges is a function of the cathode material and the gas. [24]

However, when thermionic electron emission takes place, the cathode fall is reduced. With increasing temperature of the thermionic cathode, the thermionic emission starts to prevail over the secondary emission and there is no longer a need for the cathode fall. This is advantageous from the point of view of power budget since the overall discharge voltage is reduced.

We have measured the discharge voltage U as a function of the interelectrode distance d at various currents I, using $LaCrO_3$ thermionic cathode in atmospheric air discharges (Figure 47). For every specific current I, U depends on d linearly. The line slope, which gives the electric field strength E, decreases as I increases. The value where the line crosses the U-axis corresponds to the cathode fall, since the size of the cathode fall region is negligible when compared with the size of the positive column. One can observe that the cathode fall value decreases with the rising discharge current, unlike in glow discharges with non-thermionic cathode where it only depends on the cathode material and the gas. This is due to the thermionic emission that increases with increasing cathode temperature, hence increasing current. We found that at currents over 200 mA, the $LaCrO_3$ cathode temperature gets over ~1800 K and the cathode fall is eliminated. Consequently, the discharge operates at a lower voltage.
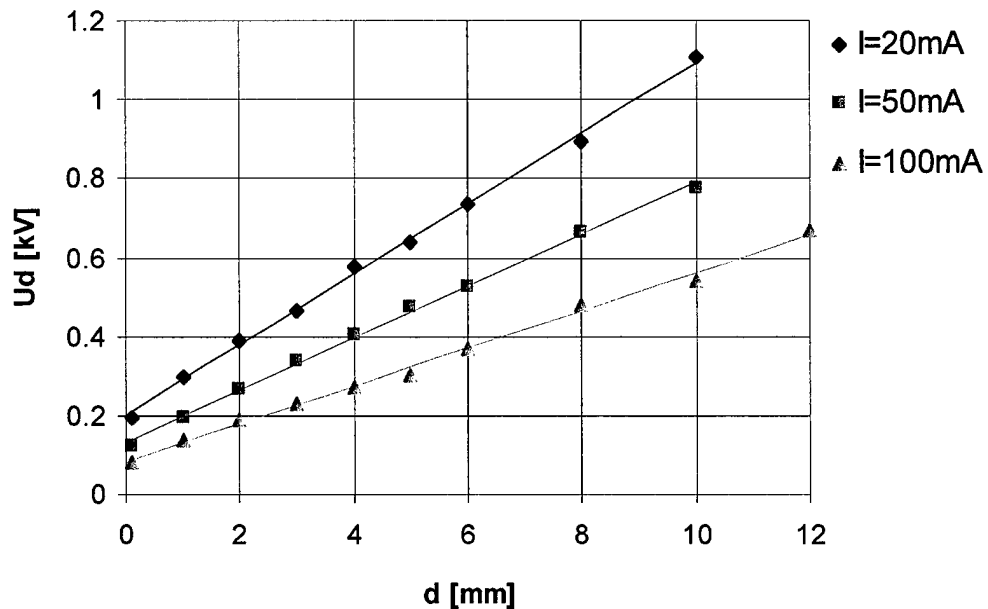
Figure 47. Discharge voltage U as a function of interelectrode distance d for various currents. Line slope gives the electric field, vertical offset on U-axis represents the cathode fall.

2.10.3. Discharges with LaCrO₃ and LaB₆ cathodes in open air

Figure 48a shows a 2 cm long DC discharge with a LaCrO₃ cathode in open air (without any tube) at swirl injection of ambient air with the flow rate $Q = 63$ slpm (standard liters per minute). Figure 48b shows a similar 2 cm long discharge with a LaB₆ cathode in open air at laminar injection with the same flow rate. For both cases the $I = 500$ mA. The $U = 447$ V or 420 V resulting in a relatively low electric field strength $E = 224$ V/cm or 210 V/cm, for LaCrO₃ and LaB₆ cathodes, respectively (cathode fall is close to 0 in both cases). Cathode temperature measured by the infrared pyrometer is found to be about 2100 K for LaCrO₃ and 1500 K for LaB₆, while anode temperature is about 1600 K in either case. The discharge diameter measured at the middle of the vertical axis by the emission intensity profiles of molecular bands of N₂ (B-A) and atomic lines of Cr and O is found to be around 3 mm for both cases, for LaB₆ also measured from BO emission. By making a simplified calculation assuming a constant current density distribution across the whole discharge diameter, we get $j = 7$ A/cm² for both cases. The power density $P = jE$ is relatively low (about 1.5 kW/cm³). The gas temperature in the middle of the discharge channel measured as rotational temperature of the molecular bands of N₂ (B-A) system is $T_g \approx 3000$ K. The estimated electron number density n_e in both discharges is high, approximately 3×10^{13} cm⁻³, and is one order of magnitude higher than a typical value obtained in DC discharges with Pt cathodes.

56
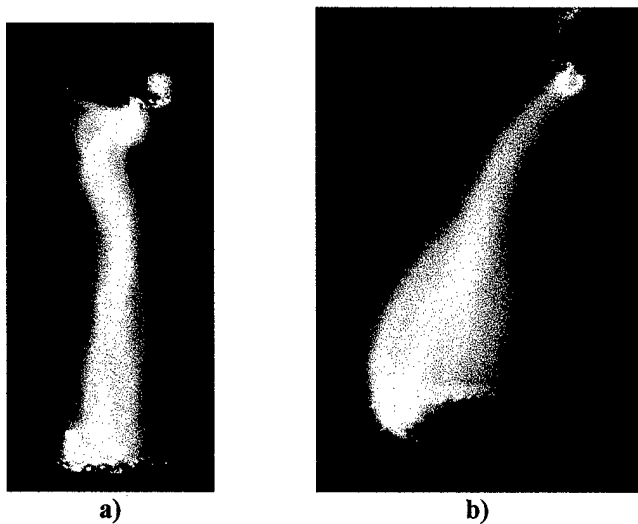
Figure 48. Discharges in open air with a) LaCrO₃, b) LaB₆ cathode. Interelectrode distance 2 cm, air flow rate 63 slpm, I = 500 mA, U = a) 447 V, b) 420 V, discharge diameter 3.1 mm.

The discharge diameter is slightly increased when the current I is increased, though not enough to keep j constant, so j increases with the increasing I. On the other hand, the electric field E decreases with increasing I in such a manner that the resulting power density $P = jE$ does not increase. This seems to be a reason why discharges with thermionic cathodes often have lower power requirements (per number of electrons created) than those with regular metal cathode: a lower E is needed to sustain the discharge.

2.10.4. Effect of tubes and swirl gas injection

Discharges in open air tend not to be spatially and temporally uniform (Figure 48). This makes their spectroscopic diagnostics, as well as measuring their precise diameter and consequently current density, difficult. In order to stabilize the discharges we surrounded them by glass (quartz, ceramic) tubes and injected a swirl air (nitrogen) flow. Tubes with various inner diameters have been tested ($\Phi = $ '4.7; 8.38; 10.45; 15.5; 22.1 mm). They were put directly on top of the gas-supplying nozzle with 1 cm diameter exit.

Tubes with a large diameter ($\Phi = 22.1$ mm) do not seem to have much effect on the discharge stability and straightness. On the other hand, tubes with medium and small diameters ($\Phi = 15.5$; 10.45; 8.38 mm) combined with the swirl flow injection affect the discharge considerably. The discharge spatial and temporal uniformity is improved. Furthermore, the discharge can undergo higher gas flow rates of ambient air or nitrogen without extinguishing. Another effect is that the discharge is more confined in the middle of the tube, its diameter D is reduced when compared with open-air case. Because of the reduced D, the current density j is increased, and consequently, n_e and P are increased as well.

57

a)   **b)**
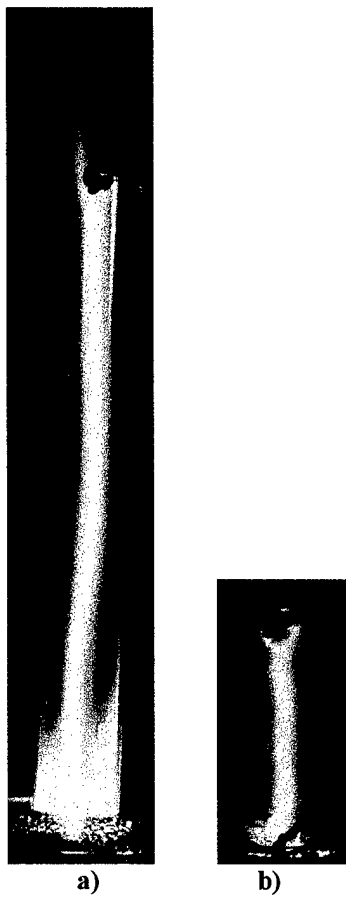
Figure 49. Air discharges with LaCrO₃ cathode in glass tubes and swirl flow, Q = 110 slpm.   **a)**
tube diameter 8.38 mm, I = 500 mA, d = 6.5 cm, U = 1037 V, discharge diameter D = 1.8 mm.
b) tube diameter 10.5 mm, I = 200 mA d = 1.8 cm, U = 825 V, D = 1.4 mm.

Figure 49 shows the 6.5 and 1.8 cm long discharges in ambient air swirl flow with the flow rate $Q = 110$ slpm with tubes of 8.38 and 10.5 mm inner diameter. Their parameters are, respectively: $I = 500$ and 200 mA, $E = 160$ and 458 V/cm, $D = 1.8$ and 1.4 mm, $j = 20$ and 13 A/cm², $n_e \approx 10^{14}$ and 3×10^{13} cm⁻³. Both discharges have $T_g \approx 3000$ K.

Tubes with the smallest tested diameter ($\Phi = 4.7$ mm), in which the gas flow velocity is the highest, confine the discharge to the greatest extent. However, their use is technically limited because the hot cathode spot easily touches the glass/quartz tube wall and melts it.

We also studied the effect of the tube diameter on the discharge properties in nitrogen swirl flow. The same behavior was observed, namely the tubes improve the discharge stability, enable them to operate at higher flow rates, and cause confinement of the discharge channel resulting in increased j, P, and n_e. The smaller the tube diameter and the higher the gas flow rate, the smaller discharge diameter is measured. Figure 50 shows the discharges in ambient swirl injected nitrogen in glass tubes with following characteristics, respectively: $d = 6$ and 3.8 cm; $I = 200$ and 500 mA; $\Phi = 10.45$ and 22.1 mm; $Q = 110$ and 94 slpm; $E = 365$ and 231 V/cm. The

58

discharge in the glass tube with small diameter (Figure 50a) is straighter, narrower and more stable, we were able to reliably measure its diameter and other parameters: $D = 1.6$ mm; $j = 10$ A/cm^2; $n_e \approx 3\times10^{13}$ cm^{-3}; $P = 3.6$ kW/cm^3. On the other hand, the discharge in the large diameter tube (Figure 50b) is broader and less uniform, with filaments; we were not able to measure its diameter reliably.

a)   b)
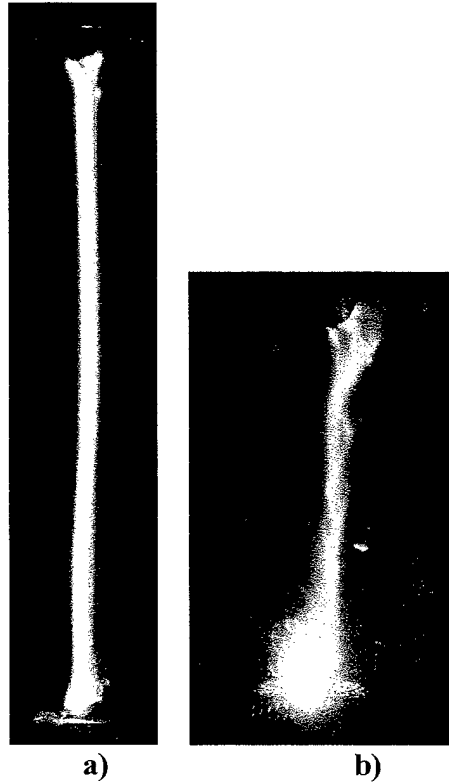
Figure 50. Nitrogen discharges with LaCrO$_3$ cathode in glass tubes and swirl flow, Q = 110 slpm.

a) Interelectrode distance d = 6 cm, tube diameter 10.45 mm, , I = 200 mA, U = 2144 V, discharge diameter D = 1.6 mm.

b) d = 3.8 cm, tube diameter 22.1 mm, I = 500 mA, U = 877 V, D = 2.9 mm.

We also explored the effect of the swirl gas injection in comparison with axial gas injection. Discharges with axial gas injection are much more sensitive to the gas flow rate. They are stable only at lower gas flow rates (max. $Q = 21$ slpm for $I = 200$ mA). They also have larger column diameters than their counterparts in swirling gas because they are not confined. The discharge diameter in axial flow does not depend on the tube diameter; the tubes have no effect on the discharge properties.

These observations indicate that the swirl gas injection, especially in narrow tubes at high gas flow rates, is responsible for unique fluid dynamic properties in the tube. Such flow properties stabilize the discharge in the middle of the tube because

59

it can more easily heat the gas by the VT transfer mechanism described in Section 2.2.3. In addition, the pressure is probably slightly reduced in the core of the tube. Therefore, the reduced field in the middle of the tube must be higher, thus stabilizing the discharge in this central zone.

Note that the gaps of 6.5 cm in Figure 49 or 6 cm in Figure 50 are very long, and we easily operated 10 cm or even longer discharges in tubes with swirl gas flow. Such long discharges were not possible to obtain without using the stabilizing effect of the swirl flow and the tube. Operating in this configuration is therefore interesting from the point of view of plasma volume scaling.

2.10.5. Discharges with Mo cathode and swirl flow

Discharges with a Mo thermionic cathode are similar to those with $LaCrO_3$ cathode. According to Raizer and Dobretsov [24, 33], Mo is a less satisfactory thermionic material than La-based compounds, in a sense that the thermionic emission starts to occur at higher cathode temperature. However, we have achieved thermionic emission from Mo cathode in air DC discharges in glass tubes. An example of such a discharge is shown in Figure 51. The 3.1 cm long discharge of $I = 500$ mA and $U = 781$ V is operated in the glass tube with 10.45 mm inner diameter. The ambient air is swirl-injected at $Q = 110$ slpm. Measured discharge diameter in the mid-distance between the electrodes is only $D = 1.3$ mm which results in very high $j = 38$ A/cm^2 and $n_e \sim 10^{14}$cm^{-3}. It is uncertain if the cathode fall at these conditions is close to 0 or rather to its normal value with Mo non-thermionic cathode (cathode temperature ~1500 K). This brings an uncertainty to the measured value of electric field $E = 207 \pm 45$ V/cm. Discharge temperature measured spectroscopically was found to be 2750 ± 250 K.
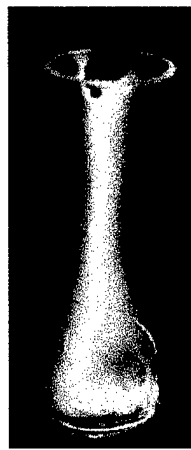
Figure 51. Air discharge with Mo cathode in 10.45 mm thick glass tube, interelectrode distance 3.1 cm, Q = 110 slpm, I = 500 mA, U = 781 V, discharge diameter 1.3 mm.

One can observe from Figure 51 that the discharge originates at the side of the Mo cathode strip, close to the glass tube wall. Then it slides almost horizontally along the surface of the Mo cathode and finally gets its vertical direction toward the anode. It is also obvious that the

discharge is not uniformly thick, D and j values provided in the above paragraph correspond to the middle of vertical axis where the discharge is the thinnest.

2.10.6. Discharges with ordinary metal cathodes in swirl flow

After obtaining interesting results of experiments with thermionic cathodes combined with the swirl flow injection the question arose: Is it mostly the effect of the thermionic cathode or rather the effect of the swirl flow in the tubes? In order to separate the two effects we performed some experiments with the discharges with ordinary metal cathodes (stainless steel) but using the swirl flow and the tubes.

a)   b)
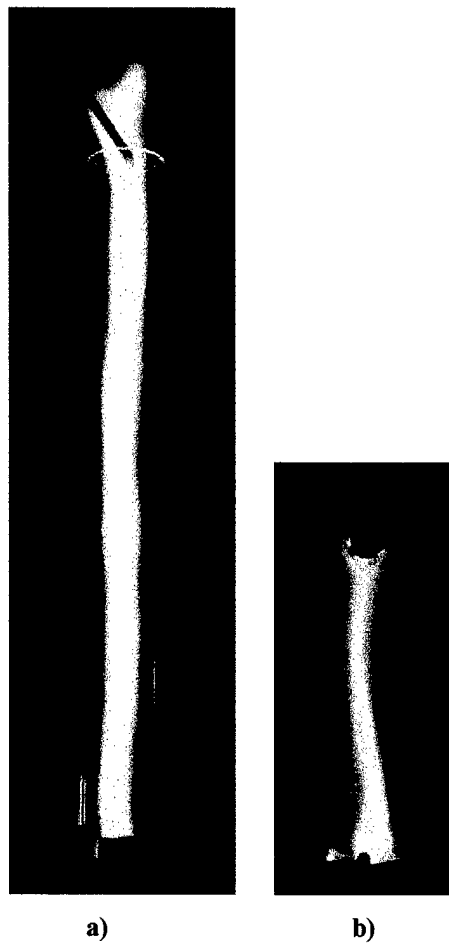
Figure 52. Air discharges with stainless steel cathode in quartz tube and swirl flow, Q = 110 slpm, tube diameter 10 mm. Different exposures. a) I = 150 mA, d = 10.3 cm, U = 3983 V, discharge diameter D = 1.55 mm. b) I = 500 mA, d = 3.2 cm, U = 1003 V, D = 2.35 mm.

Interestingly, we found that stable long discharges could be obtained in swirl flow in tubes even with non-thermionic cathodes. Figure 52 shows two examples of such discharges in

the swirl flow of the $Q = 110$ slpm and in the 10 mm thick quartz tube. They have the following characteristics, respectively: $d = 10.3$ and 3.2 cm; $I = 150$ and 500 mA; $E = 365$ and 230 V/cm; $D = 1.55$ and 2.35 mm; $j = 8$ and 11.5 A/cm^2; $n_e \approx 1.9 \times 10^{13}$ and 4.2×10^{13} cm^{-3}; $P = 2.9$ and 2.6 kW/cm^3. However, the gas temperature measured in these cases is high: ~3500-3700 K. Note that the discharge is more than 10 cm long in Figure 52a. Despite its length, it is very stable, and if the available tubes and the high voltage generator did not technically limit us, we could operate such discharge at even longer gaps.

We must underscore that the temperature of the stainless steel cathode in these discharges was probably high, especially in the 500 mA discharge where Fe and Cr were evaporated from the cathode, detected in the emission spectrum, and condensed on the tube walls. We could not measure the cathode surface temperature pyrometrically because there was no unique cathode spot, the discharge wandered around the cathode surface.

2.10.7. Spectra of discharges with thermionic cathodes

We have always been using the optical emission spectroscopy as a powerful technique for diagnostics of gas discharges. If we compare the emission spectra of air and nitrogen discharges with thermionic cathodes with previously studied discharges with ordinary metal cathodes (Pt, stainless steel, Cu), we find several general differences.

Open-air discharges with Pt, stainless steel or Cu cathodes typically used to exhibit N$_2$ 2nd (C-B) and 1st (B-A) positive systems, NO γ system and OH A-X bands, their relative intensities depended on the discharge parameters. The 2nd positive system of N$_2$ is the most convenient for determination of rotational and vibrational temperatures, as well as for measurements of the discharge diameter from the emission intensity profiles. Unfortunately, this system was found to be very weak or absent in most of the air discharges with thermionic cathodes, as well as in the discharge with stainless steel cathode but with the swirl flow. This is probably due to the low electric field, which is not high enough for electron-impact excitation of the N$_2$ C$^3\Pi_u$ state (11 eV). The absolute value of the emission intensity of N$_2$ 2nd positive system normalized to the discharge diameter as a function of the E/N is shown in Figure 53. The emission intensity increases approximately exponentially with the E/N.

The N$_2$ 1st positive system normally appears in the VIS-NIR spectrum. The electric field is probably still sufficient to excite the N$_2$ B$^3\Pi_g$ state by the electron impact (7.4 eV). An example of a UV spectrum of a 500 mA discharge with LaCrO$_3$ cathode compared with 5 mA discharge with Cu cathode is shown in Figure 54.
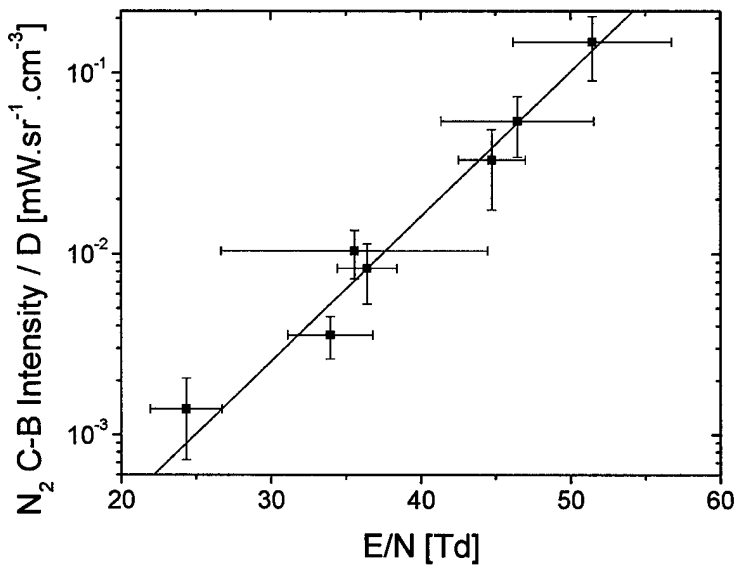
Figure 53. Absolute emission intensity of N_2 (C-B) normalized to discharge diameter D as a function of E/N.
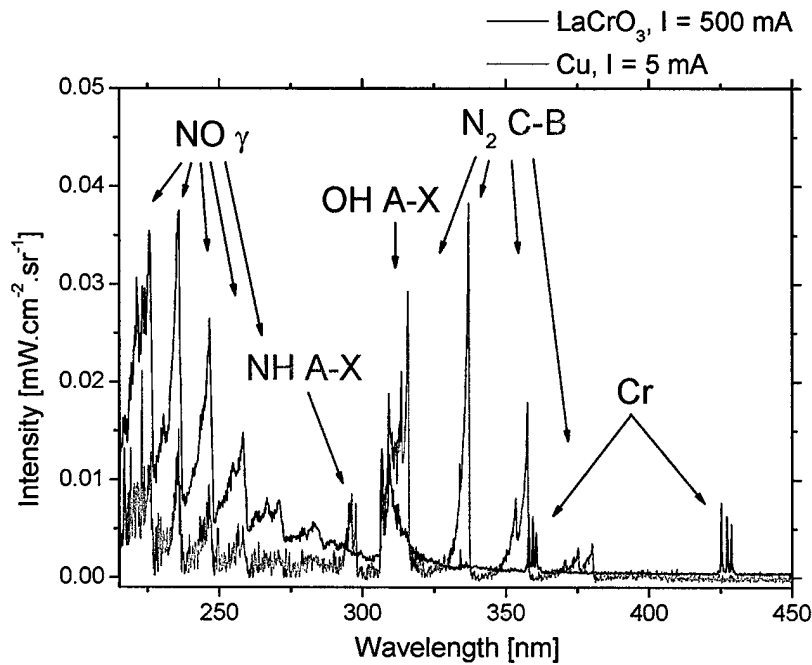
Figure 54. UV emission spectrum of air discharge with $LaCrO_3$ cathode compared with air discharge with Cu cathode and I = 5 mA. $LaCrO_3$ discharge properties are the same as in Figure 49b.

The NO γ and OH A-X bands at wavelengths below 320 nm are present in the UV spectra of discharges with thermionic cathodes in open air and with recently used quartz tubes. These bands provide an opportunity to measure the rotational temperature and the discharge diameter. However, in our fist set of experiments with thermionic cathodes and glass tubes, these could not

be used because they were filtered by glass. Therefore, we developed a novel technique of using N_2 1st positive for temperature measurement since in many cases this was the only distinguished molecular system. Yet, this system is very complex, especially in nonequilibrium plasmas where nonequilibrium vibrational distributions change relative intensities of their particular bands. It is not generally used for temperature measurements. Furthermore, the high wavelength tail of VIS-NIR spectra increased by the wall reflections of a very intense continuum radiation from the thermionic cathode. The complexity of the spectrum of an air discharge with $LaCrO_3$ cathode is illustrated on the sample VIS-NIR spectrum in Figure 55.

We have chosen a part of the 1st positive N_2 system spectrum between 875-884 nm which corresponds to transitions between vibrational levels close to each other and still has reasonable intensity to be distinguished from the cathode continuum radiation. We have assumed that these transitions are not too much affected by vibrational nonequilibrium and that the slope can be used for determination of rotational temperature after careful zero adjustments and normalization. The reliability of this technique was verified by different non-thermionic cathode discharges with distinct N_2 2nd positive spectra. The best obtained accuracy of this technique applied to thermionic cathode discharges was ±250 K. In many cases where the signal-to-noise ratio was low, we were only able to measure within ±500 K, or unable to measure at all.

Later we upgraded glass tubes with quartz tubes, enabling us to detect UV molecular systems such as NO γ and OH A-X for temperature measurements. This also provided further verification of the technique based on N_2 1st positive system for the T_g measurement.
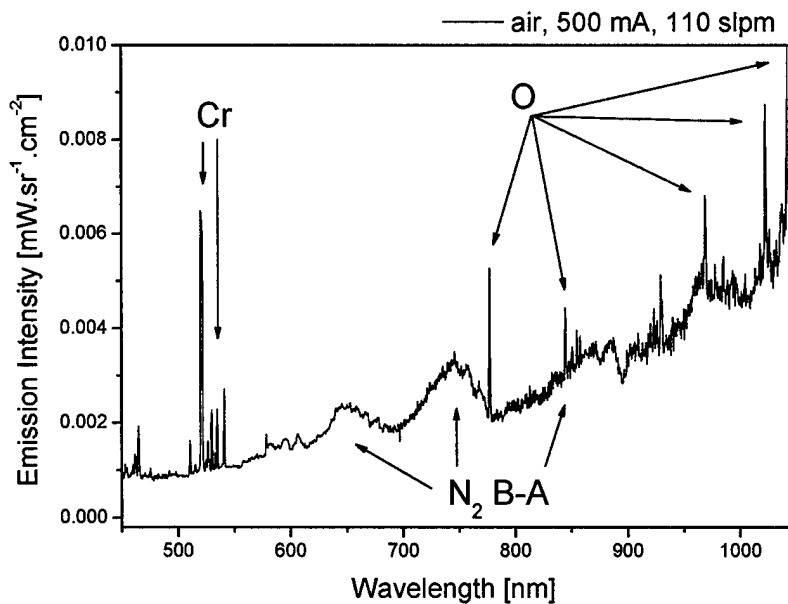
Figure 55. VIS-NIR emission spectrum of air discharge with $LaCrO_3$ cathode. Discharge properties are the same as in Figure 49b.

Strong atomic Cr or Mo lines appear in the spectra of the discharges with LaCrO₃ and Mo cathodes, respectively, as well as O lines. In the discharges with LaB₆ cathodes, we detected a new molecular system in VIS region that we assigned to BO (boron monoxide), Figure 56. In general, the lack of N_2 2nd positive system and perturbing atomic or molecular lines make the spectroscopic diagnostics of these discharges difficult.
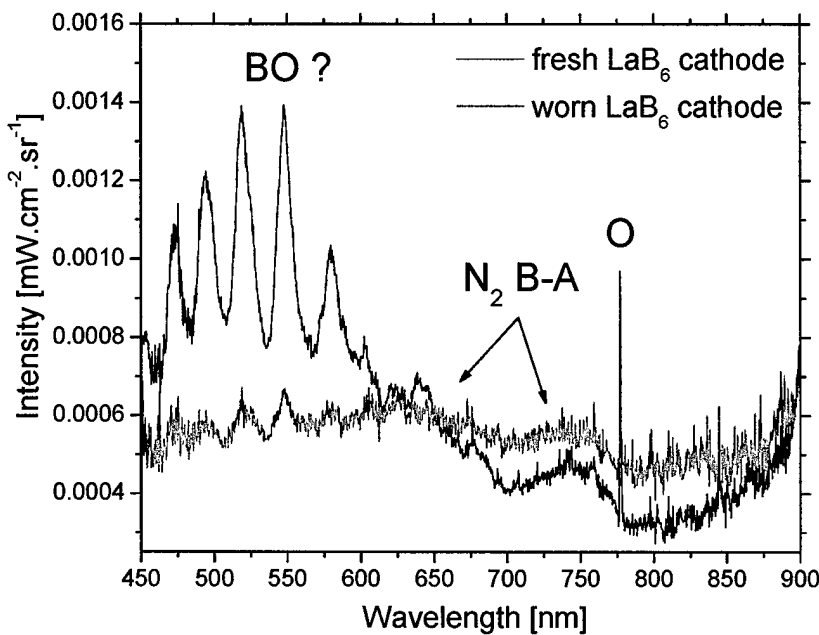
Figure 56   VIS-NIR emission spectrum of air discharge with LaB₆ cathode, fresh vs. worn cathode. I = 100 mA.

On the other hand, atomic Cr, Mo, and O lines that perturb molecular spectra and make the temperature measurement challenging, provide a useful tool for discharge diameter measurements. The presence of Cr and Mo lines in the air spectra with LaCrO₃ and Mo thermionic cathodes, as well as the presence of BO with LaB₆ cathode, indicate the removal of the material from the cathode into the plasma. This effect was confirmed by two other observations: deposits on the glass tube walls and reduction of the cathode material size up to its complete disappearance after a certain time of operation. The surface structure of the cathode material apparently changes during the operation, especially at Mo cathodes that become covered by the white-yellowish layer of Mo oxide (most likely MoO₃). LaB₆ cathodes, although generally considered one of the best thermionic materials, do not seem to be very convenient for our strongly oxidizing hot air conditions. They only operate for few minutes and quickly degrade, releasing BO to the gas and leaving white amorphous-like deposit on the cathode. Figure 56 also shows the different magnitudes of the BO emission intensity when the cathode is fresh and when it is already used for few minutes. Out of the materials we tested, LaCrO₃ seems to be the most convenient thermionic material for atmospheric air discharges, capable of functioning for several hours without substantial degradation.

The nitrogen discharges with LaCrO$_3$ cathode provide completely different spectra. First, there are no atomic Cr or O lines present. Apparently, chromium is neither sputtered nor evaporated as in the air discharges. This is probably due to chemically inert N$_2$ gas, whereas oxidation of LaCrO$_3$, as well as LaB$_6$ and Mo occur in air. Second, N$_2$ 1st positive system is much more intense than in air discharges. It is thus easier to use it for diagnostic purposes. And third, a strong N$_2^+$ 1st negative system appears in the UV spectrum. Its emission indicates a high degree of ionization, hence high n_e. An example of such a spectrum in the UV is shown in Figure 57.
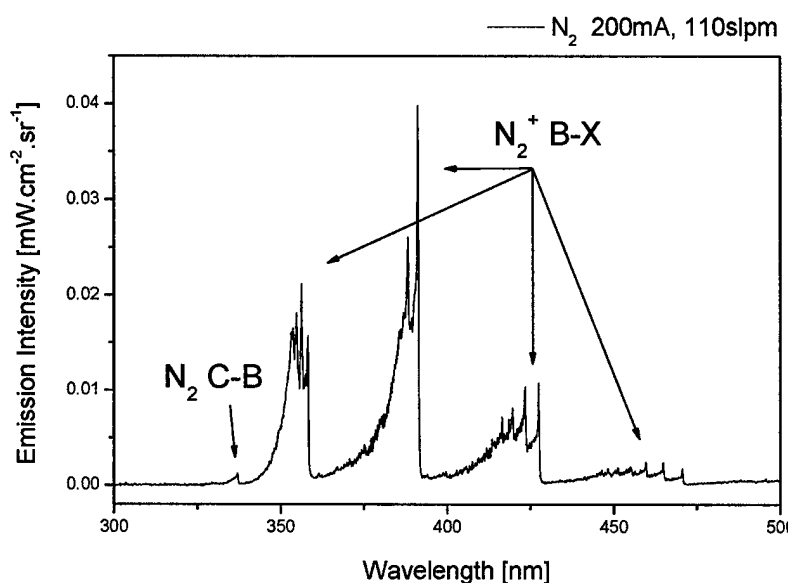
Figure 57. UV-VIS emission spectrum of N$_2$ discharge with LaCrO$_3$ cathode. Discharge properties are the same as in Figure 50a.

2.10.8. General *E-j* and *E/N-j* characteristics of air discharges

General voltage-current characteristics of DC atmospheric air discharges represented in terms of electric field – current density (*E-j*) have been reported previously. [1, 9-11] Experimental points on an *E-j* graph were shown together with predictions of collisional-radiative modeling of nonequilibrium air plasmas, also developed in our research group. [16-17] The previous *E-j* characteristic is shown in Figure 19, section 2.4.1. Now we put new experimental data together with previous data onto these characteristics and summarize the results. The reduced field – current density (*E/N-j*) representation is more appropriate because it accounts for temperature variations in various experiments. The gas temperature in most of the experiments with swirl flow was around 3000 K.

The new experimental data referring to discharges with thermionic cathodes and discharges in swirl flow fall in the lower right portion of the *E-j* and *E/N-j* graphs in Figure 58

66

and Figure 59. These discharges operate at lower E (E/N) and higher j than the previously explored discharges with Pt or Cu cathodes, in preheated air. The new data reveal a falling trend of the tail of E-j and E/N-j curves. Decreasing E/N is associated with decreasing emission intensity of N_2 (C-B), as shown in Figure 53. If we assume that the N_2 C state is mainly populated by direct electron impact, i.e. its population is proportional to T_e, and mainly depopulated by radiation to the N_2 B state, this result may then indicate decreasing T_e with increasing n_e. It would be consistent with our previously reported S-shaped behavior of the T_e-n_e curve. [1, 9-11] However, other depopulation mechanisms of N_2 C may take place and possibly overwhelm N_2 C-B radiation. Quenching by O atoms may be such a mechanism since the concentration of O atoms is likely to be considerably high at high n_e. Further analysis is required to associate the falling trend of E/N-j curve with the T_e-n_e curve and draw reliable conclusions.

In discharges with thermionic cathodes and swirl flow, we observe a significant enhancement of the electron density, the estimated n_e of these discharges is $\sim 10^{13}$-10^{14} cm^{-3}, i.e. 1-2 orders of magnitude higher than the previously obtained n_e in the discharges with metal cathodes and in open air. At the same time, power requirements related to the electron density are lower.

Variation of experimental conditions (with or without tubes, various tube diameters, swirl vs. laminar flow, cathode materials, etc.) causes a relatively large scatter of these data, especially in terms of j. However, some common features can be found:

- For a fixed E and E/N, j is greater in the experiments with tubes and swirl flow (full points in Figure 58 and Figure 59) than in open air experiments, regardless to the cathode material. This is caused by the previously discussed confinement of the discharge due to the swirl flow.

- For a given j, E and E/N are lower in the experiments with thermionic cathodes (blue and violet points in Figure 58 and Figure 59) than in the experiments with metal cathodes, regardless to the flow conditions. We find here the low E and E/N even when the cathode fall was subtracted when we calculated the E and E/N in experiments with metal cathodes (cathode fall is reduced with thermionic cathodes, as discussed in section 2.10.2).

At present, we do not fully understand the separate roles of the thermionic effect and the swirl flow. It seems that the swirl flow effect is more important in terms of high n_e (due to discharge confinement) and of the discharge stability, hence volume scaling. Nevertheless, the combined effect of the thermionic cathode and the swirl flow results not only in high n_e and favorable discharge stability, but also in low power requirements related to the electron density.

E- j characteristics of air discharges

Legend:
—·— Chauveau, model 1800K
—·— Chauveau, model 2300K
—·— Chauveau, model 2500K
—·— Chauveau, model 2900K
○ Yu, exp. 1800K
○ Yu, exp. 2300K
○ Yu, exp. 2500K
○ Yu, exp. 2900K
◇ Pt preheated air ~2800K
✳ Cu HPGD 1650-1950K
✳ Cu HPGD 2200K
□ LaCrO3, LaB6 open ~3000K
■ LaCrO3 15.5mm tube ~3000K
■ LaCrO3 10mm tube ~3000K
▲ Mo 10.5mm tube ~2750K
▼ LaB6 10mm tube ~3200K
◇ Fe open ~3700K
◆ Fe 10mm tube ~3500K
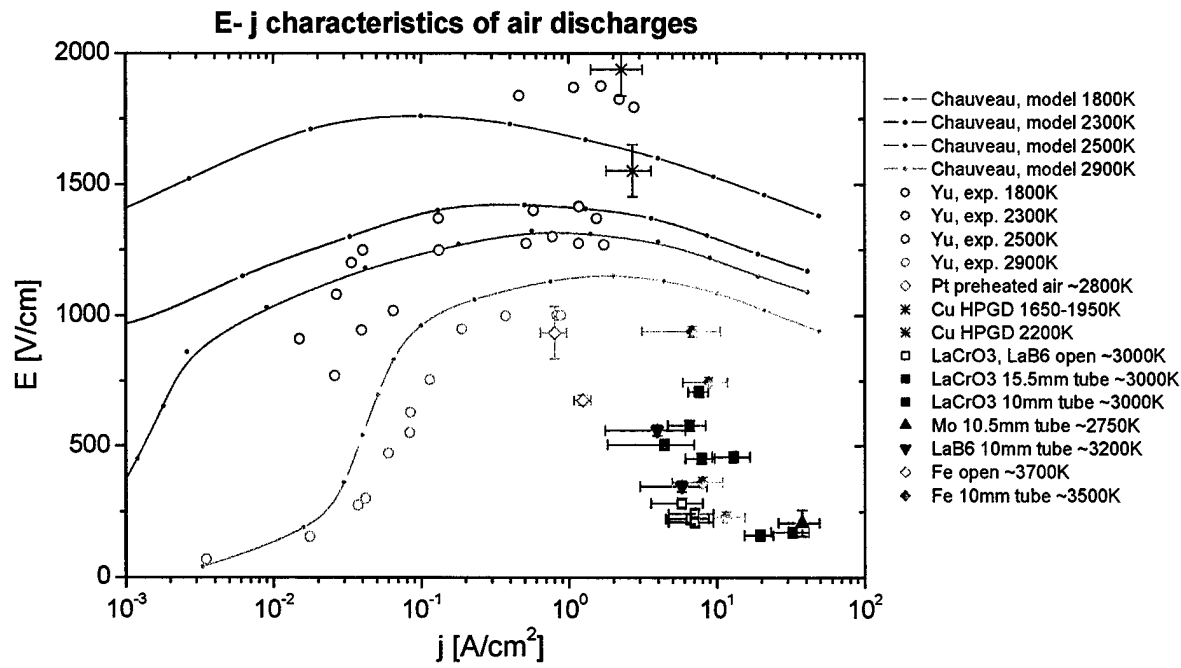
Figure 58. E-j characteristics of air discharges. Solid lines: collisional-radiative modeling by Chauveau [16]; experimental data designated Yu: discharges in preheated air with Pt cathodes [9-10]. Open symbols: experiments in open abmient air; full symbols: experiments in tubes with swirl flow of ambient air.

E/N- j characteristics of air discharges

Legend:
—·— Chauveau, model 1800K
—·— Chauveau, model 2300K
—·— Chauveau, model 2500K
—·— Chauveau, model 2900K
○ Yu, exp. 1800K
○ Yu, exp. 2300K
○ Yu, exp. 2500K
○ Yu, exp. 2900K
◇ Pt preheated air ~2800K
✳ Cu HPGD 1650-1950K
✳ Cu HPGD 2200K
□ LaCrO3, LaB6 open ~3000K
■ LaCrO3 10mm tube ~3000K
■ LaCrO3 15.5mm tube ~3000K
▲ Mo 10.5mm tube ~2750K
▼ LaB6 10mm tube ~3200K
◇ Fe open ~3700K
◆ Fe 10mm tube ~3500K
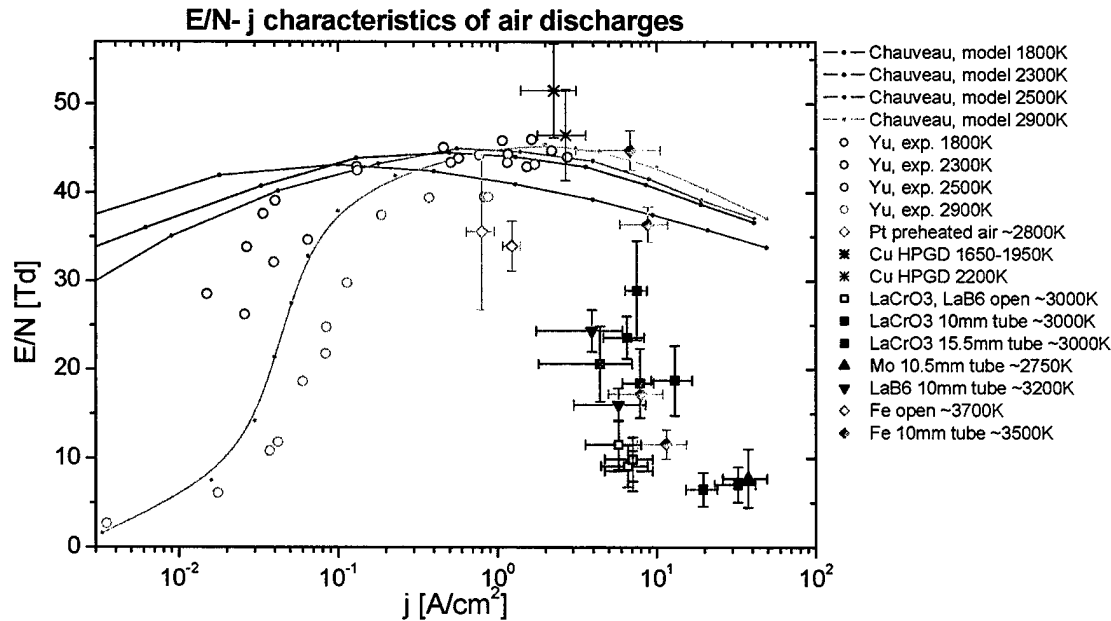
Figure 59. E/N-j characteristics of air discharges. Solid lines: collisional-radiative modeling by Chauveau [16]; experimental data designated Yu: discharges in preheated air with Pt cathodes [9-10]. Open symbols: experiments in open abmient air; full symbols: experiments in tubes with swirl flow of ambient air.

68

2.10.9. General *E-j* and *E/N-j* characteristics of nitrogen discharges

In the MURI final report and elsewhere [1, 9-10], we reported general electric field –current density (*E-j*) characteristics of DC atmospheric discharges in nitrogen. As with air, experimental points on *E-j* graph were shown together with numerical predictions of collisional-radiative model of nonequilibrium nitrogen plasmas, also developed in our research group. [5, 10] Although most of new experiments were performed in air, we have a few experimental points in nitrogen that are shown together with previously reported *E-j* nitrogen characteristics in Figure . Again, we also present the *E/N-j* graph in Figure 61 since this is a better representation taking account for temperature variations.

Figure 60 and Figure 61 also contain new numerical predictions obtained recently by Chauveau [34] in pure nitrogen nonequilibrium plasma. This new model shows a continuity in the *E-j* characteristic which is in agreement the experimental data. The discontinuity in Pierrot's earlier calculations [5] was caused by the jump in the n_e-T_e predictions. Chauveau's [34] new calculations tend to confirm that there is no discontinuity when n_e increases with T_e.
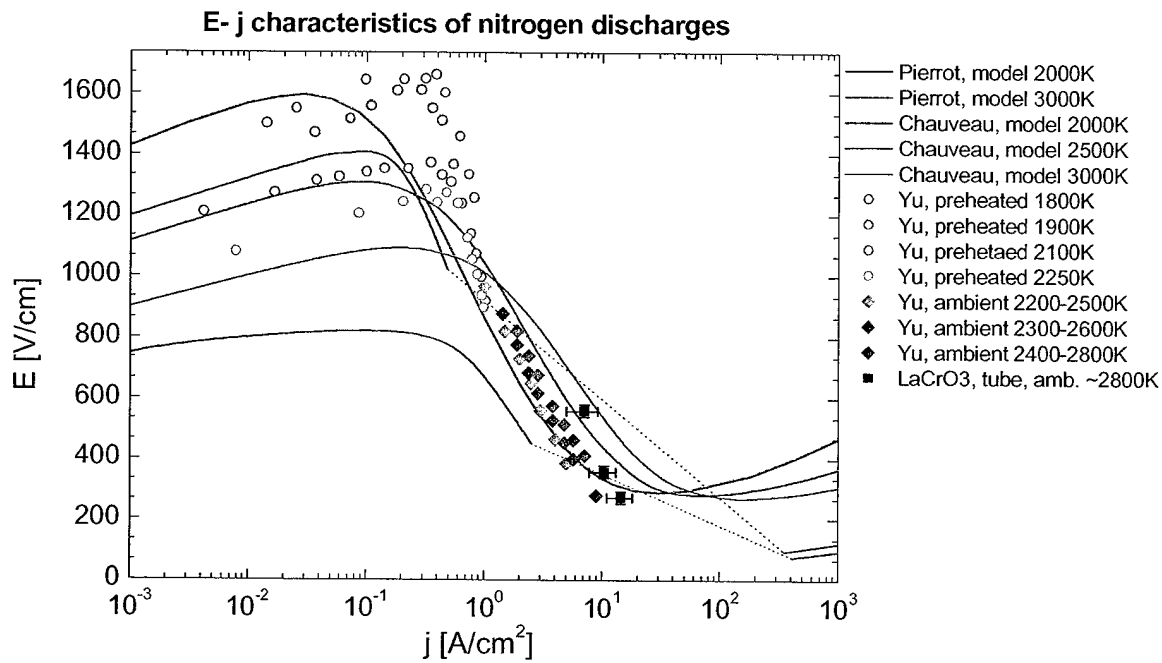
Figure 60. E-j characteristics of nitrogen discharges. Lines: calculations by collisional-radiative model of Pierrot [5] taken from Ref. [10], and new model predictions by Chauveau [34]; experimental data designated Yu: discharges in open preheated and ambient nitrogen with Pt cathodes [10]; blue symbols: discharges with LaCrO₃ thermionic cathode in 10.5 mm tube and swirl flow of ambient nitrogen.

E/N- j characteristics of nitrogen discharges

Legend:
- —— Pierrot, model 2000K
- —— Pierrot, model 3000K
- —— Chauveau, model 2000K
- —— Chauveau, model 2500K
- —— Chauveau, model 3000K
- ○ Yu, prehetaed 1800K
- ○ Yu, prehetaed 1900K
- ○ Yu, prehetaed 2100K
- ○ Yu, prehetaed 2250K
- ⟨ Yu, ambient 2200-2500K
- ◆ Yu, ambient 2300-2600K
- ◆ Yu, ambient 2400-2800K
- ■ LaCrO3, tube, amb. ~2800K
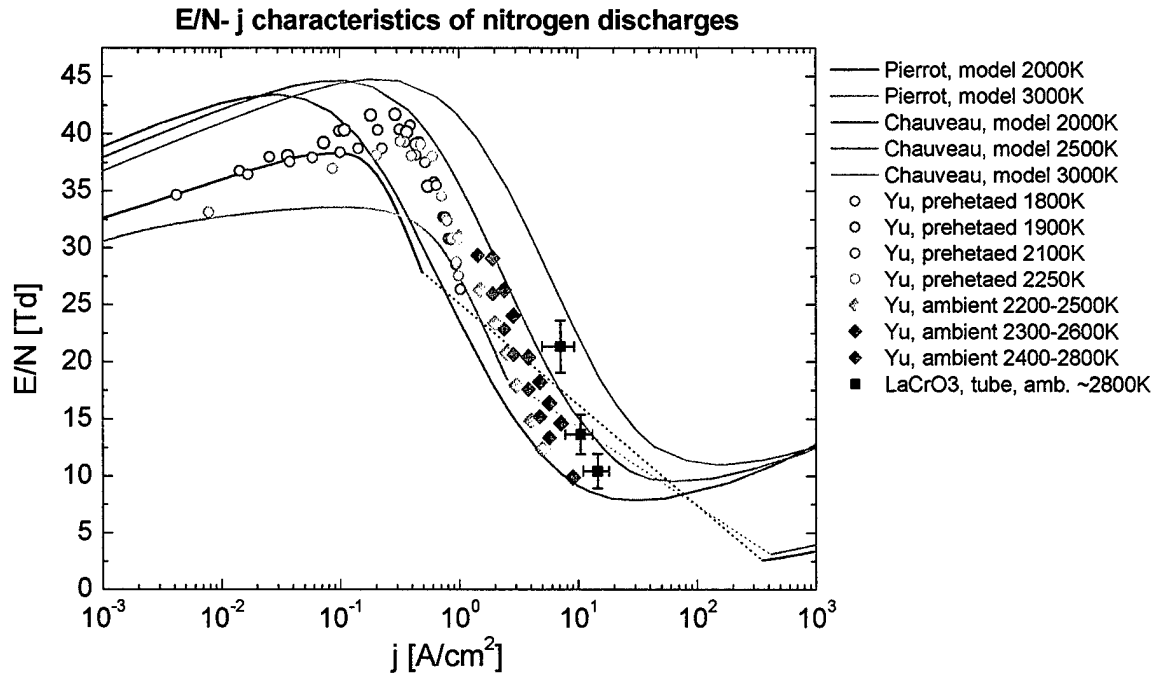
Figure 61. E/N-j characteristics of nitrogen discharges. Lines: calculations by collisional-radiative model of Pierrot [5] taken from Ref. [10], and new model predictions by Chauveau [34]; experimental data designated Yu: discharges in open preheated and ambient nitrogen with Pt cathodes [10]; blue symbols: discharges with LaCrO$_3$ thermionic cathode in 10.5 mm tube and swirl flow of ambient nitrogen.

The new nitrogen experimental data refer to discharges with thermionic LaCrO$_3$ cathode in swirl flow of ambient nitrogen in a 10.5 mm thick tube. Similar to air, discharges with thermionic cathode and swirl flow fall into the high j – low E region of the graph. However, they are very close to the experimental data of Yu obtained previously in ambient nitrogen. These old data have already indicated a falling trend of the E-j nitrogen curve. The new points are slightly shifted to the higher j because the discharge has confined in the tube due to the swirl flow.

2.11. Computational analysis of discharges in swirl flow

The swirl-stabilized discharge was modeled using a computational fluid dynamics method that simulates the key physical processes occurring in the flow. The method solves the Navier-Stokes equations augmented to include finite-rate reactions and internal energy relaxation, as well as energy addition due to the electric field. We use an 11-species (N_2, O_2, NO, O, N, O_2^+, N_2^+, NO^+, N^+, O^+, e) finite-rate air chemistry model, including a two-temperature (T, T_e) representation of the ionization reactions. [4] The governing equations and numerical method are discussed, and the computed results are then presented.

The solution of the full set of conservation equations (including mass conservation for each of the eleven species present, momentum equations in the axial, radial, and swirl directions, and internal energy equations for vibrational energy, electron translational energy, and total energy) is very challenging at the high electron temperature and atmospheric pressure conditions considered here. For an explicit calculation, the stable time step is dictated by the rate of ionization, Joule heating, and energy exchange. From experience, the stable time step is typically 0.1 ns, while the characteristic flow time is of the order of 200 μs; thus steady-state solutions require a huge number of time steps. Attempts to derive implicit formulations have been partially successful, resulting in time step increases of the order of 50 over explicit methods. However, the effect of using an implicit method on the time-accuracy of these flows is unknown, and therefore only an explicit time-integration method was used here.

To date, the full discharge code is only partially successful at predicting the state of the discharge. However, complete solutions of the swirling flow have been obtained to give estimates of E/N in the discharge region.

2.11.1. Governing equations

The electron conservation equation is given by:

$$\frac{\partial n_e}{\partial t} + \nabla \cdot \vec{j}_e = \omega_e$$

where ω_e is the rate of formation of electrons by reactions. The electron number flux, $\vec{j}_e$, is obtained from the electron momentum equation by neglecting inertia. This gives:

$$n_e \vec{v}_e = \vec{j}_e = -n_e \mu_e \vec{E} - \frac{D_e}{T_e} \nabla (n_e T_e)$$

where D_e is the electron diffusion coefficient and μ_e is the electron mobility. Now, for numerical reasons, [35] it is more convenient to write the electron velocity in terms of the logarithmic derivative of the electron number density:

$$\vec{v}_e = -\mu_e \vec{E} - \frac{D_e}{T_e} \nabla T_e - D_e \nabla (\ln n_e)$$

This form results in significantly less numerical error in regions where the electron number density is changing rapidly. In one dimension, the numerical representation of the electron conservation equation becomes:

$$n_{e,i}^{n+1} = n_{e,i}^n - \frac{\Delta t}{\Delta x} (n_{e,i+1/2}^n v_{e,i+1/2}^n - n_{e,i-1/2}^n v_{e,i-1/2}^n) + \Delta t \omega_{e,i}^n$$

where $n_{e,i+1/2}$ is the cell-face average electron number density, and $v_{e,i+1/2}$ is computed using the electron temperature and number density at grid points i and $i+1$. This approach is easily extended to multiple dimensions.

71

The electron energy equation is given by:

$$\frac{\partial}{\partial t}\left(\frac{3}{2}n_e k T_e\right)+\nabla\cdot\left(\frac{5}{2}n_e k T_e \vec{v}_e\right)=-n_e e\vec{E}\cdot\vec{v}_e-n_e\sum_h 3k[(T_e-T)+(T_e-T_v)\delta_{eh}]\frac{m_e}{m_h}v_{eh}-\omega_e I+\nabla\cdot(\lambda_e\nabla T_e)$$

where I is the average energy supplied by the electrons to the ionization reactions, and λ_e is the electron thermal conductivity. The energy exchange term represents the rate of energy loss from the electrons to the heavy particles through elastic collisions and through inelastic interactions primarily with the nitrogen vibrational modes. We account for the inelastic energy loss through the inelastic loss factor, δ_{eh}, which is from Ref. [4]. A similar numerical method is used for this equation, with the electron velocity evaluated using the logarithmic derivative.

It should be noted that in the direction perpendicular to the electric field, the electrons and ions diffuse as pairs. Thus, the electron diffusion coefficient in the field-normal direction is given by the ion diffusion coefficient. However, the electron thermal diffusivity is not changed by this ambipolar diffusion approximation.

The electric field can be computed from the Poisson equation for the electric potential. However, we choose to take advantage of the experimental geometry, and assume that the field only varies in the direction along the axis of the glass tube. In this case, there is no forced diffusion in the radial direction, which simplifies the implementation of the numerical method outlined above. In addition, we can determine the local electric field from the known total current of the discharge. Fundamentally, we know

$$I=-\int_A e n_e v_e\, dA=\int_A e n_e\left(\mu_e E_x+\frac{D_e}{T_e}\frac{\partial T_e}{\partial x}+D_e\frac{\partial \ln n_e}{\partial x}\right)dA$$

where A is the cross-sectional area of the discharge and v_e is the axial electron velocity. Now, since the total current is a parameter set by the experimental conditions, we can compute the electric field at each axial location from the above equation. This ensures that the discharge carries the correct current at every location. This concept is supported by previous work cited in Raizer. [24]

The above equations are coupled to the heavy particle mass conservation equations, the vibrational energy conservation equation, and the total energy conservation equation, and are solved using a finite-volume method. Because the flow field has a significant component of swirl, we solve a swirl momentum equation under the assumption that the flow is axisymmetric. We use an 11-species finite-rate air chemistry model, including a two-temperature (T, T_e) representation of the ionization reactions. [4] The coupling between the electrons and the heavy particle flow takes place primarily through the energy exchange terms.

2.11.2. Discharge conditions

In the computational analysis, we considered a representative DC discharge with $I = 500$ mA, operated in a 10 mm diameter tube with tangential injection of ambient air at $Q = 110$ slpm. The interelectrode distance was set to 6 cm.

The experimental configuration introduces the supply air by radial injection near the base of the cylindrical test section that is ended on top with the nozzle supplying the gas into the discharge tube. We simulate this injection through the use of mass, swirl momentum and energy source terms at the injection locations. The outflow pressure at the exit of the glass test tube is specified, and the flow field is then allowed to evolve until a steady-state flow is established. We then numerically ignite the discharge by providing a region of elevated temperature and electron concentration between the electrodes. The governing equations are then integrated in time until a steady discharge is established.

The cathode was represented in the middle of the discharge tube, 1 cm above the nozzle exit. The model does not account for the cathode material. The thermionic effect is thus not considered, but no cathode fall was implemented that is typical for the thermionic cathodes in our conditions, as discussed in section 2.10.2.

The cathode boundary conditions are critical to establishing the discharge. The cathode provides a flux of electrons corresponding to the known current. Therefore, for a given cathode dimension, the electron number or mass flux is known, and can be imposed at the grid points that represent the cathode. Within the finite volume cells that represent the cathode, we can compute the electron number density from the equation given above. Finally, we must assume an electron temperature within these cells; we take this value to be 2500 K. However, this assumption is not critical because the electron temperature increases rapidly due to Joule heating.

2.11.3. Computational results and discussion

Results of the computational analysis are represented in Figure 62-Figure 67 as color contours for every specific parameter. We show the converging nozzle and the 10 mm thick discharge tube on its top, some figures also show a zoomed section of the discharge close to the cathode.

Figure 62 and Figure 63 show the contours of the axial and swirl flow velocity. While the axial velocity is the highest in the discharge zone due to elevated temperature, the swirl velocity is the lowest there. The strongest swirl is found close to the tube walls, especially in the low part of the discharge zone.

Axial velocity (m/s)
70
60
50
40
30
20
10
0
-10
-20
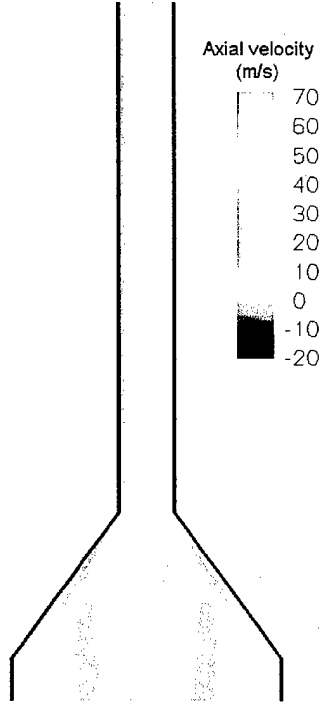
Figure 62. Contour of the axial velocity in the 10 mm thick tube with a DC discharge (I = 500 mA).

Swirl velocity (m/s)
50
40
30
20
10
0
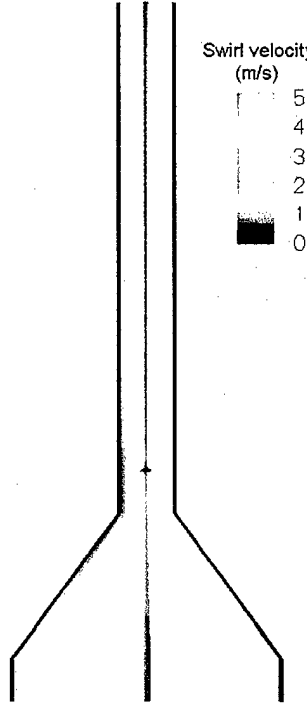
Figure 63. Contour of the swirl velocity in the 10 mm thick tube with a DC discharge (I = 500 mA).

p (kPa)
101000
100000
99000
98000
97000
96000
95000
94000
93000
92000
91000
90000
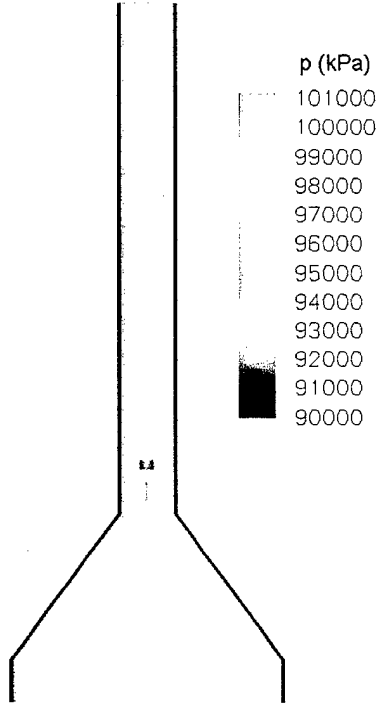
Figure 64. Contour of the pressure in the 10 mm thick tube with a DC discharge (I = 500 mA).

Figure 64 and Figure 65 show the contours of the pressure and the gas temperature. We observe a slight (max. 10 %) pressure drop in the discharge zone. The gas temperature is increased up to ~2500 K in the discharge zone. This is in a fairly good agreement with the measured gas temperatures that were typically about 3000 K. The region of the high temperature is approximately uniform, as can be seen from the zoomed section in Figure 65, and nicely confined in the middle of the tube.

Figure 66 represents the gas density contour. Because of slightly reduced pressure and strongly elevated temperature, the N drops 10 times in the discharge zone, compared to the normal conditions. The region of low N is fairly uniform and nicely confined in the middle of the tube. The lowered N causes a large enhancement on the reduced electric field E/N in the discharge zone. We assume that this is the key phenomenon that keeps the discharge confined in the middle of the tube and makes is extraordinarily stable even at long interelectrode distances.
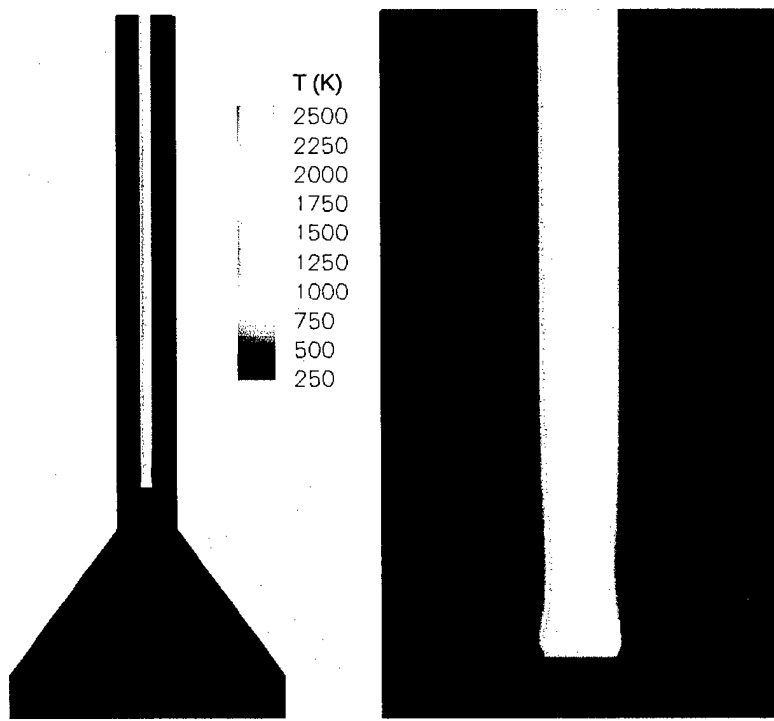
Figure 65. Contour of the gas temperature in the 10 mm thick tube with a DC discharge (I = 500 mA), zoomed section at right.
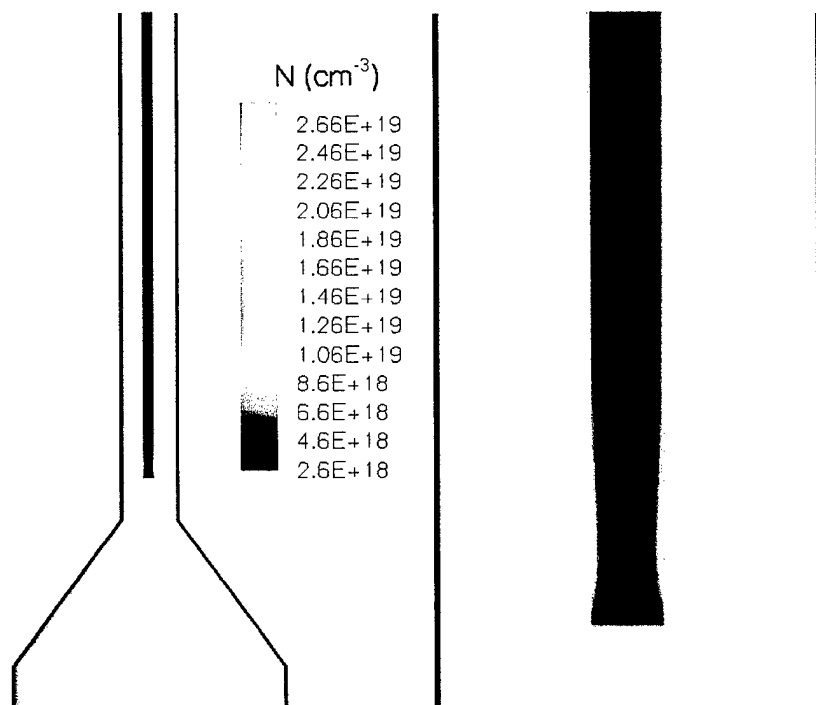
Figure 66. Contour of the gas density in the 10 mm thick tube with a DC discharge (I = 500 mA), zoomed section at right.
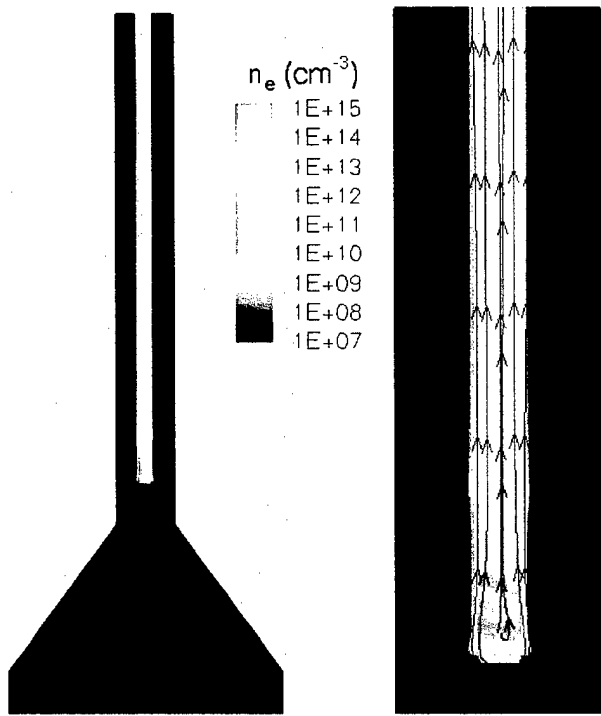
Figure 67. Contour of the electron density in the 10 mm thick tube with a DC discharge (I = 500 mA), zoomed section at right.

In Figure 67 we show the contour of the electron density. The $n_e \sim 10^{14}$ cm^{-3} is achieved in the discharge zone, which agrees well with the measured values for a 500 mA air discharge at these flow conditions. Even higher $n_e \sim 10^{15}$ cm^{-3} is found close to the cathode. Although we did not measure the n_e in this region, such a result is physically possible, because many electrons are emitted from the cathode (especially thermionic one), and the equilibrium between their generation and losses may have not yet been reached in this region. The computational results for the electron temperature are unfortunately not reliable at the present.

3. Conclusions

This final technical report summarizes the results of the program to investigate the volume scalability of nonequilibrium plasmas produced by electrical discharges in atmospheric pressure air or nitrogen, as well as to investigate related fundamental phenomena.

The review of the experiments with single DC discharges in ambient and preheated air and nitrogen provides basic characteristics of these nonequilibrium atmospheric pressure glow discharges. These discharges are able to produce nonequilibrium air and nitrogen plasmas with electron densities of the order of 10^{12} cm^{-3} and gas temperatures about 2000 K. We emphasize the mechanism of gas heating via vibrational-translational (V-T) energy transfer because it is found to considerably influence the discharge properties and plasma volume.

Investigation of the volume scalability of plasma produced by the electric discharges requires knowledge of the discharge diameter (radius). However, discharge diameter is often a vague concept and its measurement in atmospheric pressure plasmas is challenging, although it is often assumed to be coincident with the plasma emission. We employed two spatially resolved diagnostics techniques: cavity ring-down (CRDS) and optical emission spectroscopy (OES) in order to define and determine the diameter of a nitrogen discharge at atmospheric pressure. OES was used to measure spatial emission profiles of excited N_2 and N_2^+ states, as well as the gas temperature profiles. CRDS was used to measure the concentration profile of N_2^+ in its ground vibronic state. A collisional-radiative model was employed to infer the total concentration profiles of N_2^+ and N^+ from the measured N_2^+ X (v=0) concentration profile. The sum of N_2^+ and N^+ concentration profiles then gives the electron number density (n_e) profile. The n_e profiles are found to be well represented by the emission profiles of excited electronic states of N_2 and N_2^+. This result supports the use of emission spectroscopy as a tool for measuring the discharge diameter.

To understand the effects controlling the diameter of a discharge, we have developed a simple model of a DC discharge generated between two pin electrodes. The discharge size can be reasonably well predicted with this model. The modeling results are within a factor of two of the measurements. We then performed a detailed computational analysis of the DC discharge experiments in preheated air. A complete axisymmetric simulation including an 11-species finite-rate air kinetics model and a three-temperature energy formulation was used. The jet simulations using this CFD model produced an unstable jet with large-scale vortical structures. Contrary to the experiments, the non-uniformities pinch the discharge and transition to an arc occurs. We postulate that turbulent mixing in the experiments stabilizes the jet. Reformulated model prevents formation of large vortical structures, and we obtain stable diffuse discharges. The size of the computed electrically conducting channel matches the experiments, however the electron number densities are underpredicted. The electron temperature is similar to the experiment, and the vibrational and translational temperatures also agree well. We varied the

·

77

flow parameters and found that laminar diffusive processes were too weak to produce much change in the discharge radius.

Experimental investigations of flow/plasma interactions in a DC discharge placed in a transverse preheated air flow confirmed the essential role of the gas heating mechanism on the discharge shape and properties. The volume of plasma produced by the discharge is found counterintuitively to decrease when the air flow increases. We found that the vertical discharge extent is coincident with reduced field strength E/N profile since the rate coefficients of electron-impact processes are controlled by the E/N. When the flow velocity increases, the gas traversing the discharge region has less time to undergo the V-T energy transfer and therefore it does not heat up as much. Lower temperature results in higher gas density N, thereby decreasing the E/N further downstream the flow. As a result, the discharge extent is shorter at higher flow velocity.

Single DC discharges can produce plasma volumes of up to 0.5 cm^3. This volume can be almost doubled with a dual-discharge facility and increased further with multiple electrodes. For a given gas flow velocity, there is a minimum inter-discharge distance below which the discharges merge into a single column of nearly twice the diameter of the single discharge. Formation of a single column is due to the enhanced gas heating in the space between the two columns resulting in the enhanced reduced field E/N. The region between the discharges then undergoes more intense ionization processes. Thus, a preferential channel develops in the space between the two discharges, leading to the X-shape aspect. We also examined dual parallel and transverse DC discharges in fast flows of preheated air. The shape of dual discharges in preheated air depends on the flow velocity, which controls the rate of gas heating. The dual discharges in fast flows ($v{\sim}160$ m/s) do not merge into one column because there is little air heating in the space between them.

Repetitively pulsed discharges were scaled up by using a multiple-pin configuration. A plasma volume of about 0.5 cm^3 was formed with very low power requirements by using six elementary discharges in parallel. Larger volumes can be achieved by increasing the number of elementary discharges. Dual and multiple DC or pulsed discharges indicate a promising way for scaled-up plasmas.

Finally, we introduced a novel approach to produce highly ionized atmospheric pressure air and nitrogen plasmas by DC glow discharges. In this approach, we used thermionic cathodes and the swirl gas flow injection. We investigated various thermionic cathodes materials (LaCrO$_3$, LaB$_6$ and Mo). We also tested the effects of swirl flow in the discharges placed in tubes, compared with axial flow, and the tube diameter effects. As a result of both thermionic emission and swirl flow effects, an increase of the electron density by 1-2 orders of magnitude was achieved (10^{13}-10^{14} cm^{-3}), together with the high current densities j and the low electric fields E and reduced fields E/N. Use of small diameter tubes with swirl flow results in discharge confinement, and consequently electron density increase, regardless to the cathode material. At these conditions, the discharges are stable even at high flow rates of ambient air or nitrogen. They can be extended between the electrodes to as long as 10 cm, which is interesting from the point of view of plasma volume scaling. In addition, use of the thermionic cathodes results in the

lower E and E/N for a given j. Consequently, the power budget of these highly ionized plasmas related to the electron density is lower than in their previously investigated counterparts with ordinary cathodes.

A new falling region in the previously reported air discharge E-j and E/N-j characteristics was revealed after adding the experimental points referring to the DC discharges with thermionic cathodes and swirl flow in tubes. In nitrogen, the falling part of the E-j and E/N-j characteristics was already known. The new experiments with thermionic cathodes and swirl flow are in a good agreement with previously measured ones in ambient nitrogen, the discharge confinement due to the swirl flow causes their shift to the higher j and n_e.

In the last part of the report, we present a computational analysis of DC discharges in a tube with the swirl flow. Computational fluid dynamics method including finite-rate reactions of 11-species air chemistry model, including a two-temperature (T, T_e) representation of the ionization reactions, and internal energy relaxation, as well as energy addition due to the electric field was employed. The computational results are in a good agreement with experiments. The gas density spatial distribution related to the E/N distribution helps to understand the discharge confinement and its stability in the tube with swirling gas. Numerically predicted high values of the n_e also agree well with experimental estimates.

These new results indicate that the use of thermionic cathodes combined with the swirl flow stabilization represents a very promising way for producing nonequilibrium superionized plasmas in air or nitrogen at atmospheric pressure, as well as for scaling up the plasma volumes.

4. Personnel

Stanford Mechanical Engineering Department

- Professor Charles H. Kruger, Vice-Provost, Dean of Research and Graduate Policy.

- Dr. Christophe O. Laux, Senior Research Scientist (Ph.D. Mechanical Engineering, Stanford University, 1993)

- Dr. Zdenko Machala, Postdoctoral Fellow (Ph.D. Gas and Plasma Physics, University Paris XI, France, Comenius University, Slovakia, 2000)

- Dr. Xavier Duten, Postdoctoral Fellow (Ph.D. Gas and Plasma Physics, University of Paris XI, France, 2000)

- Dr. Azer Yalin, Postdoctoral Fellow (Ph.D. Mechanical Engineering, Princeton University, 2000)

- Dr. Denis Packan, Graduate Research Assistant (Ph.D. Mechanical Engineering, Stanford University, September 2002)

- Dr. Lan Yu, Postdoctoral Fellow (Ph.D. Mechanical Engineering, Stanford University, August 2001)

- Dr. Sophie Chauveau, Postdoctoral Fellow (Ph.D. Mechanical Engineering, Ecole Centrale Paris, 2001)

- Dr. J. Daniel Kelley, Visiting Scholar

University of Minnesota

- Professor Graham V. Candler

- Dr. Camille George, Research Scientist. (Ph.D Mechanical Engineering, University of Minnesota, 1998)

- Dr. Manoj Nagulapally, Graduate Research Assistant (Ph.D. Aerospace Engineering and Mechanics, University of Minnesota, June 2001)

- Brian Mader, Graduate Research Assistant. (B.S. Aerospace Engineering, University of Minnesota, June 2001)

5. Publications

- Duten, X., Packan, D., Yu, L., Laux, C.O., and Kruger, C.H., "DC and Pulsed Glow Discharges in Atmospheric Pressure Air and Nitrogen," *IEEE Transactions on Plasma Science, Special Issue on "Images in Plasma Science"*, Vol. 30, No. 1, pp. 178-179, 2002.

- Yu, L., Packan, D.M., Laux, C.O., and Kruger, C.H., "Direct-Current Glow Discharges in Atmospheric Pressure Air Plasmas," *Journal of Applied Physics*, Vol. 91, No. 5, 2678-2686, 2002.

- Kruger, C.H., Laux, C.O., Yu, L., Packan, D.M., Pierrot, L., "Nonequilibrium Discharges in Air and Nitrogen Plasmas at Atmospheric Pressure," *Pure and Applied Chemistry*, Vol. 74, No. 3, pp. 337-347, 2002.

- Yalin, A.P., Laux, C.O., Kruger, C.H., and Zare, R.N., Spatial Profiles of N_2^+ Concentration in an Atmospheric Pressure Nitrogen Glow Discharge, *Plasma Sources Science and Technology*, Vol. 11, No. 3, pp. 248-253, 2002.

- Yalin, A.P., Zare, R.N, Laux, C.O., and Kruger, C.H., "Temporally Resolved Cavity Ring-Down Spectroscopy in a Pulsed Nitrogen Plasma", *Applied Physics Letters*, Vol. 81, No. 8, pp. 1408-1410, 2002.

- Laux, C.O., Spence, T.G., Kruger, C.H., and Zare, R.N., "Optical Diagnostics of Atmospheric Pressure Air Plasmas," *Plasma Sources Science and Technology*, Vol. 12, pp. 125-138, 2003

To be published:

- Machala, Z., Yalin, A.P., Laux, C.O., Kruger C.H., "Determinations of the Diameter of an Atmospheric Pressure Nitrogen Glow Discharge by Emission and Cavity Ring-Down Spectroscopy," submitted to *J. Appl. Phys.*, 2003

- Machala, Z., Laux, C.O., Marode, E., Kruger C.H., "Atmospheric pressure DC glow discharges in air and nitrogen", prepared for *J. Phys. D: Appl. Phys.*, 2003-04

6. Interactions

6.1. Participations at Meetings, Conferences, Seminars

- Packan, D., Yu, L., Laux, C.O., Kruger, C.H., "Repetitively-Pulsed DC Glow Discharge in Atmospheric Pressure Air: Modeling and Experiments with a 12 kV, 10 ns, 100 kHz Pulse Generator," Proceedings of the 28th IEEE International Conference on Plasma Science, p. 259, Las Vegas, NV, June 17-22, 2001.

- Yu, L., Packan, D.M., Laux, C.O., Kruger, C.H., "Direct-Current Glow Discharges in Atmospheric Pressure Air and Nitrogen Plasmas," Proceedings of the 28th IEEE International Conference on Plasma Science, p. 350, Las Vegas, NV, June 17-22, 2001.

- Nagulapally, M., Candler, G.V., Laux, C.O., Kruger, C.H., "Numerical Modeling of Repetitively Pulsed Discharges in Flowing Atmospheric Pressure Plasmas," Proceedings of

the 28th IEEE International Conference on Plasma Science, p. 351, Las Vegas, NV, June 17-22, 2001.

- Yalin, A.P., Lommatzsch U., Zare, R.N., Laux, C.O., Kruger, C.H., "Cavity Ring-Down Spectroscopy of N_2^+ in Pulsed and DC Atmospheric Pressure Discharges," Proceedings of the 28th IEEE International Conference on Plasma Science, p. 9, Las Vegas, NV, June 17-22, 2001.

- Kruger, C.H., Laux, C.O., Packan, D.M., Yu, L., Yalin, A.P., Zare, R.N., Nagulapally, M., Candler, G.V., Kelley, J.D., "Nonequilibrium Discharges in Atmospheric Pressure Air," Proceedings of the 28th IEEE International Conference on Plasma Science, p. 348, Las Vegas, NV, June 17-22, 2001.

- Kruger, C.H., Laux, C.O., Yu, L., Packan, D.M., Pierrot, L., "Nonequilibrium Discharges in Air and Nitrogen Plasmas at Atmospheric Pressure," invited plenary lecture at the 15th International Symposium on Plasma Chemistry, Orléans, France, July 9-13, 2001.

- Kelley, J.D., Packan, D.M., Yu, L., Laux, C.O., and Kruger, C.H., "Repetitively pulsed glow discharge in atmospheric pressure air: modeling and experiments," Fourth Workshop on Magneto- and Plasma Aerodynamics for Aerospace Applications, Moscow, Russia, April 9-11, 2002.

- Laux, C.O., "Nonequilibrium Air Plasmas for Scramjet Ignition, Bio-Decontamination, and other Engineering Applications," Thermosciences Seminar Series, Stanford University, April 17, 2002.

- Laux, C.O., "Nonequilibrium Air Plasmas for Scramjet Ignition, Aerodynamic Flow Control, Bio-Decontamination, and other Engineering Applications," Joint Electrical Engineering/Mechanical Engineering Seminar, Old Dominion University, April 26, 2002.

- Chauveau, S.M., Laux, C.O., Kelley, J.D., and Kruger, C.H., "Vibrationally Specific Collisional-Radiative Model for Nonequilibrium Air Plasmas," AIAA 2002-2229, 33rd AIAA Plasmadynamics and Lasers Conference, Maui, HI, May 20-23, 2002.

- Yalin, A.P., Laux, C.O., Kruger, C.H., and Zare, R.N, "Spatially and Temporally Resolved Concentration Measurements of the N_2^+ Ion in Nitrogen Discharges by Cavity Ring-Down Spectroscopy," AIAA 2002-2245, 33rd AIAA Plasmadynamics and Lasers Conference, Maui, HI, May 20-23, 2002.

- George, C., Candler, G.V., Laux, C.O., and Kruger, C.H., "Computational Analysis of Diffuse Discharges in Atmospheric Pressure Air," AIAA 2002-2223, 33rd AIAA Plasmadynamics and Lasers Conference, Maui, HI, May 20-23, 2002.

- Machala, Z., Laux, C.O., and Kruger, C.H., "Nonequilibrium Microwave and DC-Discharge Plasmas in Atmospheric Pressure Air," Gordon Research Conference on Plasma Processing Science, Tilton, NH, July 21-26, 2002.

- Yalin, A.P., Machala, Z., Laux, C.O., Kruger, C.H., and Zare, R.N., "Optical Emission and Cavity Ring-Down Spectroscopy Measurements in Atmospheric Pressure Nitrogen Glow Discharge," Gordon Research Conference on Plasma Processing Science, Tilton, NH, July 21-26, 2002.

- Machala, Z., Laux, C.O., Duten, X., Packan, D.M., Yu, L., Kruger, C.H., "Scaled-up Nonequilibrium Air Plasmas", 41st Aerospace Sciences Meeting and Exhibit, January 2003, Reno, NV, paper AIAA 2003-874

- Chauveau, S. M., Kelley, J. D., Laux, C. O., and Kruger C. H., "Vibrationally Specific Modeling of Nonequilibrium Effects in air Plasmas", 41st Aerospace Sciences Meeting and Exhibit, January 2003, Reno, NV, paper AIAA 2003-137

- Kruger, C.H., "NON-EQUILIBRIUM DISCHARGES IN AIR PLASMAS AT ATMOSPHERIC PRESSURE," Fall Colloquium Series, Department of Physics, Old Dominion University, April 15, 2003.

- Machala, Z., Kruger, C.H., "Nonthermal Air Plasmas Produced by DC Discharges at Atmospheric Pressure", Thermosciences Division Seminar Series, Stanford University, Stanford, CA, USA, October 8, 2003

- Machala, Z., Laux, C.O., and Kruger, C.H., "Novel Ways to Increase Electron Density in Atmospheric Air and Nitrogen DC Glow Discharges", 56th Annual Gaseous Electronics Conference, October 2003, San Francisco, CA

- Machala, Z., Laux, C.O., Kruger, C.H., "Atmospheric Air and Nitrogen DC Glow Discharges with Thermionic Cathodes and Swirl Flow," 42nd Aerospace Sciences Meeting and Exhibit, January 2004, Reno, NV, paper AIAA 2004-355

- Machala, Z., Marode, E., Laux, C.O., Kruger, C.H., "DC Glow Discharges Atmospheric Pressure Air: Fundamentals and Innovations," International Workshop on Cold Atmospheric Pressure Plasmas: Sources and Applications, January 2004, Ghent, Belgium

6.2. Consultative and Advisory Functions to Other Laboratories and Agencies

- Dr. Laux serves on the Plasmadynamics and Lasers Committee of the American Institute of Aeronautics and Astronautics.
- Prof. Candler currently serves on the DoE/Sandia ASCI Advisory Panel. He is a member of the NATO Research Technology Organization, Working Group 10, Technologies for Hypersonic Flight. He also serves on the Thermophysics committee of the American Institute of Aeronautics and Astronautics.

7. New Discoveries, Inventions, or Patent Disclosures

None

8. Honors/Awards

- 2001 Invited Plenary Lecture: Laux, C.O., Kruger, C.H., Zare R.N., "Diagnostics of Atmospheric Pressure Air Plasmas," Arbeitsgemeinschaft Plasma Physik (APP) Spring Meeting, Bad Honnef, Germany, February 2001

- 2001 Invited Plenary Lecture: Kruger, C.H., Laux, C.O., Yu, L., Packan, D.M., Pierrot, L., "Nonequilibrium Discharges in Air and Nitrogen Plasmas at Atmospheric Pressure," 15th International Symposium on Plasma Chemistry, Orléans, France, July 9-13, 2001

- 2001 Best Student Paper Award, AIAA Thermophysics Committee, Candler G.V. et al.

- 2001 Invited Lecture: Laux, C.O., "DC and Pulsed Discharges in Atmospheric Pressure Air and Nitrogen Plasmas," 43rd Annual Meeting of the Division of Plasma Physics, Long Beach, CA, Oct. 29- Nov. 2, 2001. Bulletin of the American Physical Society, Vol. 46, No. 8, pp. 99-100, October 2001

- 2002 Invited Special Course: Laux, C.O., "Radiation and Nonequilibrium Collisional-Radiative Models," von Karman Institute Special Course on Physico-Chemical Modeling of High Enthalpy and Plasma Flows, Rhode-Saint-Genèse, Belgium, June 4-7, 2002

- Cuthbertson Award, Kruger, C.H., Stanford University, June 2003

- 2003 Plasma Chemistry Award, Kruger, C.H., International Plasma Chemistry Society, June 2003

9. References

[1]   Mechanisms of Ionizational Nonequilibrium in Air Plasmas, Final Technical MURI Report, submitted to AFOSR by C.H. Kruger, October 2002

[2]   R.J. Gessmann, C.O. Laux, C.H. Kruger, "Kinetic Mechanisms of Recombining Atmospheric Pressure Air Plasmas", AIAA 97-2364, 28th Plasmadynamics and Lasers Conference, Atlanta, GA, June 1997 (awarded 1998 Plasmadynamics and Lasers Best Technical Paper Award).

[3]   C. O. Laux, R. J. Gessman, D. M. Packan, L. Yu, C. H. Kruger, and R. N. Zare, "Experimental Investigations of Ionizational Nonequilibrium in Atmospheric Pressure Air Plasmas," 25th IEEE International Conference on Plasma Science (ICOPS), Raleigh, NC, 1998.

[4]   C. O. Laux, L. Yu, D. M. Packan, R. J. Gessman, L. Pierrot, C. H. Kruger, and R. N. Zare, "Ionization Mechanisms in Two-Temperature Air Plasmas," *AIAA 99-3476*, 30th AIAA Plasmadynamics and Lasers Conference, Norfolk, VA, 1999.

[5]   L. Pierrot, L. Yu, R. J. Gessman, C. O. Laux, and C. H. Kruger, "Collisional-radiative modeling of nonequilibrium effects in nitrogen plasmas," *AIAA 99-3478*, 30th AIAA Plasmadynamics and Lasers Conference, Norfolk, VA, 1999.

[6]   M. Nagulapally, G. V. Candler, C. O. Laux, L. Yu, D. Packan, C. H. Kruger, R. Stark, and K. H. Schoenbach, "Experiments and Simulations of DC and Pulsed Discharges in Air Plasmas," *AIAA 2000-2417*, 31st AIAA Plasmadynamics and Lasers Conference, Denver, CO, 2000.

[7]   L. Yu, L. Pierrot, C. O. Laux, and C. H. Kruger, "Effects of Vibrational Nonequilibrium on the Chemistry of Two-Temperature Nitrogen Plasmas," *Plasma Chemistry and Plasma Processing*, vol. 21, pp. 483-503, 2001.

[8]   D. Packan, L. Yu, C. O. Laux, and C. H. Kruger, "Repetitively Pulsed DC Glow Discharge in Atmospheric Pressure Air: Modeling and Experiments with a 12-kV, 10- ns, 100-kHz Pulse Generator," 28th IEEE International Conference on Plasma Science, Las Vegas, NV, 2001.

[9]   L. Yu, C. O. Laux, D. M. Packan, and C. H. Kruger, "Direct-Current Glow Discharges in Atmospheric Pressure Air Plasmas," *J. Appl. Phys.*, vol. 91, pp. 2678-2686, 2002.

[10] L. Yu, "Nonequilibrium effects in two-temperature atmospheric pressure air and nitrogen plasmas," Ph.D. Thesis, *Mechanical Engineering*, Stanford Univeristy, Stanford, CA, 2002

[11] C. H. Kruger, C. O. Laux, L. Yu, D. M. Packan, and L. Pierrot, "Nonequilibrium Discharges in Air and Nitrogen Plasmas at Atmospheric Pressure," *Pure and Applied Chemistry*, vol. 74, pp. 337-347, 2002.

[12] X. Duten, D. Packan, L. Yu, C. O. Laux, and C. H. Kruger, "DC and Pulsed Glow Discharges in Atmospheric Pressure Air and Nitrogen," *IEEE Transactions on Plasma Science Special Issue on "Images in Plasma Science"*, vol. 30, pp. 178-179, 2002.

[13] D.M. Packan, "Repetitively Pulsed Glow Discharge in Atmospheric Pressure Air" Ph.D. Thesis, *Mechanical Engineering*, Stanford Univeristy, Stanford, CA, 2002

[14] A. P. Yalin, R. N. Zare, C. O. Laux, and C. H. Kruger, "Temporally Resolved Cavity Ring-Down Spectroscopy in a Pulsed Nitrogen Plasma," *Appl. Phys. Lett.*, vol. 81, pp. 1408-1410, 2002.

[15] A. P. Yalin, C. O. Laux, C. H. Kruger, and R. N. Zare, "Spatial Profiles of N_2^+ Concentration in an Atmospheric Pressure Nitrogen Glow Discharge," *Plasma Sources Science and Technology*, vol. 11, pp. 248-253, 2002.

[16] S. M. Chauveau, C. O. Laux, J. D. Kelley, and C. H. Kruger, "Vibrationally Specific Collisional-Radiative Model for Nonequilibrium Air Plasmas," *AIAA 2002-2229*, 33rd AIAA Plasmadynamics and Lasers Conference, Maui, HW, 2002.

[17] S. M. Chauveau, J. D. Kelley, C. O. Laux, and C. H. Kruger, "Vibrationally Specific Modeling of Nonequilibrium Effects in air Plasmas", 41st Aerospace Sciences Meeting and Exhibit, January 2003, Reno, NV, paper AIAA 2003-137

[18] Z. Machala, C.O. Laux, X. Duten, D.M. Packan, L. Yu, C.H. Kruger, "Scaled-up Nonequilibrium Air Plasmas", 41st Aerospace Sciences Meeting and Exhibit, January 2003, Reno, NV, paper AIAA 2003-874

[19] Z. Machala, C.O. Laux, C.H. Kruger, "Atmospheric Air and Nitrogen DC Glow Discharges with Thermionic Cathodes and Swirl Flow," 42nd Aerospace Sciences Meeting and Exhibit, January 2004, Reno, NV, paper AIAA 2004-355

[20] C.O. Laux, T.G. Spence, C.H. Kruger, and R.N. Zare, "Optical Diagnostics of Atmospheric Pressure Air Plasmas," *Plasma Sources Science and Technology*, Vol. 12, pp. 125-138, 2003

[21] C. O. Laux, R. J. Gessman, C. H. Kruger, F. Roux, F. Michaud, and S. P. Davis, "Rotational Temperature Measurements in Air and Nitrogen Plasmas Using the First Negative System of N_2^+," *JQSRT*, vol. 68, pp. 473-482, 2001.

[22] C. O. Laux, "Optical Diagnostics and Radiative Emission of Air Plasmas," Ph.D. Thesis, *Mechanical Engineering*. Stanford, CA, USA: Stanford University, 1993.

[23] C. O. Laux, "Radiation and Nonequilibrium Collisional-Radiative Models," Von Karman Institute Lecture Series on Physico-Chemical Models of High Enthalpy and Plasma Flows Modeling, Rhode Saint-Genese, Belgium, June 4-7, 2002

[24] Yu. P. Raizer, "Gas Discharge Physics," New York: Springer, 1991

[25] Busch, K.W. and Busch, A.M. (1999) Cavity-Ringdown Spectroscopy – ACS Symposium Series 720 (Washington, DC: American Chemical Society)

[26] Berden G., Peeters, R., Meijer, G. (2000) Cavity Ring-Down Spectroscopy: Experimental Schemes and Applications, *Int. Reviews in Physical Chemistry* 19 (4): 565-607

[27] F. G. Blottner, M. Johnson, and M. Ellis, "Chemically Reacting Viscous Flow Program for Multi-Component Gas Mixtures," Sandia Laboratories, Albuquerque, NM SC-RR-70-754, Dec. 1971 1971.

[28] R. N. Gupta, J. M. Yos, R. A. Thompson, and K.-P. Lee, "A Review of Reaction Rates and Thermodynamic and Transport Properties for an 11-Species Air Model for Chemical and Thermal Nonequilibrium Calculations to 30,000 K," NASA RP-1232, August 1990 1990.

[29] J.-H. Lee, "Electron-Impact Vibrational Relaxation in High-Temperature Nitrogen," *AIAA 92-0807*, 30th Aerospace Sciences Meeting and Exhibit, Reno, NV, 1992.

[30] R. D. Ramshaw, "Self-Consistent Effective Binary Diffusion in Multicomponent Gas Mixtures," *J. Non-Equil. Thermodyn.*, vol. 15, pp. 295-300, 1990.

[31] M. Nagulapally, D. Kolman, G. V. Candler, C. O. Laux, R. J. Gessman, and C. H. Kruger, "Numerical Simulation of Nonequilibrium Nitrogen and Air Plasma Experiments," 29th AIAA Plasmadynamics and Lasers Conference, 1998.

[32] P.-C. Huang, "A Turbulent Swirling Arc Model and a Two-Fluid Turbulence Model for Thermal Plasma Sprays," University of Minnesota, 1993

[33] L.N. Dobretsov, M.V. Gomoiunova "Emission Electronics," Jerusalem, Israel program for scientific translations, 1971

[34] S. M. Chauveau, private communication

[35] E.P. Hammond, K. Mahesh, and P. Moin, *"A Numerical Method to Simulate Radio-Frequency Plasma Discharges,"* J. Computational Physics **176**, 402, 2002